Theory of Finite-temperature and Non-equilibrium X-ray Absorption

Tun Sheng Tan

A dissertation
submitted in partial fulfillment of the
requirements for the degree of

Doctor of Philosophy

University of Washington

2020

Reading Committee:

John Rehr, Chair

Gerald Seidler

Shih-Chieh Hsu

Joshua Kas

Program Authorized to Offer Degree:
Physics

University of Washington

Abstract

Theory of Finite-temperature and Non-equilibrium X-ray Absorption

Tun Sheng Tan

Chair of the Supervisory Committee:
John Rehr
Physics

There has been considerable interest in non-equilibrium phenomena in recent years. For example, the development of femtosecond lasers has led to many experiments involving non-equilibrium systems. In these experiments, the electrons and lattice are in an out-of-equilibrium state due to the significantly longer electron-lattice relaxation time than the energy absorption of the electrons. Understanding the interaction between the electrons and atomic structures in these short live non-equilibrium state of matter can provide new insight for next-generation spintronic devices and high energy density physics. Time-resolved x-ray absorption spectroscopy (TR-XAS) has an advantage over diffraction spectroscopy by probing the local atomic structure and local electronic properties. Analyzing the spectra requires accurate modeling of the excitations across a wide range of conditions but such analysis codes are not widely available. Our goal is to develop a first-principle theoretical framework which quantitatively agrees with absorption near-edge structure (XANES) This thesis aims to develop a finite-temperature electronic structure theory that accounts for the temperature dependence of the exchange-correlation and the phonon interactions. We first describe the theory of x-ray absorption at finite temperature with the inclusion of temperature dependent exchange-correlation using the multiple-scattering formalism. Dynamic effects from the lattice can be included in the theory using molecular dynamics or the computation of dynamical matrix. This method has been implemented in the real-space

multiple scattering code, FEFF10. Finally, we present the finite temperature generalization of the COHSEX approximation to the quasiparticle electron self-energy. This contribution highlights the importance of the dynamic corrections to the COH approximation especially for high energy unoccupied states. These developments make possible simulations of a wide variety of systems and experiments with temperatures up to the warm dense matter regime.

TABLE OF CONTENTS

Page

List of Figures iv

Glossary ix

Chapter 1: Introduction 1
1.1 Background 2
1.1.1 X-ray Absorption 2
1.1.2 Warm Dense Matter 4
1.1.3 Magnetism of Transition Metals 6
1.2 Goals and Contributions 8
1.3 Organization of this Dissertation 9

Chapter 2: Theory of Finite-Temperature X-ray Absorption 10
2.1 Quasiparticle XAS 12
2.2 Green's Function Approach 13
2.2.1 Constructing Green's Function 15
2.3 Finite-Temperature Self-consistent Field Potential 15
2.3.1 Contour Integration 16
2.4 Core Hole Lifetime and Instrumental Broadening 17
2.5 Finite-temperature X-ray Spectroscopy Code FEFF 18
2.6 Summary 20

Chapter 3: Modeling of Non-equilibrium Dynamics 21
3.1 Effects of Thermal Disorder 22
3.1.1 Ab Initio Molecular Dynamics 23
3.1.2 Monte Carlo Vibrational Mode Sampling 25
3.2 Dynamic Response Approximations 26

3.2.1 2-Temperature Model of Dynamic Response 26
3.2.2 3-Temperature Model of Spin Dependent Systems 28
3.3 Summary 29

Chapter 4: Calculations of Finite Temperature X-ray Spectra 30
4.1 Warm Dense Aluminum 30
4.2 Warm Dense Copper 33
4.3 Non-equilibrium Fe/MgO Heterostructure 37
4.3.1 Fe L_3-edge 40
4.3.2 O K-edge 44
4.4 Summary 48

Chapter 5: Finite-temperature Self-energy Correction 50
5.1 COHSEX Approximation 52
5.1.1 Zero-temperature 52
5.1.2 Finite-temperature 54
5.2 Static vs Dynamic COHSEX 55
5.3 Analysis 59
5.4 Summary 62

Chapter 6: Summary and Conclusions 64
6.1 Theory of Finite-Temperature XAS 65
6.2 Finite-Temperature COHSEX Self-Energy 65
6.3 Future Work 66
6.4 Concluding Remarks 68

Appendix A: Numerical Solution of Convolution Integral 69

Appendix B: Harmonic Approximation of X-ray Absorption 70
B.1 Derivation of Dynamical Matrix 70
B.2 Debye-Waller Factor 72

Appendix C: FEFF10 Finite-temperature Codes 74
C.1 Finite-temperature Related Cards 74
C.2 Description of Subroutines 75

C.3 Example Calculations 75

Appendix D: Derivation of Static COHSEX Approximation 80

Appendix E: Fe/MgO Heterostructure 82
E.1 Normalization of O K-edge 82
E.2 Density of State Calculation 82

Bibliography 85

LIST OF FIGURES

Figure Number Page

1.1 Experimental cobalt (Co) K-edge absorption spectrum versus incident photon energy at room temperature.[19] 3

1.2 Temperature-density phase diagram for two-component plasma adapted from Ref [28]. The separation between the different statistics regime is define by the electron (ion) degeneracy parameter χ_e (χ_i) where $\chi_a = n_a\lambda_D^3$ and the de Broglie wave length $\lambda_D = h/\sqrt{2\pi m_a k_B T_a}$. 5

1.3 A schematic spin vector configuration illustrating the differences between Stoner model and Heisenberg model. The thermal response of Stoner model reduces the overall spin amplitude whereas in the Heisenberg model, a spin disorder is induced. 7

2.1 The exchange ϵ_x and correlation ϵ_c contributions to the the exchange-correlation energy per particle ϵ_{xc} versus temperature for the homogeneous electron gas model adapted from Ref [18]. 12

2.2 Energy contour for electron density calculation at temperature T>0. Here, $\omega_j = \pi(2j-1)kT$ denotes the imaginary part of the Matsubara poles of $f_T(E,\mu)$. The integration starts from some energy level E_B above the core states but below the valence states. Contour A (blue) represents the original integration path along the real axis while contour C (red) represents the integration path in the imaginary plane. 18

2.3 Example of a density of state $\rho(\omega)$ along different height in the complex plane. The imaginary part of ω increases from blue to red. 19

3.1 Dynamics of electron temperature (blue) and lattice temperature (red) based on two-temperature model calculation. The absorption power is calculated using Beer-Lambert law for a Gaussian profile 400 nm laser source for a 70 nm thick copper. 28

4.1 Chemical potential for aluminum, $\mu(T)-\mu(T=0)$ versus electron temperature,T using von Barth Hedin exchange-correlation potential (blue) [55] and KSDT exchange-correlation potential (red) [32]. The T=0K DFT calculation (orange) by Lin et al. [87] is shown up to $T = 4$ eV. 31

4.2 Density of states for aluminum at electronic temperature $T_e = 10$ eV: (blue) our calculation including states up to $l_{max} = 8$, (black) the non-relativistic KKR calculation by Starrett [48] and (red) the average atom model, Tartarus [48, 35]. 32

4.3 Electron temperature dependence of K-edge absorption for Al at $T_e = 0.025$, 0.5, 1.4 and 3.0 eV. 33

4.4 K-edge absorption for equilibrium Al ($T_e = T_L$) at solid density. (Left) Experimental absorption spectra at $T = 0$ and 0.09 eV.[25] FEFF simulation are done at the same temperature as the experiment. From bottom to top, QMD-DFT are simulated at $T = 0$ and 0.07 eV while HNC-NPA are simulated at $T = 0$ and 0.1 eV. (Right) Experimental absorption spectra at $T = 0.27$, 1.4 and 1.76 eV. From bottom to top, QMD-DFT are simulated at $T = 0.43$, 0.86 and 0.07 eV while HNC-NPA are simulated at $T = 0.5$ and 1.0 eV. FEFF simulation are done at $T = 0.27$, 1.4 and 3.0 eV. 34

4.5 Copper L_3-edge at solid density for (Left) electron temperature $T_e = 300$ K up to 9000 K at lattice temperature $T_L = 300$ K and (Right) for lattice temperature $T_L = 300$ K up to 5000 K at electron temperature $T_e = 300$ K. The DFT calculation by Jourdain et al. [91] is shown for $T_e = 300$ K (light blue) and 5800 K (green). The lower panels show the change in absorption with respect to the ambient condition $T_e = T_L = 300$ K. 35

4.6 (Left) Edge shift in the L_3-edge as a function of electron temperature. The blue curve is a linear fit of the FEFF calculation (red). The error bar represents the standard deviation of the edge shift over different lattice temperature up to $T_L = 10000$ K. (Right) The change in pre-edge area as a function of electron temperature. The DFT calculation (green) by Jourdain et al. [91] is computed using ABINIT at lattice temperature $T_L = 300$ K. 36

4.7 Time-resolved XANES for 70 nm copper at different times t =2 ps and 9 ps. The experimental measurement (red) is averaged over 150 snapshots. The ambient condition measurement is averaged over 70 ps. Our calculation (blue) for different times are computed at $T_e = 10200$ K adn 6000 K. The DFT result by Cho et al. [5] (green) is calculated using Quantum Espresso code at the same temperatures. 38

4.8 $[Fe/MgO]_8$ heterostructure made up of eight 2 nm Fe and 2 nm MgO grown on a Si_3N_4 substrate with a Cu heat sink. 39

4.9 The cross section of the structure used in our calculation provided by Markus Gruner and Rossitza Pentcheva. Atoms in gold are Fe, in red are O and in orange are Mg. The inner layer is labeled L1. The intermediate layers are labeled L2 and L3. The interfaces are labeled L4. 39

4.10 Layer resolved density of states (DOS) for Fe/MgO at $T = 0$ K. From the left, the first two figures are the total DOS of iron for the center layer (L1) and the interface layer (L4). The last two figures are the total DOS of MgO for layers L4 and L1. 41

4.11 Layer resolved x-ray absorption of Fe/MgO heterostructure for: (left) Fe L_3-edge and (right) O K-edge. Layer 1 corresponds to the middle layer and layer 4 correspond to the interface layer. The average absorption spectra (black) are slightly offset. 42

4.12 Dynamics of 16 nm Fe layer induced by a laser pulse with fluence of 20 mJ/cm^2, width of 50 fs and wavelength of 263 nm. The electronic temperature with detector temporal resolution of 150 fs is shown in dashed. 43

4.13 Fe L3-edge x-ray absorption for paramagnetic state and ferromagnetic state of Fe/MgO. In the solid blue line is the calculated absorption for ambient condition (ferromagnetic state). In dashed lines are the calculated absorption ($T_e = 300$ K, 1600 K) for the paramagnetic excited system. In black and red are the unpumped and pumped experimental measurements at 240 fs time-delay. 44

4.14 (Top) Spin-polarized density of state for L4 layer of Fe. The shaded area represents the occupied portion of the density at $T = 300$ K. (Bottom) Density of state for L4 layer of Fe in the paramagnetic state. The density is scaled by 1/2 to match the spin-polarized density in the plot above. 45

4.15 (Top) Comparison between layer-averaged XANES and experimental measurement at 240 fs time-delay. (Bottom) Change in absorption between elevated temperature absorption and the room temperature absorption. In black is the experimental differences. In the solid lines are the calculated differences due to change in electronic temperature only. In dashed lines are the calculated differences ($T_e = 1500$, 2000 K) due to the change in electronic temperature and atomic spin based the magnetization curve in Ref [88]. 46

4.16 (Top) Comparison between layer-averaged XANES (with 0.1 offset) and experimental measurement at 87 fs time-delay. Substantial background is present in the pre-edge region but it does not affect the spectral difference. (Bottom) Change in absorption between elevated temperature absorption and the room temperature absorption. In black is the experimental differences. In the solid lines are the differences due to Debye-Waller factor only. 47

4.17 (Top) Comparison between layer-averaged XANES (with 0.1 offset) and experimental measurement at 90 ps time-delay. Substantial background is present in the pre-edge region but it does not affect the spectral difference. (Bottom) Change in absorption between elevated temperature absorption and the room temperature absorption. In black is the experimental differences. In the solid lines are the differences due to Debye-Waller factor only. 48

5.1 (Color online) Results for the SEX (left) and COH (right) contributions to the static (dashed) and full dynamic (solid) quasiparticle self-energy vs k/k_F at various temperatures T/T_F for the homogeneous electron gas for $r_s = 2.0$: (from blue to red) the curves denote T/T_F =0.01, 0.5, 1.0, and 2.0. Note that the COH contribution is always significantly larger in magnitude than the SEX and persists to higher k/k_F, while the SEX becomes for unoccupied states above k_F. 56

5.2 (Color online) The real part of static COHSEX approximation (dashed) vs fully dynamic self-energy (solid) for various densities: (from blue to orange) r_s =1.0, 2.0, 3.0, 4.0 at $T/T_F = 0.01$ (left) and 1.0 (right). Note that the high temperature behavior is considerably smoother than near $T = 0$ and the change in behavior beyond about $k = k_p$ reflecting the onset of plasmon excitations. For reference the LDA-$v_{xc}(T)$[113, 101] for each r_s are added as circles at k_F. 57

5.3 (Color online) Fully dynamic COH (solid) and SEX (dashed) contributions to the imaginary part of the quasiparticle correction to the DFT energy ε_k vs k/k_F for $r_s = 4.0$, for various temperatures: (from blue to red) T/T_F =0.01, 0.5, 1.0, and 2.0. Note that the dominant contribution comes from the COH terms, while the dynamic contributions to the SEX from particle-hole excitations are significant only near k_F. 58

5.4 (Color online) The electron energy-loss function $L(q, \omega) = |\text{Im } \epsilon^{-1}(q, \omega)|$ for $r_s = 2.0$ at various temperatures: (from blue to red) T/T_F =0.01, 0.5, 1.0, and 2.0 for momentum $q/k_F = 0.5$ (left) and 2.0 (right). 59

5.5 Real (solid) and imaginary (dashed) parts of the renormalization constant Z_k vs k/k_F for r_s=4.0 at (blue to red) T/T_F =0.01, 0.5, 1.0, and 2.0. 61

5.6 (Color online) Dynamic correction to COHSEX self-energy $\Sigma(k, E_k) - \Sigma_k^{COHSEX}$ at the Fermi level k_F as a function of r_s: from blue to red, the curves denote T/T_F =0.01, 0.5, 1.0, and 2.0. 62

6.1 Finite-temperature XANES workflow in FEFF10. The red boxes highlight the temperature dependent steps in the workflow. 66

B.1 Temperature dependence of $\sigma^2(T)$ for the nearest neighbor (left) and next nearest neighbor (right) single scattering path in iron. The $\sigma^2(T)$ computed using the dynamical matrix with GGA functional (blue) is compared to the correlated Debye model (green) and experiment measurements [131] (red). . 73

C.1 (Top) Electron temperature dependence of L_3-edge in titanium for T_e= 0.025, 0.5, 1.0 and 3.0 eV. (Bottom) The difference in absorption with respect to the T_e= 0.025 eV absorption spectrum. 76

C.2 (Top) Electron temperature dependence of L_3-edge in vanadium for T_e= 0.025, 0.5, 1.0 and 3.0 eV. (Bottom) The difference in absorption with respect to the T_e= 0.025 eV absorption spectrum. 77

C.3 (Top) Electron temperature dependence of L_3-edge in silver for T_e= 0.025, 0.5, 1.0 and 3.0 eV. (Bottom) The difference in absorption with respect to the T_e= 0.025 eV absorption spectrum. 78

C.4 (Top) Electron temperature dependence of L_3-edge in gold for T_e= 0.025, 0.5, 1.0 and 3.0 eV. (Bottom) The difference in absorption with respect to the T_e= 0.025 eV absorption spectrum. 79

E.1 (Left) Oxygen K-edge X-ray absorption before background subtraction at time-delay t = 870 fs and 90 ps. In black are the measurements before pumping and in red are the measurements after pumping. The differences in the signals are very small to observed. (Right) Background subtracted absorption measurement before pumping at time-delay t = 870 fs (black) and 90 ps (blue). 83

E.2 Layer resolved density of states (DOS) for Fe/MgO at T_e=0K. From the left, the first four figures are the iron total DOS of layers from L1 to L4 and the last four figures are the DOS for oxygen and magnesium of layers from L4 to L1. The FEFF DOS for MgO are shifted by -2.6eV and Fe are shifted by 0.2eV to match the Fermi level of the DFT. The reference density of states are the DFT calculation by Rothenbach et al. [8]. 84

GLOSSARY

XAS: X-ray absorption spectrum

EXAFS: Extended x-ray absorption fine structure

XANES: X-ray absorption near edge structure

DOS: Density of states

FMS: Full multiple scattering

FT: Finite temperature

WDM: Warm dense matter

TR: Time-resolved

NEQ: Non-equilibrium

SCF: Self-consistent field

3TM: Three-temperature model

2TM: Two-temperature model

DW: Debye-Waller

CD: Correlated Debye

FSR: Final state rule

COHSEX: Coulomb hole screened exchange

MD: Molecular dynamics

DF: Density functional theory

ACKNOWLEDGMENTS

I would like to thank all of the people who have been very supportive during my time at the University of Washington. I would like to express my sincere appreciation to Professor John J. Rehr for providing support and patience throughout the program. This work would not have been possible without his guidance. Next, I also would like to thank Josh Kas and Fernando Vila for their mentorship and support. I would like to express my appreciation to Gerald Seidler and Shih-Chieh Hsu for their feedback and advice. Finally, I would like to thank my family for their loving support.

Chapter 1

INTRODUCTION

X-ray absorption spectroscopy (XAS) is an important tool for the study of physical processes in many fields ranging from materials science to chemistry, geophysics and astrophysics.[1, 2, 3, 5, 6, 4] XAS has been extensively used to probe the local electronic properties and local atomic structure simultaneously at various synchrotron facilities around the world. With the development of x-ray free electron lasers (XFELs), XAS experiments have been extended to treat ultra-short temporal resolution of order 10^{-15} ~10^{-12} seconds. This time-resolved capability is important when investigating the dynamic response of a sample like spin relaxation [7, 6] and electron-phonon energy transfer [5, 8].

A typical x-ray absorption spectrum consists of a rapidly raising edge due to the creation of a photoelectron from a core electron and is followed by an oscillating decay in amplitude up to several hundreds of eV. The energy range of ~10eV from the edge is called the x-ray absorption near-edge structure (XANES). Interpreting the spectra is highly non-trivial due to the complex nature of XANES. Standard analysis of XANES involves comparison between experimental spectra and numerical simulations. In addition, the validity of the theory under extreme thermodynamic conditions and strongly non-equilibrium conditions still requires validation. A goal of this work is to extend the theory to finite temperatures, up to the warm dense matter regime.

Modern theory of XAS is based on Fermi's golden rule.[9] The quasiparticle approximation is often used to make the calculation of the many-body cross section tractable. A common approach to evaluate the cross section is to employ ground-state density functional theory (DFT) [11, 10] or the real-space multiple-scattering approach (RSMS) [12, 13]. Exchange-correlation functionals in many DFT implementations are only available for ground-states

which requires additional corrections [17, 14, 16, 15] to the functionals for excited states in the XAS calculation. On the other hand, the RSMS approach uses complex-valued self-energy in place of the ground-state exchange-correlation.

At low temperatures, the exchange-correlation contributions are weakly dependent on temperature. Thus, zero temperature self-energy and exchange-correlation functionals are sufficiently good approximation at low temperature. However, in the warm dense regime, the temperature dependence is crucial to capture the phase transition from the exchange-dominated regime to correlation-dominated regime.[18] However, most codes lacks the treatment of the electron temperature dependence for finite-temperature calculations. Construction of the pseudopotential is often based on the zero temperature exchange-correlation functionals.

These considerations have motivated the work in this thesis. The body of this work consists of four chapters which summarize our contributions to the theory of finite-temperature and non-equilibrium x-ray absorption. In addition to the theoretical developments, which also include the development of finite-temperature self-energy approximations, we have applied the approach to a number of systems, including finite-temperature metals and pump-probe experiments, including validation with experiments.

1.1 Background

1.1.1 X-ray Absorption

X-ray absorption spectroscopy measures the absorption of an incident photon as a function of its energy. From the Beer-Lambert law, the x-ray absorption coefficient $\mu(E)$ is given by

$$\mu(E) = \frac{1}{z} \log \left[\frac{I_t}{I_i} \right] \tag{1.1}$$

for an incident photon with energy $E = \hbar\omega$ on a sample with thickness z. I_i and I_f are the incident and transmitted intensities respectively. The measured quantity $\mu(E)$ is related to the total absorption cross section σ which could be computed from quantum theory:

$$\sigma(E) = \frac{\mu(E)}{c}, \tag{1.2}$$

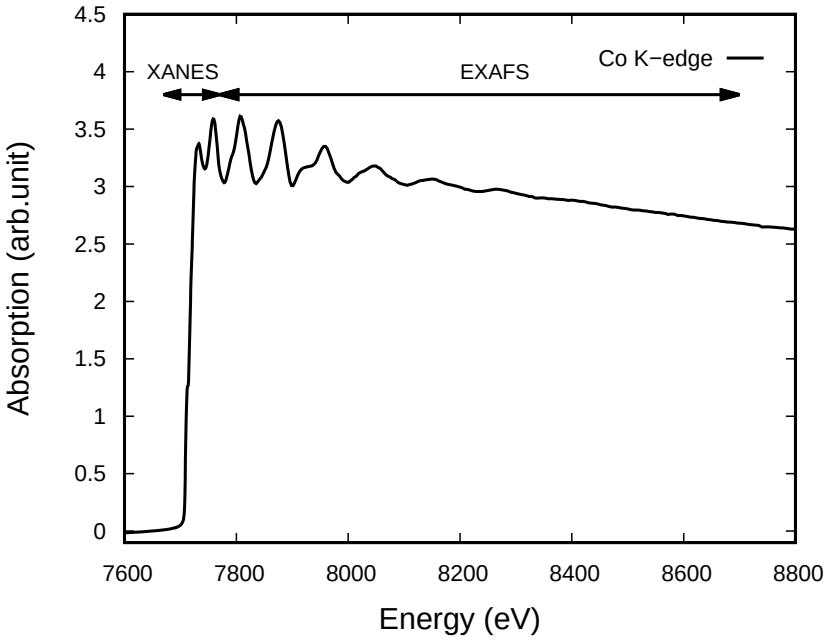

Figure 1.1: Experimental cobalt (Co) K-edge absorption spectrum versus incident photon energy at room temperature.[19]

where c is the concentration of the absorbing atoms. When the incident photon has energy less than the excitation energy of a core electron, E_0, there is no absorption. When $E \approx E_0$, the absorption increases rapidly. We show a typical XAS spectrum in Fig 1.1 for the K-edge of cobalt metal. The spectrum is divided into two regions: XANES and extended x-ray absorption fine structure (EXAFS). The XANES region consists of a raising edge and is dominated by many-body effects which make interpreting the spectra complicated. The EXAFS region consists of decaying oscillations. This is mainly due to the back-scattering interference of the photo-electron by the neighboring atoms. While the theory of EXAFS provides a quantitative description, the analysis of XANES is mostly qualitative due to the complex many-body effects such as shake-up, shake-off, and exciton excitations in the region. The goal in this work is to extend the theory of XAS to finite temperature, as described below.

1.1.2 Warm Dense Matter

Warm dense matter (WDM) is a unique phase of matter that exists in between the hot plasma and cold condensed matter. It exists in many astrophysical objects like white dwarf stars [20, 21], planetary interiors [22, 23] and core of neutron stars [24]. This state of matter can also be found in the early stage of an inertial confinement fusion reaction. This state of matter is currently routinely studied in the lab, e.g. with intense laser sources.[25, 5, 27, 26, 4]

To define WDM, it is often useful to illustrate the phase space that it occupies. Fig 1.2 shows the temperature-density phase space adapted from Ref [28]. The WDM regime has a loosely defined boundary occupying between the regimes of classical statistics and full quantum statistics. This state of matter is characterized by the reduced temperature parameter $\Theta = k_B T/E_F$, plasma coupling parameter $\Gamma = E_c/k_B T$, and the quantum coupling parameter r_s/a_B. Here E_F is the Fermi energy, r_s is the Wigner-Seitz radius, E_c is the Coulomb energy and T is the electron temperature.[29, 30] A state of matter is consider WDM when Γ and r_s/a_B are of order unity. The strong ion couplings and partial degeneracy in the system pose a challenge in simulating WDM. In the condensed matter regime, the low electron temperature allows perturbation corrections to the thermal effects in periodic systems. In hot plasma regime, ions are sparsely separated leading to weak interactions. Quantum statistics can be treated classically with the Maxwell-Boltzmann distribution for most of the plasma properties. However, for WDM, a fully quantum theory is required due to the small spacing between the ions Further, due to the high temperatures low electron temperature perturbation approximation is no longer valid. Therefore, a numerical approach is typically used to accurately treat Coulomb coupling correlations, thermal excitations, and fermionic exchange effects on equal footing as required for WDM.

Finite-temperature DFT [31] and quantum Monte Carlo [32, 29] are commonly used to explore the properties of WDM. At the same time, high temperature plasma models such as the average atom model and hyper-netted-chain have also been adapted to the study of

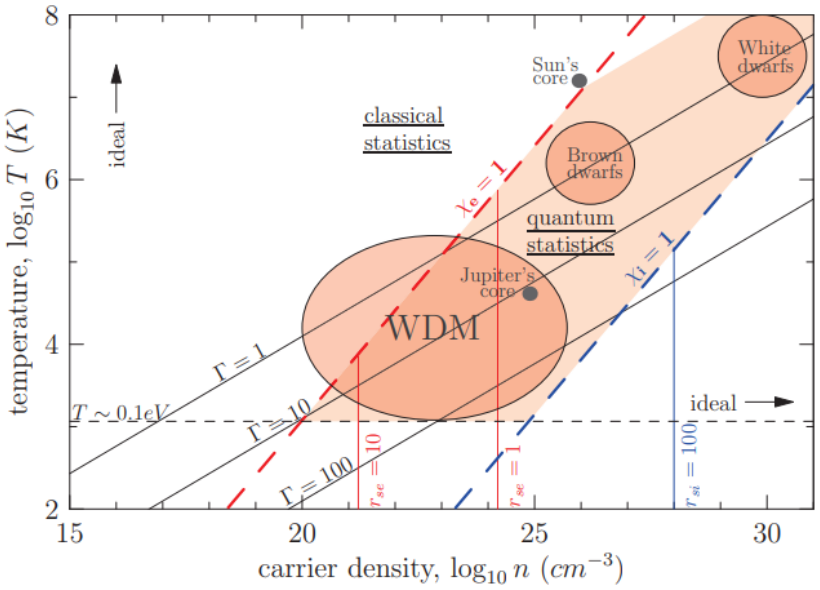

Figure 1.2: Temperature-density phase diagram for two-component plasma adapted from Ref [28]. The separation between the different statistics regime is define by the electron (ion) degeneracy parameter χ_e (χ_i) where $\chi_a = n_a \lambda_D^3$ and the de Broglie wave length $\lambda_D = h/\sqrt{2\pi m_a k_B T_a}$.

WDM [34, 35, 33]. These efforts have led to different parameterizations of the temperature dependent exchange-correlation functional for DFT calculation. However, many current electronic structure calculations for WDM do not include the finite-temperature exchange-correlation corrections. In addition to that, the temperature correction to the electron self-energy for understanding excited-state properties in WDM such as x-ray absorption and thermal conductivity is an ongoing research topic.

On the experimental side, direct measurement of WDM poses a challenge because WDM is opaque to the optical wavelengths and even in the soft x-ray regime. Hence, most experimental studies of WDM require the use of hard x-rays to penetrate the interior of the sample. One of the common x-ray diagnostic methods is x-ray absorption spectroscopy (XAS). Several works [25, 5, 27, 36] are devoted to understanding the edge response in XAS measurements.

Correlations between the spectral features of XAS and the electron temperature have been shown to be a useful diagnostic tool when coupled to a theoretical model. At the same time, extensive testing is still needed to verify the regime of validity of the theoretical models. One of our objectives in this thesis is to make such quantitative comparisons.

1.1.3 Magnetism of Transition Metals

Another goal of our thesis is to treat the effects of magnetism on XAS. In isolated atoms, the existence of magnetism is due to the total angular momentum **J** of partially filled shells. The magnetic moment M_J of an atom is given by

$$M_J = -g_J \mu_B \mathbf{J}, \tag{1.3}$$

where g_J is the Landé-factor and μ_B is the Bohr magneton. M_J of an atom is an integer(half-integer) multiple of μ_B. However, the measured M_J in solids are not. The presence of crystal field effects in solids suppress the orbital angular momentum. Thus, the spin moment is a good approximation to the magnetic moment in solids. For 3d-transition metals, conducting 3d-electrons are the source of magnetism. The d-shell wavefunctions in these metals have non-negligible overlap with neighboring atoms. Historically, there are two major theories to describe the collective phenomenon of magnetism in these metals. Fig 1.3 shows a simplified schematic illustrating the two theories using a collection of spin vectors.

The Stoner model [37] which is an itinerant electron model describes the magnetism within the band structure theory. In this model, the spin majority (up) and spin minority (down) 3d bands are shifted in the opposite direction by the exchange interaction. The size of the exchange spin splitting is determined by

$$\Delta_{ex} = \frac{n_\uparrow - n_\downarrow}{n_\uparrow + n_\downarrow} I, \tag{1.4}$$

where I is the Stoner parameter I and $n_{\uparrow,\downarrow}$ is the spin up(down) density of states.[37] The difference in the spin up and down occupation results in a non-zero net magnetic moment. The magnetic moment can be reduced via the creation of Stoner excitation (electron-hole

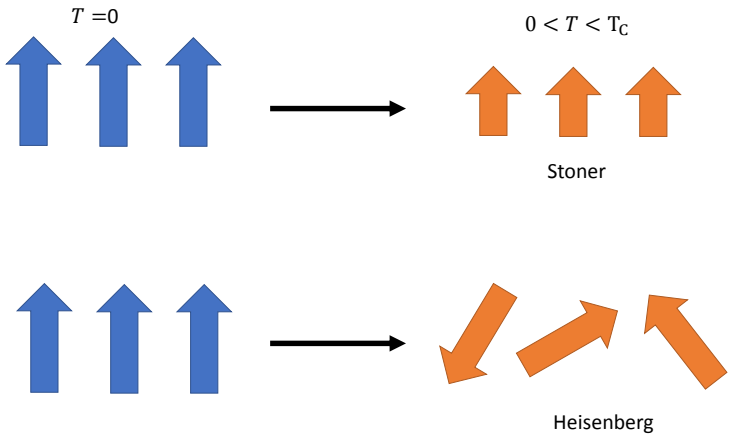

Figure 1.3: A schematic spin vector configuration illustrating the differences between Stoner model and Heisenberg model. The thermal response of Stoner model reduces the overall spin amplitude whereas in the Heisenberg model, a spin disorder is induced.

quasiparticle with opposite spin). This theory is successful in determining the ground state exchange splitting between the Fermi levels of the up and down bands for Fe, Co and Ni. However, it overestimates the Curie temperature and fails to predict the Bloch $T^{3/2}$ law for the magnetization at low temperature.[38]

On the other hand, the Heisenberg model describes the magnetic ordering in terms of localized atomic spin moments at each lattice site. The interaction between the spin at site i, $\mathbf{S}_i$ with the spin at site j, $\mathbf{S}_j$ is given by (ignoring anistropy and antisymmetric contributions) [39]

$$H_{ex} = \frac{1}{2}\sum_{i \neq j} J_{ij}\mathbf{S}_i \cdot \mathbf{S}_j, \tag{1.5}$$

where J_{ij} is the exchange constant. In this picture, the Hamiltonian admits spatial fluctuation solutions of spin moments known as magnons (spin wave). At low temperatures, the magnons contribution to the decrease in the magnetization is proportional to $T^{3/2}$.[38] In this model, the magnon has infinite life-time. A more physical model will allow these

magnons to decay into Stoner excitations. For an accurate description of thermodynamic properties of itinerant magnetism, both stoner excitations and magnons need to be included in the theory.[38]

While the static magnetism in atoms is well understood, ultrafast magnetic dynamics is still an active subject of research. In absent of electron transport, the ultrafast demagnetization measurements for nickel [40, 41] and gadolinium [42] reveal a dominant contribution from Stoner excitations to the demagnetization process, whereas the experiments for iron [43, 44] show transverse spin fluctuation as the dominant channel. A recent experiment for cobalt [45] shows that the long-range disorder due to the magnons and the collapse of exchange splitting have equal contribution to the demagnetization. The transition from $3d^{\uparrow} \rightarrow 3d^{\downarrow}$ in transition metals requires an energy comparable to the exchange splitting Δ_{ex} while a transition from $4sp^{\uparrow} \rightarrow 3d^{\downarrow}$ requires much lower energy [40]. In a typical pump-probe experiment, the electronic temperature could reach about 0.1∼0.2eV. Thus, the collapse of exchange splitting is more energetically favorable in nickel ($\Delta_{ex} \sim 0.2eV$)[46] than in iron ($\Delta_{ex} \sim 2eV$)[44]. It should be noted that the Brillouin zone sampled may differ depending on the spectroscopy methods used in the experiment.

1.2 Goals and Contributions

The main goal of this thesis is to develop the theory of finite-temperature and non-equilibrium x-ray absorption and to extend the current numerical capability for non-equilibrium systems. While there exists similar numerical tools for the calculation of electronic structure, the use of pseudo-potential does not include temperature effects in the exchange-correlation. The temperature correction is important for accurate simulation of warm dense systems. In line with the objectives, we have develop the finite-temperature generalization of the COHSEX approximation to the quasiparticle self-energy. Finally, we implemented several finite-temperature related algorithms in the FEFF10 code for the calculation of finite-temperature XAS. The new implementation enabled us to analyze non-equilibrium systems. Our new implementation has enabled us to analyze the dynamics and finite-temperature properties of a number

non-equilibrium systems, including both electronic, lattice and spin-degrees of freedom.

1.3 Organization of this Dissertation

In chapter 2, we provide an overview of the theory of finite-temperature x-ray absorption. We formulate the conventional theory in the multiple scattering framework and describe the numerical routine for computing the x-ray absorption. In chapter 3, we present an overview of the methods used to model non-equilibrium dynamics of the nuclei and temperatures. We discuss sampling techniques used to generate a set of nuclear configurations that converge to the appropriate limit. Furthermore, we describe the dynamics of electron temperature using the 2-temperature model (2TM) introduced by Anisimov et al. [47] and its extension to include the spin degree of freedom. Next, in chapter 4, we present results for several systems using the FEFF10 code. We compared our density of states calculation for aluminum to those of Ref [48, 35]. In addition, we calculate and compare the XANES for warm dense copper [5] and metal-insulator heterostructure $[Fe/MgO]_8$ [8] to the experiments. In chapter 5, we present the finite-temperature generalization of the quasiparticle electron self-energy within the COHSEX approximation which was originally published in Ref [49]. The COHSEX approximation was introduced as an efficient approximation to the computationally expensive GW self-energy. While it is of interest to include the temperature correction for the excited-state calculation, there has been no analysis into the finite-temperature COHSEX approximation to our knowledge. We present the finite-temperature theory and elucidate the important properties of the theory using the homogeneous electron gas. Finally, in chapter 6, we present the summary of our work and propose areas of future research.

Chapter 2

THEORY OF FINITE-TEMPERATURE X-RAY ABSORPTION

X-ray absorption near edge spectroscopy is a well established tool in many fields ranging from materials science, chemistry, biology and plasma physics. It offers a way to probe the local electronic properties and local atomic structure simultaneously. With the development of ultrafast lasers, the technique has been extended to resolve fast measurements of the order of 10^{-15} ~10^{-12} seconds. The time-resolved x-ray absorption near edge spectroscopy (XANES) allows direct observation of transient physics like spin relaxation and warm dense matter (WDM). However, interpreting the spectra is highly intractable due to the complex nature of XANES. Standard analysis of XANES involves comparison between experimental spectra and numerical simulations.

The modern theory of x-ray absorption (XAS) is based on approximations of the many-body Fermi's golden rule.[9] The quasiparticle approximation is often used to make the calculation of the many-body cross section tractable. Standard approaches to simulating XAS can be divided into two categories: band-structure ground-state density functional theory (DFT) and real-space multiple scattering. The former combines the developed theory of band-structure with ground-state DFT to evaluate the Fermi's golden rule. While the ground-state electronic structure theory is well understood [10, 11], the excited-state theory is still under active investigation. Exchange-correlation functionals in many DFT implementations are only available for the ground states. Many works have been done to introduce corrections to the funtionals for excited states in the XAS calculation.[17, 14, 16, 15] On the other hand, the real-space multiple-scattering approach is an all-electron real-space approach that uses a one-particle Green's function instead of wavefunctions or orbitals. Unlike the DFT approach, a complex valued self-energy is used in place of the ground-state exchange-

correlation which is applicable to the excited states. However, many implementations of the real-space multiple-scattering approach use the spherical muffin-tin (MT) approximations to further simplify the calculations. Progress has been made to extend beyond the MT potential to full potential which is beyond the scope of this thesis.[50, 51]

For finite-temperature calculation of XAS, a finite-temperature theory of electronic structure is required. At low temperature, the exchange-correlation contributions are weakly dependent on the temperature. Zero temperature self-energy and exchange-correlation functionals are sufficiently good approximations at low temperature. However, in the warm dense regime, the temperature dependence is required to capture the phase transition from the exchange- to correlation-dominated behavior.[18] Fig 2.1 shows the exchange ϵ_x and correlation ϵ_c contributions to the the exchange-correlation energy per particle ϵ_{xc} for the homogeneous electron gas model. A crossover from the exchange- to correlation-dominated regime happens close to the Fermi temperature. In this chapter, we present the quasiparticle theory of XAS and its finite-temperature generalization within real-space multiple-scattering framework. We derive the absorption cross section from the Fermi's golden rule and rewrite the expression in terms of a one-particle electron Green's function. Then, we highlight out the relevant changes required for a finite-temperature calculation. In particular, our construction of the muffin-tin potential includes the temperature correction to the exchange-correlation potential. Our current implementation builds upon the theory and FEFF9 code developed by Rehr and coworkers.[52]

The remainder of the chapter is organized as follows: in the next section we review the quasiparticle XAS theory and present the real-space Green's function formalism of the theory. The next section focuses on the implementation of a finite-temperature self-consistent field calculation, followed by a summary of the finite-temperature generalization made within the FEFF10 code. Examples of XANES calculated using our implementation of FEFF10 are presented in chapter 4.

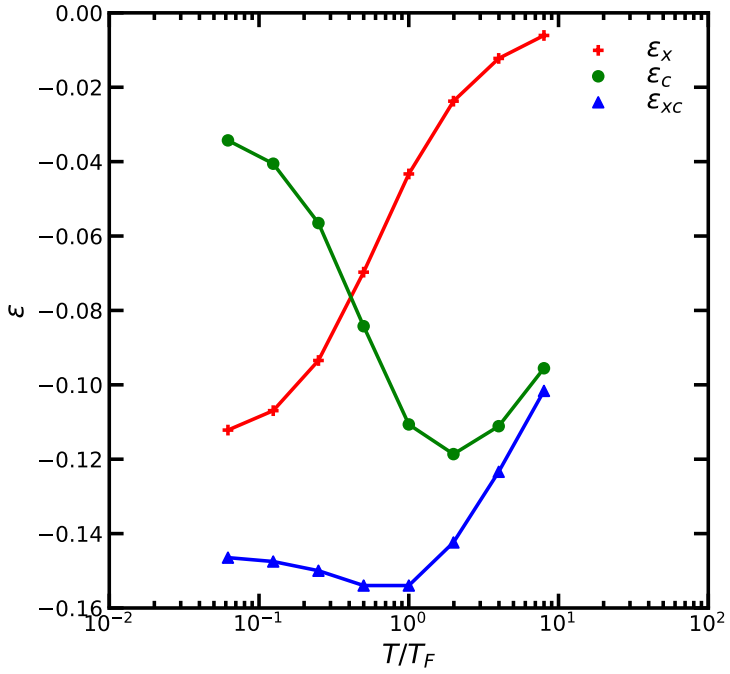

Figure 2.1: The exchange ϵ_x and correlation ϵ_c contributions to the the exchange-correlation energy per particle ϵ_{xc} versus temperature for the homogeneous electron gas model adapted from Ref [18].

2.1 Quasiparticle XAS

In this section, we briefly describe the quasiparticle theory of XAS. While the theory ignores some many-body effects such as multi-electron excitations, it includes a dynamic self-energy and the effect of lattice vibrations and disorder. The quasiparticle theory has been successful at reproducing many experimental result qualitatively.

The absorption cross section σ for a material can be computed via Fermi's golden rule in atomic unit (m_e=e=$\hbar$=1)

$$\sigma(\omega) = 4\pi^2 \frac{\omega}{c} \sum_{I,F} |\langle I|\hat{D}|F\rangle|^2 \delta(\omega + E_I - E_F) \tag{2.1}$$

where $|I\rangle$ is the many-body ground state with energy E_I, $|F\rangle$ is the many-body excited state

with energy E_F and $\hat{D}$ is the many-body excitation operator by the x-ray field.

Next, we make two assumptions to the above many-body formula to simplify the calculation. We assume that electrons are independent particles such that the excited electron can be separated from other electrons. Hence, we can approximate the many-body states as $|I\rangle = |\phi_c\rangle \otimes |\Phi_0^{N-1}\rangle$ and $|F\rangle = |\phi^k_{photoelectron}\rangle \otimes |\Phi_n^{N-1}\rangle$ where $|\Phi_n^{N-1}\rangle$ is the n^{th} excited state of the N-1 electrons system and $|\phi_c\rangle$ is the single-electron core state. The second assumption is that the electron-photon coupling is mediated by the dipole interaction, $\hat{d} = \sum_{i,f} d_{ij}\hat{a}_f^\dagger \hat{a}_i$. This transforms Eq. (2.1) into an effective single-particle cross section [53]

$$\sigma_{QP}(\omega) = 4\pi^2 \frac{\omega}{c} S_0^2 \sum_{i,f} |\langle i|\hat{d}|f\rangle|^2 \delta(\omega + \epsilon_i - \epsilon_f) \tag{2.2}$$

where $S_0^2 = |\langle \Phi_0^{N-1}|\Phi_0^{N-1}\rangle|^2$ is the amplitude reduction factor. ϵ_i and ϵ_j are the eigenenergy for quasiparticle $|i\rangle$ (deep-core) and $|f\rangle$ (photo-excited) states. Within the independent particle picture, a core-electron leaves behind a hole after being excited into the photo-electron state. Thus, the final state is modified by the interaction with the core hole potential.

2.2 Green's Function Approach

We adopt the real-space Green's function formalism to overcome the computational bottleneck of the double sum and the translational symmetry requirement in Korringa-Kohn-Rostoker (KKR) band structure method.[52] The retarded single-electron Green's function, $G^R_{l'j',lj}$ at site j with angular momentum l is given by[17]

$$G^R_{l'j',lj}(E) = \sum_{fll'} |l'j'\rangle \frac{\langle l'j'|f\rangle\langle f|lj\rangle}{E - \epsilon_f + i\Gamma} \langle lj| \tag{2.3}$$

$$-\frac{1}{\pi}\text{Im } G^R_{l'j',lj}(E) = \sum_{fll'} \langle l'j'|f\rangle\langle f|lj\rangle \delta(E - \epsilon_f) |l'j'\rangle\langle lj| \tag{2.4}$$

where Γ is the core hole life time, ε_f is the eigenenergy of the final-state Hamiltonian $H' = p^2/2 + V_f + \Sigma(E)$, V_f is the effective one electron Coulomb potential in the presence of a screened core hole and Σ is the dynamically screened electron self-energy. By inserting G^R

into Eq. (2.2), the final states are implicitly summed in the calculation of σ_{QP}

$$\sigma_{QP}(\omega) = -4\pi\frac{\omega}{c}S_0^2\mathrm{Im}\sum_{ill'}\langle i|\hat{d}\ G^R_{l0,l'0}(\omega+\epsilon_i)\ \hat{d}^\dagger|i\rangle f_T(\epsilon_i)\Big(1-f_T(\omega+\epsilon_i)\Big) \tag{2.5}$$

where site 0 is the absorbing atom, $f_T(E) = 1/\Big(1+\exp[(E-\mu)/k_BT]\Big)$ is the Fermi-Dirac distribution and μ is the chemical potential of the final system. The distribution $1-f_T$ accounts for the unoccupied states. For T $>$ 0, the Fermi surface is not well defined and the chemical potential can lie below the Fermi level. Eq. (2.5) depends explicitly on the temperature through f_T and depends implicitly on the temperature through the self-consistent calculation of G^R. For deep core excitation, the single-particle state is a good approximation to the initial state and for most cases, the initial excitation involves only a single state.

From here onward, we will drop superscript for G. Using the multiple-scattering theory, G can be expanded in terms of the free propagator G^0

$$G = G^0 + G^0VG \tag{2.6}$$

$$= G^0 + G^0VG^0 + G^0VG^0VG^0 + \ldots \tag{2.7}$$

An alternative decomposition of the potential V into a superposition of atomic potentials $\sum_i v_i$ allows us to separate the site-centered contribution G_c and the scattering contribution G_{sc}[54]

$$G = G^0 + G^0TG^0 + G^0TG^0TG^0 + \ldots \tag{2.8}$$

$$= G^c + \sum_{i\neq c} G^ct_iG^c + \sum_{i,j\neq c} G^ct_iG^0t_jG^c \tag{2.9}$$

$$= G^c + G^{sc} \tag{2.10}$$

where $G^c = G^0 + G^0t_cG^c$ and $T = \sum_t t_i$ is the local scattering matrix with contribution $t_i = v_i + v_iG^0t_i$ at site i. In the multiple-scattering expansion, the contributions to the EXAFS converges rapidly with increasing order. However, for XANES an infinite summation of the series is required. It can be shown that the sum of the series G^{sc} is given by[13]

$$G^{sc} = \Big(1-\bar{G}^0T\Big)^{-1}G^0 \tag{2.11}$$

where $\bar{G}^0$ is the Green's function whose diagonal terms are zeros to exclude self-scattering contributions.

2.2.1 Constructing Green's Function

The construction of the full Green's function involves solving the single site Dirac-Fock equation to obtain the phase shifts δ_{Ln} and regular spinor solutions R_{Ln} (irregular solution H_{Ln}). The details for the derivation can be found in Ref [13, 54]. The full Green's function is then [54]

$$\begin{aligned} G(r, r', E) &= -2k\Big[\sum_{LL'} H_{Ln}(r_>)R^{\dagger}{}_{L'n'}(r_<)\delta_{LL'}\delta_{nn'} + \\ &\quad R_{Ln}(r_n)e^{i\delta_{Ln}}\bar{G}^{sc}_{Ln,L'n'}e^{i\delta_{L'n'}}R^{\dagger}{}_{L'n'}(r'_n)\Big] \end{aligned} \tag{2.12}$$

where the labels n is the site nearest to r, $r_n = r - \mathbf{R}_n$ where $\mathbf{R}$ is the center of site n and $r_<(r_,>)$ is the min$[r,\ r']$ (max$[r,\ r']$). The prefactor k is determined from the Wronskian between the regular solution and the irregular solution.[54]

2.3 Finite-Temperature Self-consistent Field Potential

In this section, we outline the procedure for computing a self-consistent muffin-tin potential for the construction of the full Green's function. The initial charge density is constructed from the atomic electron densities from solving the relativistic Dirac-Fock equation within the muffin-tin (MT) approximation. Then, the density is used to construct a new set of potentials $V = V^{MT}_{coulomb}(\rho_{old}) + V_{xc}(T)$ and a new chemical potential, $\mu(T)$. The static exchange-correlation potential $V_{xc}(T)$ is added to account for the finite-temperature ground-state electron correlation effect. For the final-state calculation, $V^{MT}_{coulomb}$ is replaced with a non-hermitian Coulomb potential in the presence of a core hole. The self-consistent field (SCF) calculation is terminated when the charge neutrality condition within the Norman radius is satisfied. The SCF subroutine is summarized as follows

1. Compute atomic density ρ_{old} and chemical potential $\mu(T)$ by solving the relativistic Dirac-Fock equation.

2. Construct a new potential $V = V^{MT}_{coulomb}(\rho_{old}) + V_{xc}(T)$.

3. Compute a new density ρ_{new} and a new chemical potential $\mu_{new}(T)$.

4. Update the old density $\rho_{old} = \alpha\rho_{old} + (1-\alpha)\rho_{new}$ with some mixing parameter α.

5. Repeat steps 2 - 4 until the charge neutrality condition is satisfied.

For the case of spin polarized density, we follow the von Barth-Hedin prescription [55] where the source of magnetization is mainly due to the atomic magnetization. In this case, we consider only the spins from partially filled d and f states to construct the initial atomic densities from a given spin configuration. Mattern [56] extended the SCF to finite-temperature in his thesis for the study of non-resonant inelastic x-ray scattering. However, the code is not publicly available.

2.3.1 Contour Integration

Within the finite-temperature SCF procedure, the electron density $\rho(r)$ is computed. The electron density depends on the temperature implicitly via the SCF. It can be obtained $\rho(r)$ from the spectral relation of the Green's function G

$$\rho(r, r', E) = -\frac{1}{\pi}\text{Im } G(r, r', E) \tag{2.13}$$

The electron density $\rho(r)$ can be easily obtained by integrating the Green's function G.

$$\rho(r) \;\; = \;\; -\frac{2}{\pi}\int_{E_B}^{\infty} dE \text{ Im } G(r, r, E) f_T(E-\mu) \tag{2.14}$$

The factor of 2 accounts for the spin degeneracy. The integral extends from some energy level E_B above the core states but below the valence states to infinity (usually some large cutoff). However, a direct integration of G can be problematic since there are singularities along the

real energy axis. A typical approach is to extend the integral to the complex energy plane where the excitation structures are smeared out. In the complex plane, the integrals can be decomposed into a sum of Matsubara poles and a smooth complex line integral.[57]

$$\begin{aligned}\rho(r) &= -\frac{2}{\pi}\int_C d\omega \ \mathrm{Im}\ G(r,r,\omega) f_T(\omega-\mu) \\ &\quad +4i\ \mathrm{Im}\ \sum_{i=1}^{N} \mathrm{Res}[G(r,r,z_i) f_T(z_i-\mu)] \end{aligned} \tag{2.15}$$

where $z_j = \mu \pm i\pi(2j-1)kT$ are the Matsubara poles and N is the number of poles enclosed by contour C and the real axis. The contour C is shown in Fig 2.2. When the height of the contour C passes the middle of two adjacent Matsubara poles, the Fermi-Dirac distribution takes the same value as on the real axis. A few number of points are needed to integrate the first term because G changes slowly with energy. As example, we computed the density of states for copper along different heights in Fig 2.3. The highly oscillating features are broadened out with increasing height. The complex contour integration is also used to evaluate Eq. (2.5).

2.4 Core Hole Lifetime and Instrumental Broadening

The quasiparticle cross section calculated via Eq. (2.5) does not account for the finite lifetime of the core hole. The decay of the core hole broadens the linewidth of the cross section. The effective cross section is a result of a convolution between quasiparticle cross section σ_{QP} with a Lorentzian of width $\Gamma_{corehole}$. The finite resolution of detector is treated similarly with a Lorentzian of width $\Gamma_{detector}$.

$$\sigma_{eff}(\omega) = \int d\omega' \sigma_{QP}(\omega') \frac{\pi/\Gamma}{(\omega-\omega')^2+\Gamma^2} \tag{2.16}$$

$$\begin{aligned} &= -4\pi\frac{\omega}{c} S_0^2 \mathrm{Im} \sum_{ill'} f_T(\epsilon_i) \int d\omega' \frac{\pi/\Gamma}{(\omega-\omega')^2+\Gamma^2} \\ &\quad \times \langle i|\hat{d}\ G_{l0,l'0}(\omega+\epsilon_i)\ \hat{d}^\dagger|i\rangle \Big(1-f_T(\omega+\epsilon_i)\Big) \end{aligned} \tag{2.17}$$

where $\Gamma = \Gamma_{corehole} + \Gamma_{detector}$.

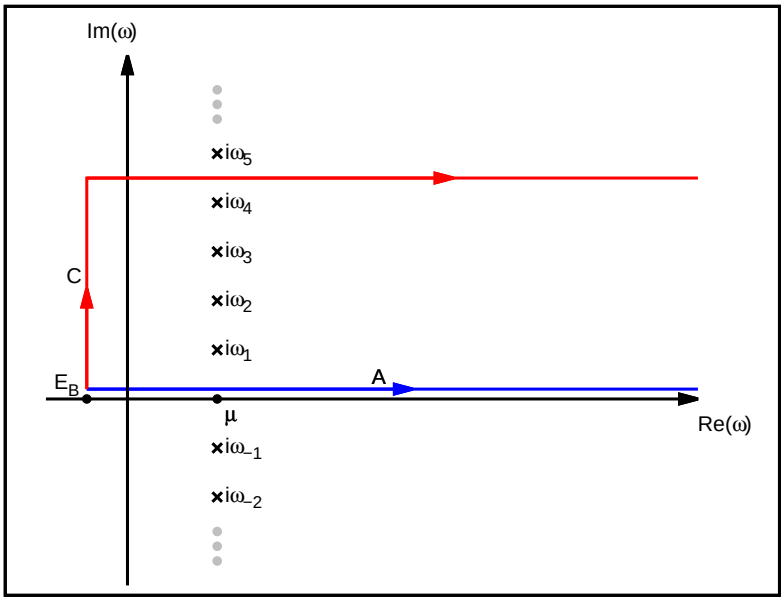

Figure 2.2: Energy contour for electron density calculation at temperature T>0. Here, $\omega_j = \pi(2j-1)kT$ denotes the imaginary part of the Matsubara poles of $f_T(E,\mu)$. The integration starts from some energy level E_B above the core states but below the valence states. Contour A (blue) represents the original integration path along the real axis while contour C (red) represents the integration path in the imaginary plane.

2.5 Finite-temperature X-ray Spectroscopy Code FEFF

In this section, we summarize our implementation of the finite-temperature XAS calculation in FEFF10. FEFF10 is a x-ray spectroscopy code that uses the relativistic real-space Green's function approach based on quasiparticle approximation and spherical muffin-tin potential approximation.

This code takes a set of Cartesian coordinates for the nuclei and the charges as input. Then, the atomic densities are computed for each unique species from the Dirac-Fock equation. Next, the spherical MT potential, the chemical potential and Green's function are

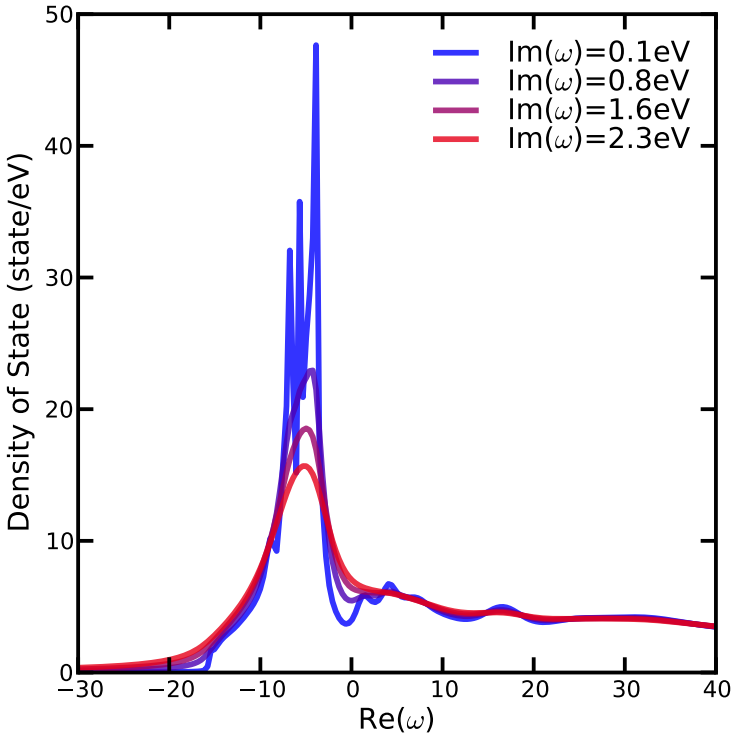

Figure 2.3: Example of a density of state $\rho(\omega)$ along different height in the complex plane. The imaginary part of ω increases from blue to red.

determined self-consistently from the overlapping atomic potentials from the atomic densities. Once self-consistency is achieved, the absorption is computed and convolved with the a Lorentzian. The control cards for the finite-temperature XANES subroutines are documented in Appendix C.

In this code, the KSDT exchange-correlation potential [32] for the construction of the muffin-tin potential. A shortcoming of the current implementation is the use of the Hedin-Lundqvist dynamically screened self-energy $\Sigma(T = 0)$ for the excited states.[58] Currently, there is a lack of efficient parameterization for $\Sigma(T > 0)$. Work is in progress to develop an accurate parameterization of the self-energy based on our work in chapter 5.

2.6 Summary

We presented the theory of finite-temperature quasiparticle XAS. The theory is based on the generalization of the standard theory of quasiparticle XAS. The self-consistent muffin-tin potential accounts for the temperature correction through the use of temperature dependent exchange-correlation potential such as the KSDT parameterization for the homogeneous electron gas.[32] This generalization of the potential improves the ground-state wavefunction calculation needed for the construction of the free one-particle Green's function. Next, the electron self-energy is generalized to a finite-temperature self-energy within the Matsubara formalism. This generalization is crucial for the XAS since it accounts for the temperature correction to the final-state effects. A feasible calculation of the XAS requires an efficient implementation of the finite-temperature self-energy. The final modification to the standard theory of the XAS is the smearing of the Fermi level. At finite temperature, the Fermi level is no longer well defined and the contributions of states below the chemical potential are weighted according to the Fermi-Dirac distribution. In summary, the theory of finite-temperature quasiparticle XAS is a generalization of the standard theory of XAS to include the electron temperature response but it does not account for the dynamic response of the atomic structure which will be addressed in chapter 3.

Implementation of the finite-temperature theory is straightforward, provided an accurate parameterization of the finite-temperature exchange-correlation potential and the finite-temperature self-energy are available. We implemented the theory on top of the FEFF9 code by Rehr et al.[52] In our implementation, we use the KSDT exchange-correlation potential [32] for the construction of the muffin-tin potential. Further details and example calculations are given in Appendix C. Due to a lack of finite-temperature parameterization of the electron self-energy, our code uses the zero-temperature Hedin-Lundqvist self-energy. However, the temperature correction is weakly dependent on the temperature when the temperature is below the Fermi temperature.[18] In order to validate the theory, the approach has been applied in a number of cases and compared with quantitative experiments in chapter 4.

Chapter 3

MODELING OF NON-EQUILIBRIUM DYNAMICS

The theory of finite-temperature XAS introduced in chapter 2 addresses the electronic response of a sample for a fixed structure. Since most physical systems are probed under non-zero temperature conditions and possibly laser excitations, a static theory may not always describe the real world. The dynamic response of the lattice is usually characterized by the attenuation of the measured intensity. Lattice vibrations can also induce forbidden electronic transitions which result in non-trivial changes to the XANES such as additional pre-edge structure.

The advances in calculation electron-phonon interactions from first principles has made it possible to calculate XAS at finite lattice temperature.[59] Here, we briefly describe two approaches, molecular dynamics and Monte Carlo sampling to calculate XAS at finite lattice temperature. They do not require direct calculation of electron-phonon coupling matrix elements and combine naturally with the theory of finite-temperature XAS without any modification. Thus, these methods also allow the treatment of non-equilibrium electron and lattice systems.

The introduction of electron and lattice temperature introduces additional parameters to the theory. The temperatures are known accurately for samples in thermal equilibrium but they are usually approximated when probing non-equilibrium samples. Short pulse laser can heat electrons to a very high temperature in a short time driving the sample out of equilibrium. To analyze the XAS, the energy transport from the hot electron to other subsystems of the sample is required to accurately describe the evolution of the temperatures. Historically, the first model proposed to study the transfer of energy between the electrons and lattice is introduced by Anisimov et al.[47] The model is called two-temperature model

due to the two degrees of freedom assumed in the model. The dynamics of the electron and lattice temperatures are governed by the conservation of laws and are derived from the Boltzmann equation. The works of Allen[60], and Qiu et al.[61, 62, 63] contributed the understanding of heat transfer in metals.

In this chapter, we present an overview of the techniques required to extend the analysis of finite-temperature XAS to non-equilibrium systems. We first describe the ab initio molecular dynamics and Monte Carlo sampling method for the calculation of XAS at finite temperature. Next, we introduce the two-temperature and three-temperature models to describe the ultrafast thermal response of the electron and lattice.

3.1 Effects of Thermal Disorder

In the experiments, the thermal average of the x-ray absorption $\langle\sigma(E)\rangle_T$ is measured. The lattice vibrations can induce forbidden electronic transitions which result in additional pre-edge structure in XANES. If we know exactly the probability distribution $P(\mathbf{R})$ that generates the atomic configuration $\mathbf{R}$, then we can evaluate the absorption. However, $P(\mathbf{R})$, in general, is hard to compute. The most common approach to approximate the average is to numerically approximate $P(\mathbf{R})$ by importance sampling.

$$\langle\sigma(E)\rangle_T = \int d\mathbf{R}\ \sigma(E;\mathbf{R})P(\mathbf{R}) \tag{3.1}$$

$$\approx \frac{1}{S}\sum_{i=1}^{S}\sigma(E;\mathbf{R}_i) \tag{3.2}$$

where S is the total number of atomic configurations. Therefore, in this section, we briefly describe two methods for generating the atomic configuration samples: ab initio molecular dynamics (AIMD) and the Monte Carlo sampling of dynamical matrix method.

Classical lattice vibrations and anharmonic effects are readily included in AIMD [64] when the temperature is much greater than the vibrational frequency. This method is widely used in the analysis of warm dense matter and liquid systems [65, 5, 66, 26, 67]. At low temperatures where quantum zero-point motion dominates, methods such as path integral molecular dynamics (PIMD) [68], phonon spectral convolution [69, 70] and Monte Carlo vibrational

mode sampling of dynamical matrix [71, 72] have been used to describe the nuclear motion in XANES. Depending on the precision required, different methods are employed for maximal computation efficiency.

3.1.1 Ab Initio Molecular Dynamics

In the AIMD method, the electron dynamics is treated quantum mechanically while the nuclei positions are updated classically using Newton's second law from the forces exerted by the electrons via Hellmann–Feynman theorem [73]. For a system consisting of nuclei with position vectors $\mathbf{R}$ and electrons with position vectors $\mathbf{r}$, the associated Hamiltonian is given by

$$H(\mathbf{r},\mathbf{R}) = T_N + T_e + V_{ee}(\mathbf{r}) + V_{NN}(\mathbf{R}) + V_{eN}(\mathbf{r},\mathbf{R}) \tag{3.3}$$

where T is the kinetic operator for the nucleus and electron, V_{ee} is the electron-electron repulsion, V_{NN} is the nucleus-nucleus repulsion and V_{eN} is the electron-nucleus attraction. Given that the mass of the nucleus is several orders larger than the mass of the electrons, we can decouple the wavefunctions of the nuclei $\psi(t,\mathbf{R})$ and the electrons $\phi(\mathbf{r})$ provided that the kinetic energy of the nuclei is much smaller than the electrons. Therefore, we end up with a coupled equation that can be solved iteratively.

$$\Big[T_e + V_{ee}(\mathbf{r}) + V_{eN}(\mathbf{r},\mathbf{R})\Big]\phi(\mathbf{r}) = \epsilon(\mathbf{R})\phi(\mathbf{r}) \tag{3.4}$$

$$\Big[T_N + V_{NN}(\mathbf{R}) + \epsilon(\mathbf{R})\Big]\psi(t,\mathbf{R}) = \frac{\partial}{\partial t}\psi(t,\mathbf{R}) \tag{3.5}$$

where ϵ is the eigenenergy of the many-electron wavefunction $\phi(\mathbf{r})$. ϵ is found using density functional theory [11, 10] at the ground-state configuration $\mathbf{R}^{(t-1)}$ of the previous time step $t-1$. Instead of solving Eq. (3.5) quantum mechanically, it is solved using Newton's second law and Hellmann–Feynman theorem. The force on a nucleus with mass M_i at position $\mathbf{R}_i$ can be written as

$$M_i\frac{d^2\mathbf{R}_i}{dt^2} = -\frac{\partial}{\partial\mathbf{R}_i}\langle\phi_0|\Big[T_e + V_{ee}(\mathbf{r}) + V_{eN}(\mathbf{r},\mathbf{R})\Big]|\phi_0\rangle \tag{3.6}$$

where ϕ_0 is the ground state of Eq. (3.4). In this picture, the nuclei evolve along the minimum of Born-Oppenheimer (BO) potential energy surface.

The molecular dynamics at finite temperature can be performed in the microcanonical ensemble settings where the number of particles, the total volume and total energy are fixed. One simple method is called velocity rescaling introduced by Woodcock.[74] The initial velocities are randomly assign to the nuclei such that they satisfies the thermodynamic relation

$$\langle E_K \rangle = \frac{3}{2} N k_B T \tag{3.7}$$

where E_K is the kinetic energy, N is the total number of atoms and k_B is the Boltzmann constant. Then, the velocities are adjusted by a factor $\sqrt{T/T_{current}}$ when the current average temperature $T_{current}$ is much greater or less than the desired temperature T. While this method is fast and simple, it fails to produce the correct canonical ensemble. Andersen [75] was the first to propose a scheme called Andersen thermostat that guarantees the correct canonical distribution. The nuclei interacts with a heat bath randomly with some specified collision probability. When a nuclei interacts or collides with the heat bath, it is assigned a new velocity sampled from the Maxwell-Boltzmann distribution.

Since then many other schemes such as Langevin dynamics [76], Berendsen thermostat [77] and Nosé-Hoover thermostat [79, 78] have been proposed. Nosé-Hoover thermostat is the most common thermostat used today. The scheme is deterministic and generates the correct canonical ensemble. The algorithm uses an auxiliary system consisting of a single particle with mass Q, position s, and velocity $\dot{s}$ in a potential $3k_BT\log(s)$. The potential is chosen such that the correct canonical ensemble is obtained. The position s is a scaling factor for transforming the time τ in the auxiliary system to the physical time t: $d\tau = sdt$. Therefore, the molecular dynamics simulation at constant temperature using the Nosé-Hoover thermostat is governed by the Hamiltonian

$$H = s^2 \sum_i \frac{M_i}{2} \dot{\mathbf{R}}_i^2 + V(\mathbf{R}) + \frac{1}{2} Q \dot{s}^2 + 3k_B T \log(s) \tag{3.8}$$

where the first and second terms are the kinetic energy and potential energy of the physical system and the third and fourth terms are the kinetic energy and potential energy of the Nosé-Hoover thermostat. The auxiliary mass Q is generally set close to the center frequency of phonon spectrum. If Q is too large, the phase-space sampling will be inefficient. If Q is too small, the physical system will decouple from the thermostat.[79]

3.1.2 Monte Carlo Vibrational Mode Sampling

While AIMD is able to simulate the lattice dynamics for various state of matter, AIMD can be computationally expensive due to the small time step required. Monte Carlo vibrational mode sampling (MCVMS) method provides an alternative method for sampling the configuration space at a lower cost as long as the harmonic potential approximation holds. In addition, a subset of modes can be selectively excited using MCVMS to study the effects of non-equilibrium phonons.

Within the Born-Oppenheimer (BO) approximation, small perturbation to the nuclear configuration can be approximated using the harmonic approximation. Hence, at equilibrium configurations R_0, the Hamiltonian for the nucleus is given by (spectrum is shifted by $\varepsilon(R)$) [80]

$$H \approx \sum_{\alpha} \frac{P_\alpha^2}{2M_\alpha} + V^{BO} + \frac{1}{2}\sum_{\alpha,i}\sum_{\alpha',i'} \left.\frac{\partial^2 V(x)}{\partial u_{\alpha,i}\partial u_{\alpha',i'}}\right|_{x=R_0} u_{\alpha,i}u_{\alpha',i'} \tag{3.9}$$

where P_α is the momentum of the nuclei, M_α is the mass, $V^{BO} = V(R_0)$ is the constant BO potential energy surface and $u_{\alpha,i}$ is the displacement of α-th nucleus in the i-direction. The second derivative of V is called the inter-atomic force constant which will be denoted by Φ. Another useful quantity is called the dynamical matrix D [80]

$$D_{\alpha i,\alpha' i'}(\mathbf{q}) = \sum_n \frac{\Phi_{\alpha i,\alpha' i'}}{\sqrt{M_\alpha M_{\alpha'}}} e^{i\mathbf{q}\cdot\mathbf{R}_n} \tag{3.10}$$

where $\mathbf{R}_n$ is the Bravais lattice. D is Fourier transform of the mass normalized Φ and its eigenvalue problem

$$\sum_{\alpha' i'} \left(D_{\alpha i,\alpha' i'}(\mathbf{q}) - \delta_{\alpha i,\alpha' i'}\omega_\mu^2(\mathbf{q}) \right) \varepsilon^{(\mu)}_{\alpha' i'}(\mathbf{q}) = 0 \tag{3.11}$$

defines the $3N$ vibrational modes of the system. In a solid crystal, there are $3N-3$ modes due to translation symmetry. The eigenvectors $\varepsilon^{(\mu)}_{\alpha' i'}$ are also called the normal modes. The dynamical matrix can be computed numerically by a finite difference method or using density functional perturbation theory.[82, 81] Additional details on the derivation of the eigenvalue problem can be found in Appendix B along with its connection to the Debye-Waller factor.

Once the dynamical matrix is obtained, a set of configurations can be generated by the following displacement [71]

$$u_{\alpha i} = \frac{1}{\sqrt{M_\alpha}} \sum_{\mu=1}^{3N} a_\mu x_i^\mu \varepsilon_{\alpha i}^\mu \tag{3.12}$$

where $a_\mu = \sqrt{\frac{1}{2\omega_\mu} \coth\left(\beta\hbar\omega_\mu/2\right)}$ is the normal length, x_i^μ is a standard normal random variable and $\varepsilon_{\alpha i}^\mu$ is the eigenvector of the real-space dynamical matrix D. A sufficiently large real-space supercell is required to include all the relevant long wavelength modes. This method can also be extended to include thermal expansion effects via the quasi-harmonic approximation.

3.2 Dynamic Response Approximations

Phenomenological models [47] have been studied and used in analyzing ultrafast relaxation processes. Allen [60] extended the Ansimov's model to metals. Since then, TTM has been extended to include spins[7, 83, 84], non-thermal phonons[85] and non-thermal electrons[86].

3.2.1 2-Temperature Model of Dynamic Response

Here, we focus on the 2TM model proposed by Anisimov et al. [47] for metallic system where the electronic heat capacity (C_e) is much smaller than the lattice heat capacity (C_l). In the two-temperature model (2TM), we are assuming that there are two thermal reservoirs (T_e & T_l) in the system under investigation. This assumption is justified in many cases since the thermalization of electron gas is of order of ~100 fs. The next assumption is the electron-electron scattering and phonon-phonon scattering proceed at a much rapid rate than the

electron-phonon scattering. Under these assumptions, it is valid to describe the occupations of the electrons and phonons by their respective local equilibrium distributions f_e and f_l.

$$f_e(E) = \frac{1}{1+e^{\beta(E-\mu)}} \tag{3.13}$$

$$f_l(\omega) = \frac{1}{e^{\beta\hbar\omega}-1} \tag{3.14}$$

The energy balance equations of the electron and lattice subsystems give the spatial temporal dynamics of the electronic and lattice temperatures in a set of coupled non-linear differential equation [47, 87]:

$$C_e\frac{dT_e}{dt} = \nabla[K_e(T_e)\nabla T_e] - G_{el}(T_e - T_l) + P(t) \tag{3.15}$$

$$C_l\frac{dT_l}{dt} = \nabla[K_l(T_l)\nabla T_l] + G_{el}(T_e - T_l) \tag{3.16}$$

where $C_{e,l}$ are the heat capacities of the electrons and lattice, $K_{e,l}$ are the thermal conductivities of the electrons and lattice, G_{el} is the electron-phonon coupling factor, and P is the laser source term. P is usually modelled with a temporal Gaussian profile. In many studies, the traverse thermal gradients are ignored because of the relatively long time scale of the heat propagation given a typical beam spot diameter of order ~10 μm. Longitudinal temperature gradients are also neglected in thin film samples. The parameters C_e and G_{el} in 2TM have been computed from first principle by Lin et al. [87] for various metals based on Allen's electron relaxation theory [60] for metals.

Fig 3.1 shows an example 2TM calculation for a copper foil system described in Ref [5]. The heat diffusion in Eq (3.15) and Eq (3.16) are ignored. The parameters for C_l is chosen to be 3.5 $\times 10^6$ J/m^{3}K as in Ref [5] while C_e and G_{el} are taken from Ref [87]. The laser source $P(t)$ is modeled with Beer-Lambert law for a Gaussian profile 400 nm laser incident on a 70 nm thick copper foil. The lattice response quickly to the changes in the electron temperature due to the strong electron-phonon coupling G_{el} and proceeds to equilibrate over ~10 ps. Knowing the electron temperature evolution can help to initialize a grid search for fitting the temperature in a XAS calculation.

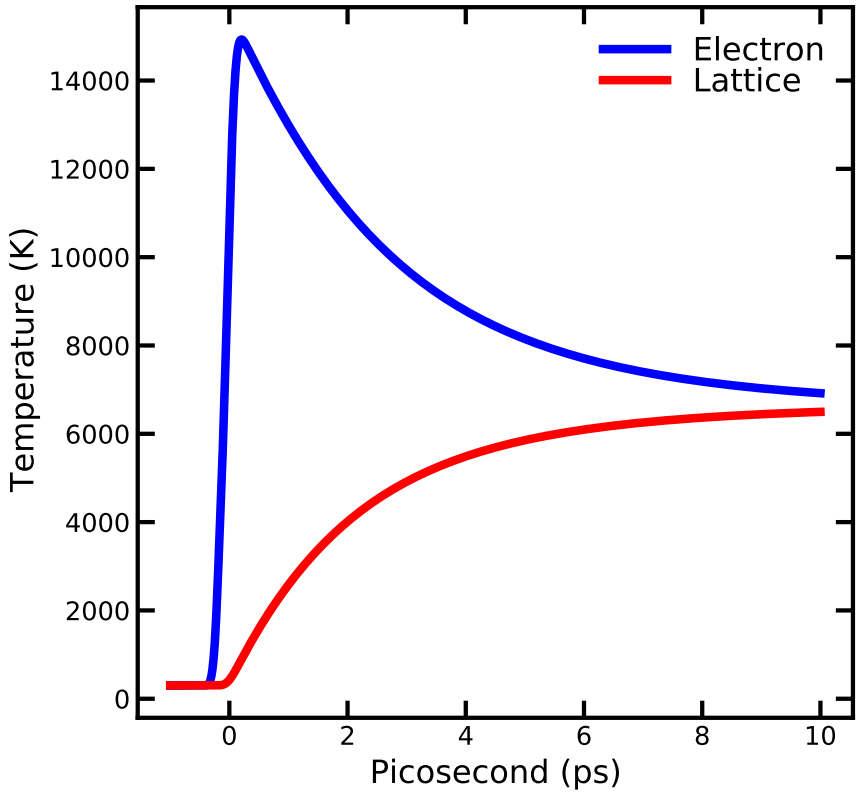

Figure 3.1: Dynamics of electron temperature (blue) and lattice temperature (red) based on two-temperature model calculation. The absorption power is calculated using Beer-Lambert law for a Gaussian profile 400 nm laser source for a 70 nm thick copper.

.

3.2.2 3-Temperature Model of Spin Dependent Systems

The 2TM model can be easily extended to N-temperature models. For the case of spin polarized system, a 3TM model is often adopted to analyze the system. In the most general

form, the 3TM is written as

$$C_e\frac{dT_e}{dt} = \nabla[K_e(T_e)\nabla T_e] - G_{el}(T_e - T_l) - G_{es}(T_e - T_s) + P(t) \quad (3.17)$$

$$C_l\frac{dT_l}{dt} = \nabla[K_l(T_l)\nabla T_l] + G_{el}(T_e - T_l) - G_{ls}(T_l - T_s) \quad (3.18)$$

$$C_s\frac{dT_s}{dt} = \nabla[K_s(T_s)\nabla T_s] + G_{es}(T_e - T_s) + G_{ls}(T_l - T_s) \quad (3.19)$$

Beaurepaire et al.[7] were the first to use the 3TM to describe the experimental measurement of ultrafast demagnetization in ferromagnetic nickel. Although the three-temperature model (3TM) was based on phenomenological model, it is successful to predict the electron spin relaxation process.[7] Recent works [88, 89] have derived the coupling factors G from atomic spin models.

3.3 Summary

We have introduced AIMD and Monte-Carlo vibrational mode sampling method as approximations to the lattice dynamics for the calculation of x-ray absorption theory presented in chapter 2. Vibrational mode sampling is suitable for modeling the vibronic effects below the melting point as long as the quasi-harmonic approximation holds. The method is computationally cheap to produce many random configurations for various temperatures from a single dynamical matrix calculation. AIMD is able to model lattice dynamics for various phases of matter when coupled with a suitable thermostat. In addition, anharmonic effects are included implicitly in the calculation. High quality samples (configurations) are generated by randomly sampling the well thermalized trajectory. These methods can be included into the existing x-ray absorption calculation without any modification to the codes.

Furthermore, the N-temperature model for describing the evolution of electron temperature is a complementary tool for studying the dynamical response in XAS. The two-temperature model for metals is well studied by Allen [60] and Lin et al. [87]. The electron-phonon coupling factor and electron heat capacity can be calculated from the electron density of states. For spin systems, an additional degree of freedom is introduced to the system. Calculating the couplings for the spin with the electron and lattice subsystems is non-trivial.

Chapter 4

CALCULATIONS OF FINITE TEMPERATURE X-RAY SPECTRA

In this chapter, we present our results calculated using our implementation of finite temperature XAS code FEFF10. We investigate some well-studied simple metal systems to explore the range of applicability of FEFF10. We also apply the code to study the response of a metal-insulator heterostructure under a ultrafast laser heating.

4.1 Warm Dense Aluminum

Aluminum (Al) is a prototypical system for testing electronic structure calculation. The electronic density of states (DOS) for Al is similar to free electron model with a square root like dispersion. We compute the chemical potential for aluminum up to $T_e = 10$ eV in Fig 4.1 using temperature independent exchange-correlation potential von Barth Hedin (v_{xc}^{VBH}) [55] and temperature dependent exchange-correlation KSDT (v_{xc}^{KSDT}) [32]. The temperature correction to the chemical potential is negligible for $T < 1$ eV. In addition, our v_{xc}^{VBH} chemical potential agrees with the GGA T=0K DFT calculation [87] up to $T = 4$ eV. The chemical potential exhibits free electron like behavior up to 10 eV.

In Fig. 4.2, we compare our calculated density of states at 10 eV to the non-relativistic KKR code of Starrett [48] and the average atom code Tartarus [35]. We see a good agreement with our implementation and with the KKR code. The KKR code is similar to FEFF with the use of the spherical muffin-tin potential and real-space multiple scattering approach. However, it solves the non-relativistic Schrödinger equation. In our calculation, we include states up to angular momentum $l_{max} = 8$. The s, p and d states ($l < 3$) contributes to the DOS below 40 eV. The structure of the DOS in the KKR code and our code is due to the

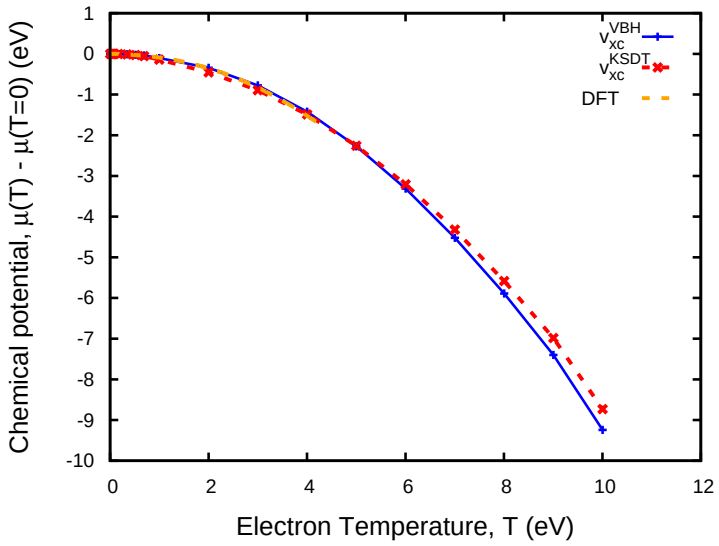

Figure 4.1: Chemical potential for aluminum, $\mu(T)-\mu(T=0)$ versus electron temperature,T using von Barth Hedin exchange-correlation potential (blue) [55] and KSDT exchange-correlation potential (red) [32]. The T=0K DFT calculation (orange) by Lin et al. [87] is shown up to $T = 4$ eV.

multiple-scattering effects which is absent in the average atom model. The bound state in the average atom model can only exists as Dirac delta functions which is seen near $E = 0$ eV. On the other hand, the sharp peak below $E = 0$ eV in our calculation is due to the discontinuity of the derivatives near the chemical potential.

Next, we investigate the temperature dependence of the K-edge x-ray absorption at solid density up to warm dense Al. We compute the K-edge absorption for electron temperature $T_e = 0.025$, 0.5, 1.4 and 3.0 eV in Fig 4.3. The behavior of the K-edge is similar to the broadening of the Fermi-Dirac distribution due to the simple free electron like density of states of Al. The onset of the pre-edge is due to the increasing contribution of states below the Fermi level. In addition, we compare our multiple-scattering approach within the correlated Debye model ($T_{Debye} = 430$ K) to two other models.[25] The first model is based on the DFT coupled with quantum molecular dynamics (QMD). The absorption cross section

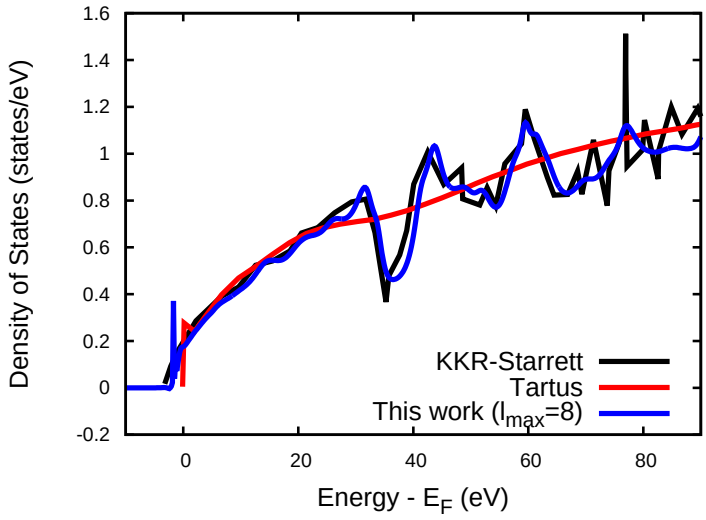

Figure 4.2: Density of states for aluminum at electronic temperature $T_e = 10$ eV: (blue) our calculation including states up to $l_{max} = 8$, (black) the non-relativistic KKR calculation by Starrett [48] and (red) the average atom model, Tartarus [48, 35].

.

calculated using the DFT orbitals is averaged over QMD runs. The second model is the hyper-netted-chain neutral pseudo atom (HNC-NPA) model described in Ref [90, 67]. This model assumes that the ions are surrounded by a spherical electron cloud forming a locally neutral sphere. This approximation has been proven to be effective at computing properties of hot dense plasma when QMD is prohibitively expensive. Mančić et al. investigated the Al K-edge under isochoric heating condition ($T_e = T_L$) at solid density.[25] The absorption measurements are taken at equilibrium temperatures $T_e = T_L = 0.025$, 0.09, 0.27, 1.40 and 1.76 eV as shown in Fig 4.4. They found that the QMD-DFT approach agrees better with the experiment at low temperature ($T < 0.4$ eV) while HNC-NPA is a better model for higher temperatures. Our model agrees qualitatively with the experiment up to $T = 0.27$ eV with the correlated Debye model. At low temperatures, our model provides a good approximation to the more computationally demanding QMD-DFT method. However, the correlated De-

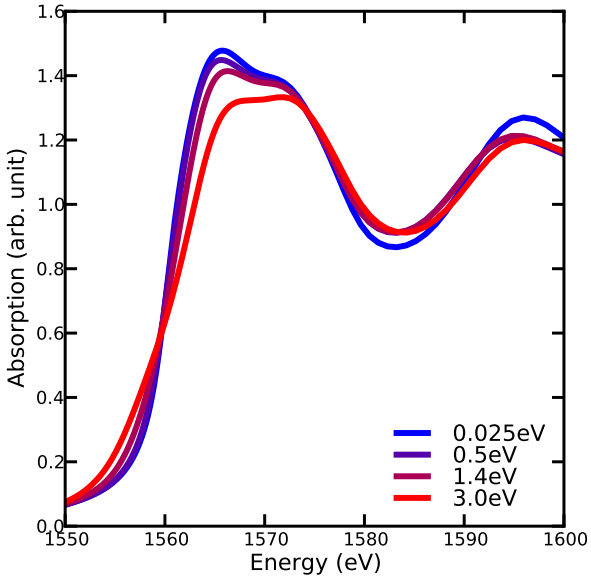

Figure 4.3: Electron temperature dependence of K-edge absorption for Al at $T_e = 0.025$, 0.5, 1.4 and 3.0 eV.

bye model breaks down at high temperature when the anharmonicity contribution becomes large which is expected at temperatures well above T_{Debye}. Fine structures are completely suppressed in the correlated Debye model at $T = 0.27$ eV which is about $8T_{Debye}$ while the other two models retains some structure.

4.2 Warm Dense Copper

Copper is a transition metal. It has different excited-state property compared to simple metals like aluminum due to the highly localized d-band below the Fermi level. Hence, at elevated temperatures, the changes in XAS will be different from other simple metals. Several works [5, 27, 26, 36] have been conducted to study these non-trivial changes to the $L_{3,2}$-edge in warm dense matter using a more accurate but a more computationally expensive AIMD simulation. Here we investigate the changes in XANES for the $L_{3,2}$ within the correlated Debye model approximation to the lattice dynamics. Fig 4.5 shows the simulated XANES

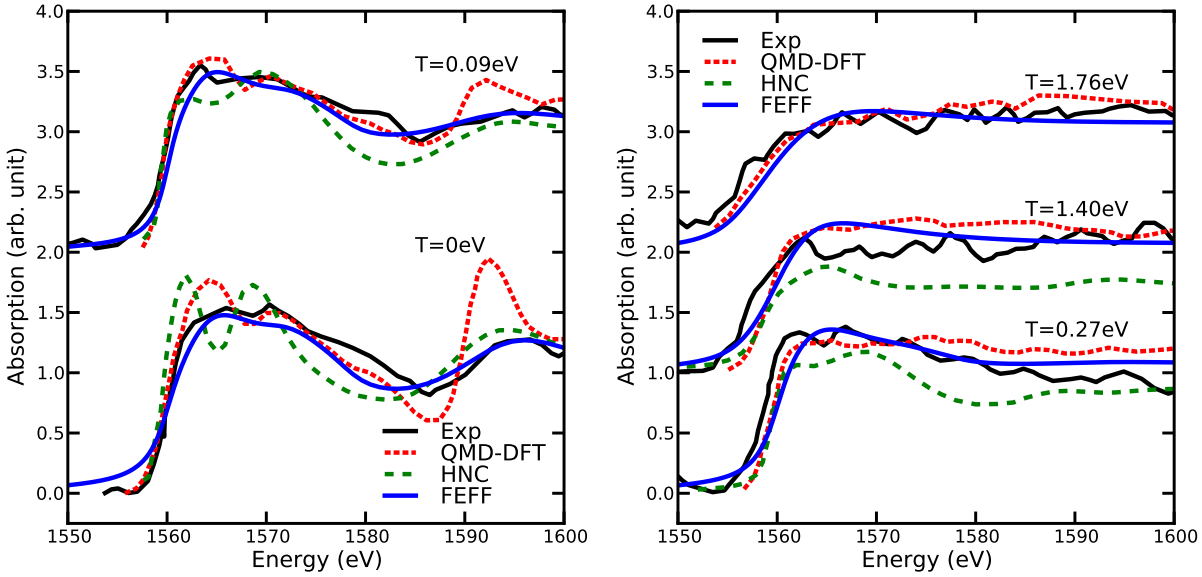

Figure 4.4: K-edge absorption for equilibrium Al ($T_e = T_L$) at solid density. (Left) Experimental absorption spectra at $T = 0$ and 0.09 eV.[25] FEFF simulation are done at the same temperature as the experiment. From bottom to top, QMD-DFT are simulated at $T = 0$ and 0.07 eV while HNC-NPA are simulated at $T = 0$ and 0.1 eV. (Right) Experimental absorption spectra at $T = 0.27$, 1.4 and 1.76 eV. From bottom to top, QMD-DFT are simulated at $T = 0.43$, 0.86 and 0.07 eV while HNC-NPA are simulated at $T = 0.5$ and 1.0 eV. FEFF simulation are done at $T = 0.27$, 1.4 and 3.0 eV.

spectra at solid density for various temperatures. Our calculation is broadened with a Gaussian to match the DFT spectra by Jourdain et al. [91]. The increase in electron temperature induces the rise of the pre-edge structure consistent with the results reported in Ref [5, 27, 26, 36]. The pre-edge structure in the XANES can be attributed to the increasing contribution from the d-states as the Fermi-Dirac distribution broadens. Conversely, states right above the Fermi level have a smaller contribution leading to a smaller peak at the edge. The changes in XAS due to electronic temperature are mainly localized near the edge whereas the lattice response broadens the fine structure. To extract the edge shift and pre-edge area

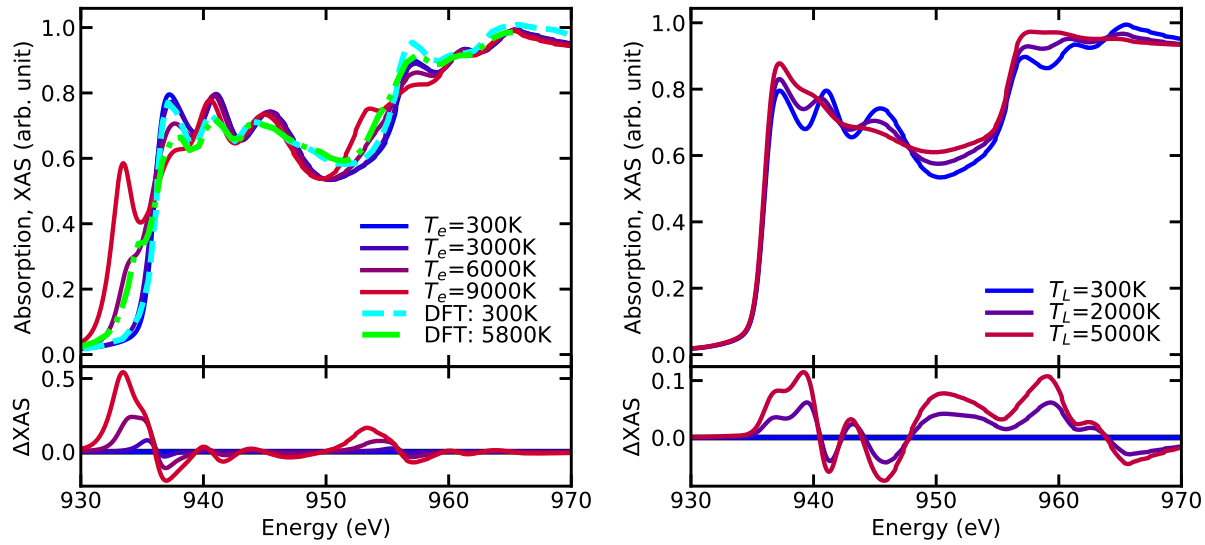

Figure 4.5: Copper L_3-edge at solid density for (Left) electron temperature $T_e = 300$ K up to 9000 K at lattice temperature $T_L = 300$ K and (Right) for lattice temperature $T_L = 300$ K up to 5000 K at electron temperature $T_e = 300$ K. The DFT calculation by Jourdain et al. [91] is shown for $T_e = 300$ K (light blue) and 5800 K (green). The lower panels show the change in absorption with respect to the ambient condition $T_e = T_L = 300$ K.

under the curve, the edge boundary is defined to be the first local maximum of the first derivative in the reference XANES spectrum. The electron temperature dependence of the edge shift and pre-edge area are shown in Fig 4.6. The pre-edge area is linearly correlated to the electron temperature up 6000 K before the pre-edge structure amplitude is significant compared to the absorption above the edge. On the other hand, the pre-edge area is a slowly varying function of the electron temperature even at elevated temperature. Our calculation shows a non-linear relation below 6000 K with a transition to a linear relation at high temperature similar to the result obtained by Jourdain et al. [91]. Therefore, the pre-edge area is a better proxy to the electron temperature compared to the edge shift.

Next, we compare our finite-temperature calculation to the time-resolved XANES experiment of warm dense copper by Cho et al. [5]. The system under investigation is a 70 nm

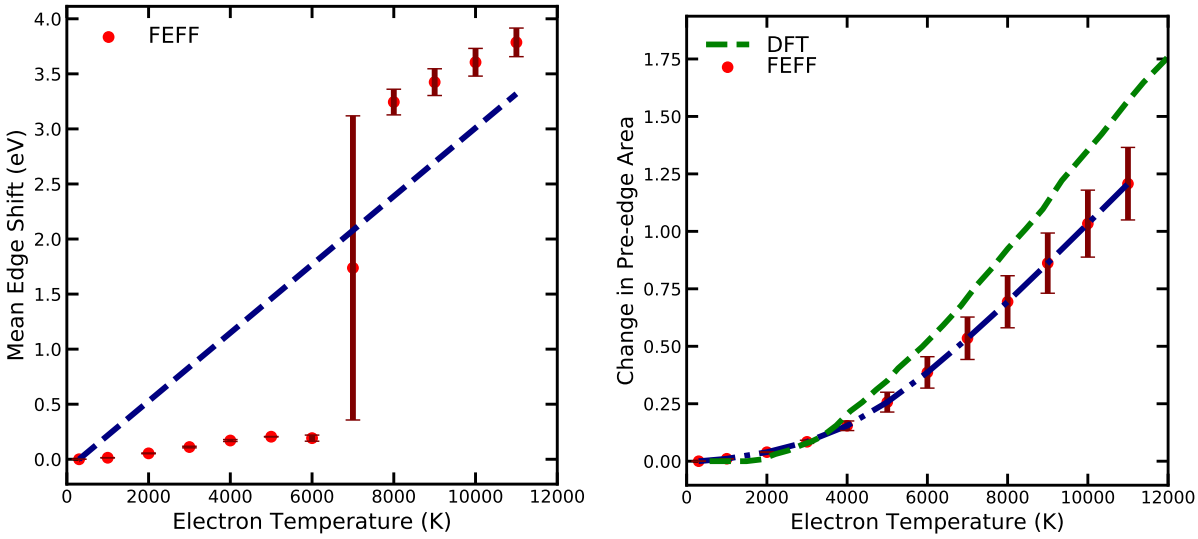

Figure 4.6: (Left) Edge shift in the L_3-edge as a function of electron temperature. The blue curve is a linear fit of the FEFF calculation (red). The error bar represents the standard deviation of the edge shift over different lattice temperature up to $T_L = 10000$ K. (Right) The change in pre-edge area as a function of electron temperature. The DFT calculation (green) by Jourdain et al. [91] is computed using ABINIT at lattice temperature $T_L = 300$ K.

copper foil heated optically by a 400 nm laser at a fluence of 0.33 J/cm^2. The electrons are optically excited leading to a huge pre-edge peak below the L_3-edge. To model the temperature evolution, the 2TM model introduced in section 3.2.1 is used. We chose the same parameters as Cho et al. with the ab initio electron heat capacity and electron-phonon coupling factor from Lin et al.[87] The temperature evolution is shown in Fig. 3.1. The lattice temperature raises quickly above the melting temperature ~1358 K under 1 ps due to the strong electron-phonon coupling in copper.

In our simulation, we compute the XAS from 20 atomic configurations from QMD simulation using the VASP package [92, 93] with the generalized gradient approximation [94]. We use the PAW potentials with an energy-cutoff of 590 eV. The 2×2×2 supercell system is

propagated with a time step of 1 fs to reach equilibration and the sampling of configurations is performed by randomly sampling from a 2 ps long trajectory with a time step of 1 fs. We compare our simulation at the temperatures T_e = 300 K, 10200 K and 6000 K for the time-delays $t < 0$ ps, t= 2 ps and t= 9 ps respectively with the DFT calculation by Cho et al. [5] in Fig 4.7. Our calculation overestimates the Fermi level for T_e = 10200 K (t=2 ps) by a few eV leading to the shift in the XANES.

4.3 Non-equilibrium Fe/MgO Heterostructure

In this section, we consider a metal-insulator system made up of eight 2 nm layers of iron (Fe) and magnesium oxide (MgO) stacked in alternating order as shown in Fig. 4.8. The heterostructure is grown on a 200 nm thick Si_3N_4 membrane with a 100 nm thick Cu as heat sink. Rothenbach et al. [8] investigated the energy transport across the Fe-MgO interface by measuring the Fe L3-edge and O K-edge. The Fe layers are optically excited by a 264 nm laser with an incident fluence of 20 mJ/cm^2 and a pulse duration of 50 fs. A maximum change in absorption is reported at 240 fs for Fe and at 870 fs for O after the initial laser heating.

We compute the XAS for Fe/MgO using a $5 \times 5 \times 2$ supercell with 573 atoms based on the 24 atom optimized primitive cell structure by Markus Gruner and Rossitza Pentcheva [95] as shown in Fig. 4.9. The center layers of iron and oxygen are labeled L1. The intermediate layers are labeled L2 and L3. The interface layers are labeled L4. We define 13 unique potentials for type of atom in each layer including the potential for the absorbing atom. A spin occupation of 3.5, 3.5, 3, 2.5 for the iron layers L1, L2, L3, L4 respectively is chosen such that the density of states matches as close as possible to the density of states computed in Ref [8] supplemental material. In contrast, the spin occupation for bulk iron is 4.

Fig 4.10 shows the ferromagnetic ground state density of states for L1 and L4. A complete DOS for each layer can be found in the Appendix E. The Fe and O spin down density of states in the interface layer L4 has a localized empty states right above the Fermi level. This is due to the hybridization between the Fe and O at the interface. However, the interface

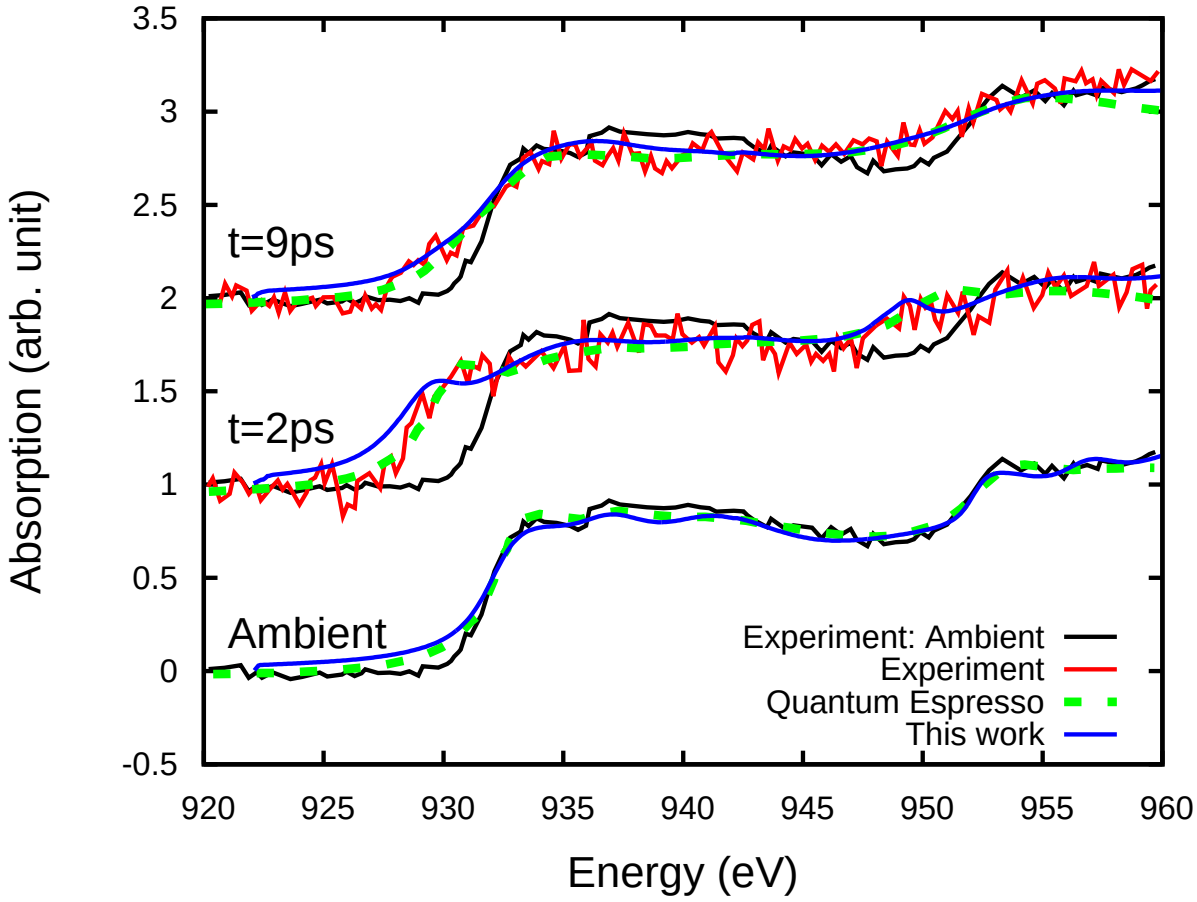

Figure 4.7: Time-resolved XANES for 70 nm copper at different times t =2 ps and 9 ps. The experimental measurement (red) is averaged over 150 snapshots. The ambient condition measurement is averaged over 70 ps. Our calculation (blue) for different times are computed at T_e = 10200 K adn 6000 K. The DFT result by Cho et al. [5] (green) is calculated using Quantum Espresso code at the same temperatures.

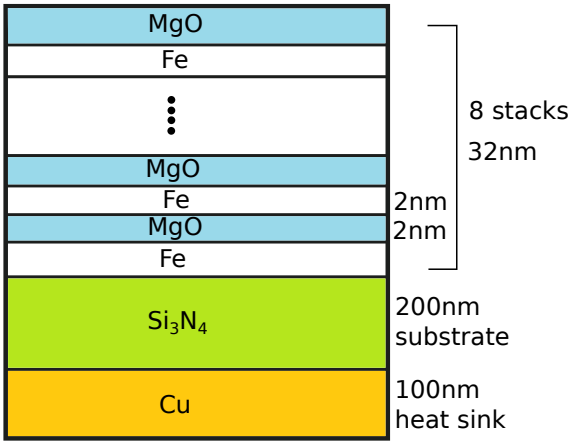

Figure 4.8: $[Fe/MgO]_8$ heterostructure made up of eight 2 nm Fe and 2 nm MgO grown on a Si_3N_4 substrate with a Cu heat sink.

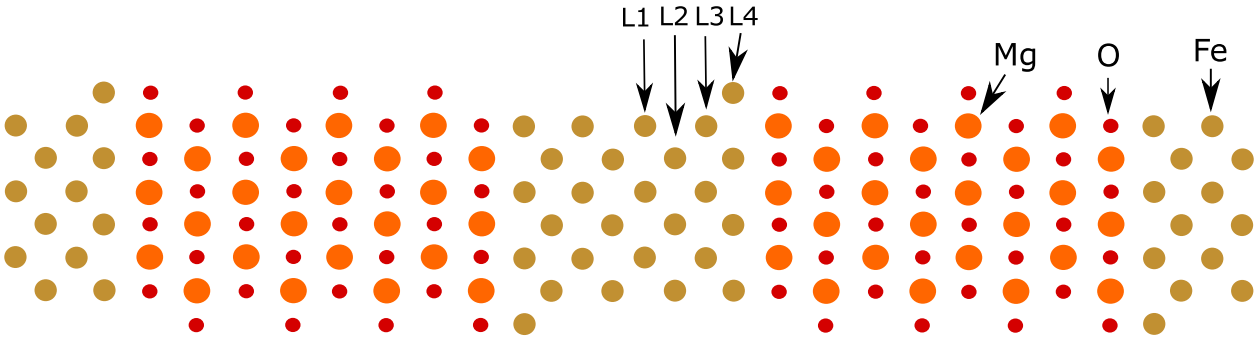

Figure 4.9: The cross section of the structure used in our calculation provided by Markus Gruner and Rossitza Pentcheva. Atoms in gold are Fe, in red are O and in orange are Mg. The inner layer is labeled L1. The intermediate layers are labeled L2 and L3. The interfaces are labeled L4.

state in the O is placed at the wrong location due to the incorrect placement of the Fermi level right above the valence states in the MgO. The spherical muffin-tin approximation is not able to accurately determine the charge transfer in oxides.The computed layer resolved x-ray absorption for Fe L_3-edge and O K-edge are shown in Fig 4.11. The L_3-edge of metal is characterized by a huge white line. The absorption edge of Fe in L4 is red-shifted compared to the bulk layer as the edge state is closer to the Fermi level. On the other hand, the presence of the edge state in MgO induces a pre-edge structure at L4.

4.3.1 Fe L_3*-edge*

To understand the magnetization dynamics of Fe, we employ the three temperature model (3TM) as in Ref [88].

$$C_e \frac{dT_e}{dt} = -G_{el}(T_e - T_l) + P(t) \quad (4.1)$$

$$C_l \frac{dT_l}{dt} = G_{el}(T_e - T_l) \quad (4.2)$$

$$\frac{dT_s}{dt} = \tau_M^{-1}(T_e - T_s) \quad (4.3)$$

where C_e and C_l are the electronic specific heat capacity and lattice specific heat capacity. P(t) is the laser source term. G_{el} is the electron-phonon coupling constant. Since the atomic moment of iron is coupled to the electronic temperature, the spin temperature in this model describes the overall macroscopic magnetization of the system. A demagnetization time constant τ_M is used to model the dynamic. C_e and G_{el} are modeled with the zero-temperature DFT calculation in Ref [87]. The parameter $C_l = 2.2\times10^6$ $\mathrm{Jm^{-3}K^{-1}}$ [88] is taken to be temperature independent and $\tau_M = 0.34$ fs to be the same as the demagnetization time constant of cobalt [88]. The laser source is modeled with the experiment fluence of 20 $\mathrm{mJ/cm^2}$ with a pulse width of 50 fs. We employ Beer-Lambert law for the laser attenuation. We also account for the temporal resolution of the detector (150 fs) by convolving the electronic temperature with a Gaussian. We ignore the heat exchange between the MgO by assuming the heat exchange between Fe and MgO is at a longer time scale. The result of the simulation

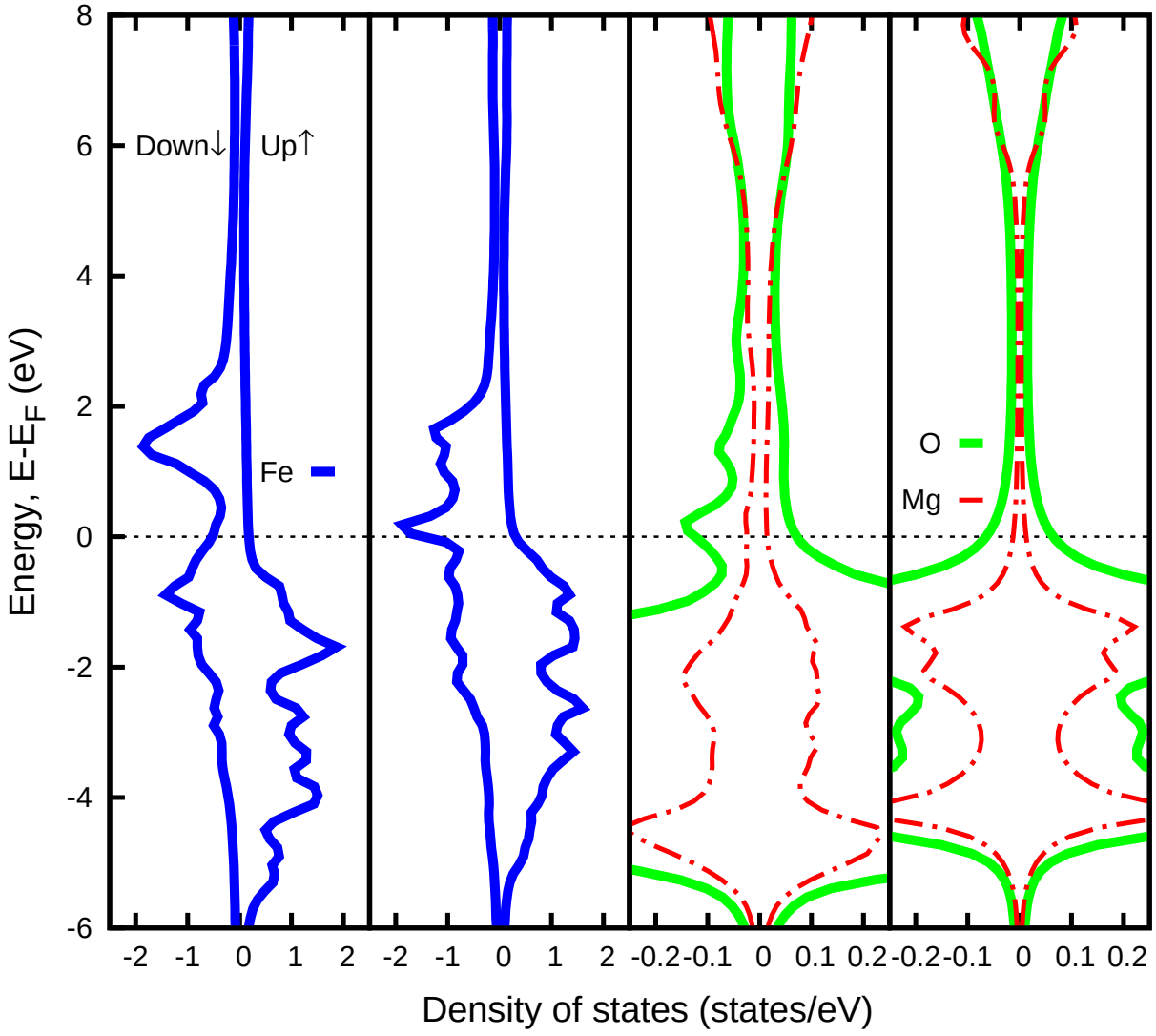

Figure 4.10: Layer resolved density of states (DOS) for Fe/MgO at $T = 0$ K. From the left, the first two figures are the total DOS of iron for the center layer (L1) and the interface layer (L4). The last two figures are the total DOS of MgO for layers L4 and L1.

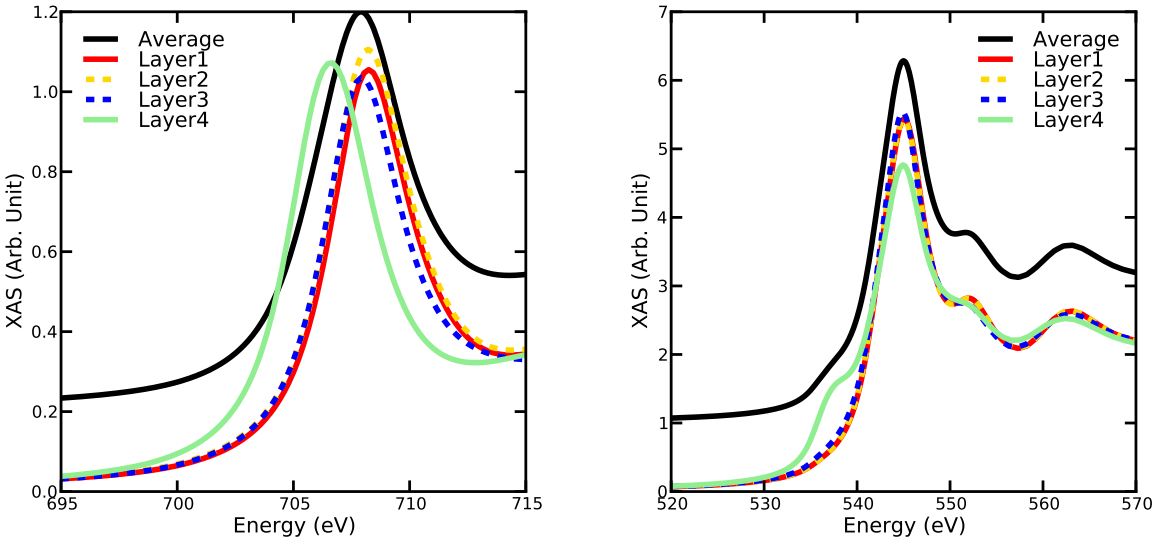

Figure 4.11: Layer resolved x-ray absorption of Fe/MgO heterostructure for: (left) Fe L_3-edge and (right) O K-edge. Layer 1 corresponds to the middle layer and layer 4 correspond to the interface layer. The average absorption spectra (black) are slightly offset.

is shown in Fig 4.12. T_e reaches the maximum in ∼100 fs while T_s reaches a temperature well above the Cure temperature of 1043 K in ∼200 fs. This simplified model does not account for heat transfer between the iron and magnesium oxide. The temperatures in this simulation are likely to be overestimated but it serves as an initial guess to the electron temperature in fitting the XAS. In our first analysis, we investigate the effect of the change in atomic magnetization. We compare the L3-edge x-ray near-edge absorption (XANES) for the paramagnet Fe/MgO and ferromagnet Fe/MgO at an electronic temperature T_e=300K and 1600K. The layer-averaged absorptions are shown in the Fig 4.13. The calculated energy shift (about 1eV) between the two absorption spectra is much larger than the measured shift at time-delay of 240 fs. This is because of the large exchange splitting (∼ 2eV) in the density of state. The huge spin down occupation at 1.5 eV in Fig 4.14 is shifted towards the Fermi level when the atomic magnetization decreases to zero. Therefore, our calculation based on

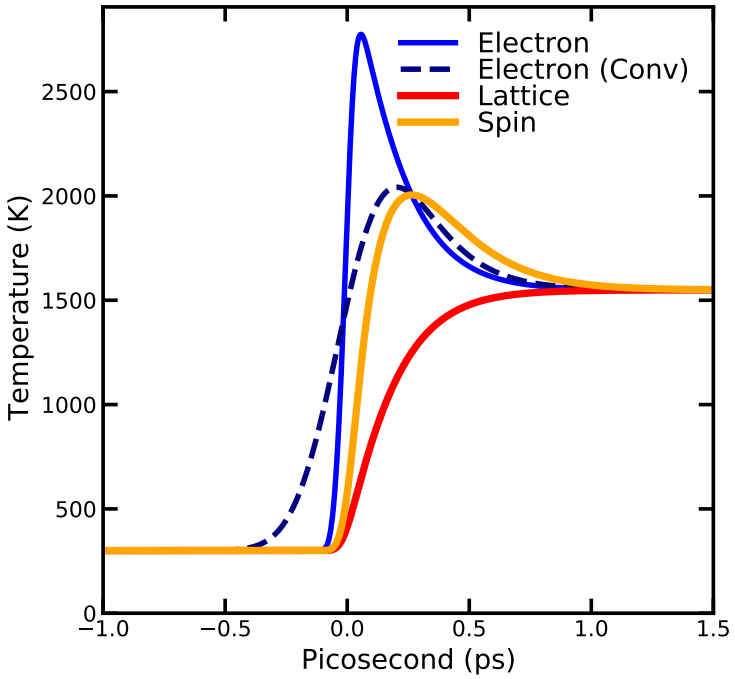

Figure 4.12: Dynamics of 16 nm Fe layer induced by a laser pulse with fluence of 20 mJ/cm^2, width of 50 fs and wavelength of 263 nm. The electronic temperature with detector temporal resolution of 150 fs is shown in dashed.

the collapse of exchange splitting is not able to explain the demagnetization of Fe/MgO.

Next, we present our results in Fig 4.15 based on the assumption that the spin rotation is the major contribution. The top plot shows the layered-resolved Fe L3-edge absorption at $T_e = 300$ K. The middle plot shows a comparison between the experimental measurements at a time-delay of 240 fs with our layer-averaged calculation. The relaxation of the non-equilibrium electrons is accompanied by the creation of magnons which reduces the net magnetization of the hetero-structure. The resulting differences in the absorption is shown in the bottom plot of Fig 4.15 is mainly due to the Fermi-Dirac broadening and the shift in chemical potential. To include the temperature effects on the atomic moment, we reduces the spin occupation according to the atomic magnetization curve computed by Chimata et al.

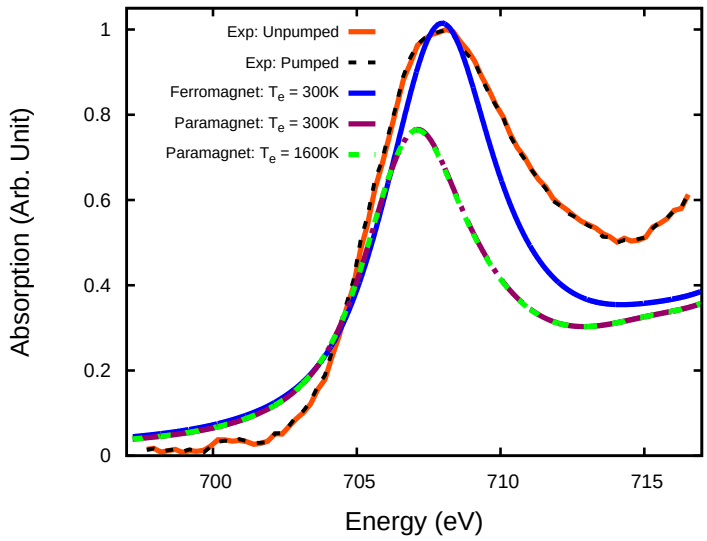

Figure 4.13: Fe L3-edge x-ray absorption for paramagnetic state and ferromagnetic state of Fe/MgO. In the solid blue line is the calculated absorption for ambient condition (ferromagnetic state). In dashed lines are the calculated absorption (T_e = 300 K, 1600 K) for the paramagnetic excited system. In black and red are the unpumped and pumped experimental measurements at 240 fs time-delay.

[88]. Here we assume that the atomic moment is characterized by the electronic temperature T_e. At T_e = 2000 K, the reduction in atomic moment is less than 2%. The resulting differences in the absorption are shown in dashed lines.

4.3.2 O K-edge

For the oxygen K-edge, the experimental measurement of the absorption signals have substantial background in the pre-edge region. This is due to a technical difficulty with the experimental setup that prevents measurement of the reference incident intensity. [8] However, the background is canceled out when taking the difference between the pumped and unpumped signal. Appendix E details the post-processing background subtraction for ex-

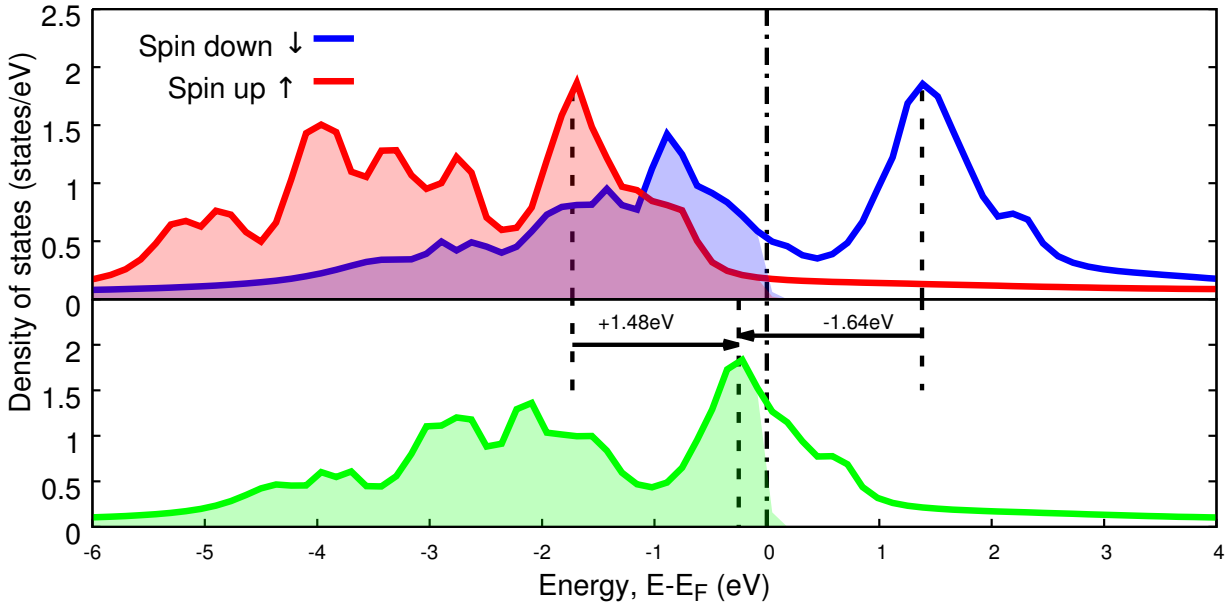

Figure 4.14: (Top) Spin-polarized density of state for L4 layer of Fe. The shaded area represents the occupied portion of the density at T= 300 K. (Bottom) Density of state for L4 layer of Fe in the paramagnetic state. The density is scaled by 1/2 to match the spin-polarized density in the plot above.

perimental absorption.

We model the thermal disorder by a correlated Debye model with a Debye temperature of T_{Debye} = 470 K. Since MgO is an insulator and for temperatures below 1 eV , the Fermi-Dirac broadening effect is negligible. Fig 4.16 shows the results for fixed T_e = 300 K at various lattice temperatures T_l. The top plot shows a comparison between the experimental measurements at a time-delay of 870 fs with our layer-averaged calculation. The pre-edge structure in the experiment is obscured by the huge background. The bottom plot shows the differences in absorption between the absorption before and after pumping. In this short time frame, the lattice excitation is highly non-thermal [8] with certain optical vibrations modes being activated. Our theory approximates the phonons contribution to the XANES through

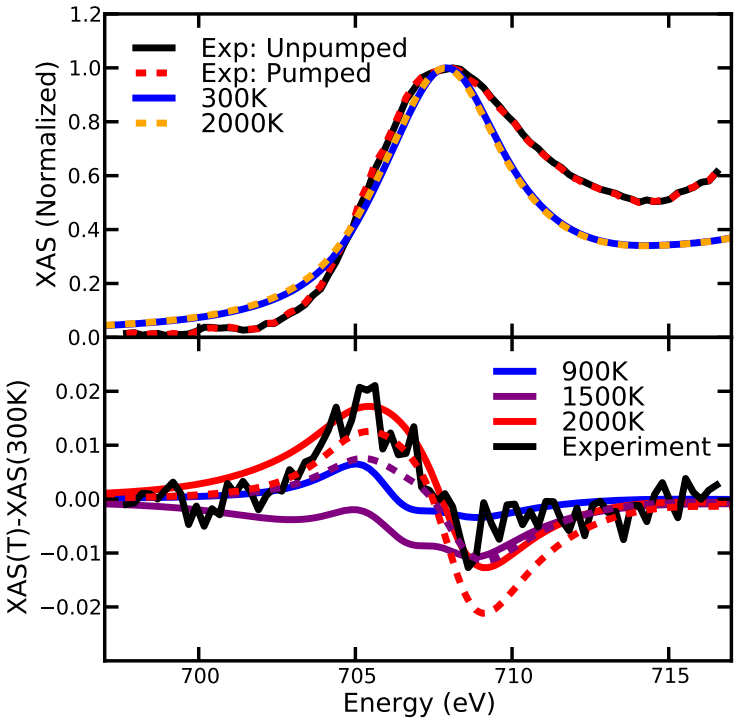

Figure 4.15: (Top) Comparison between layer-averaged XANES and experimental measurement at 240 fs time-delay. (Bottom) Change in absorption between elevated temperature absorption and the room temperature absorption. In black is the experimental differences. In the solid lines are the calculated differences due to change in electronic temperature only. In dashed lines are the calculated differences (T_e = 1500, 2000 K) due to the change in electronic temperature and atomic spin based the magnetization curve in Ref [88].

the single scattering Debye-Waller factor. Further investigation is required to separate the contribution from the hot phonons and cold phonons.

While the phonon dynamics at 870 fs is dominated by highly thermal incoherent excitations, the correlated Debye model is a better description for the equilibrium phonons at 90 ps.[96] Fig 4.17 shows a comparison between our calculation and the experiment at 90 ps for the O K-edge. In this experiment, the pre-edge structure of is visible and the change in absorption is more localized compared to our calculation near the edge. This can be attributed

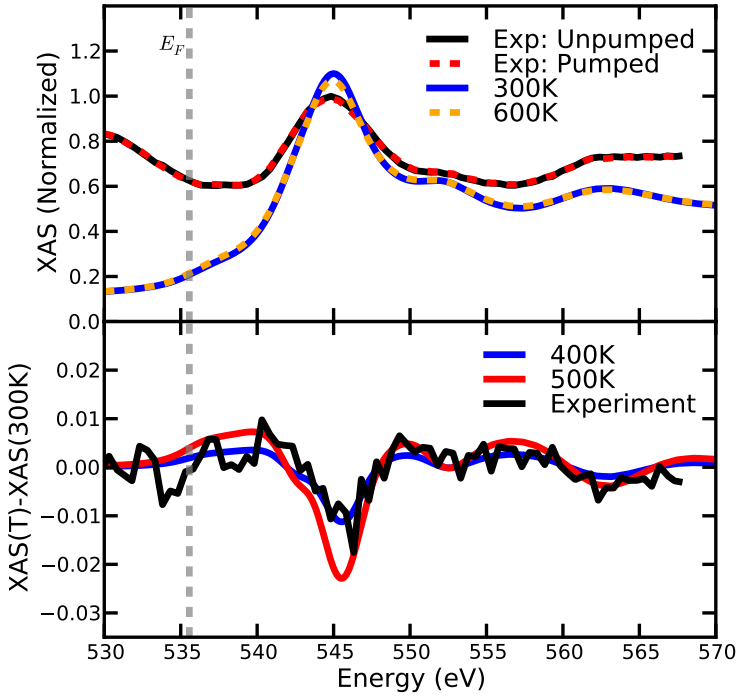

Figure 4.16: (Top) Comparison between layer-averaged XANES (with 0.1 offset) and experimental measurement at 87 fs time-delay. Substantial background is present in the pre-edge region but it does not affect the spectral difference. (Bottom) Change in absorption between elevated temperature absorption and the room temperature absorption. In black is the experimental differences. In the solid lines are the differences due to Debye-Waller factor only.

to the incorrect placement of the localized state at the oxygen interface layer. Above the edge, our calculation is able to capture the changes in the fine structure. Since the phonons are thermally coherent in this case, the lattice temperature of correlated Debye model is a well defined quantity and our estimated temperature of 400 K agrees with the temperature estimate 430±10 K from the diffraction measurement of Rothenbach et al. [8].

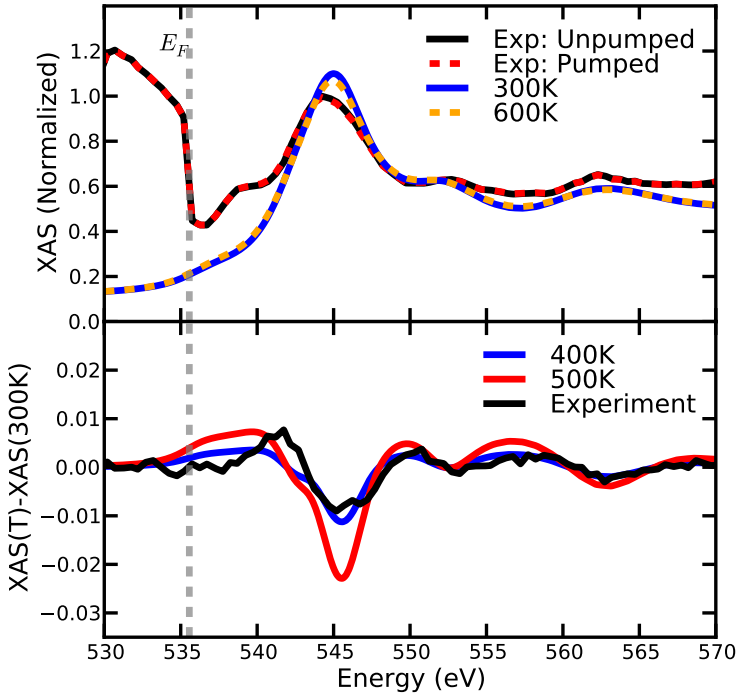

Figure 4.17: (Top) Comparison between layer-averaged XANES (with 0.1 offset) and experimental measurement at 90 ps time-delay. Substantial background is present in the pre-edge region but it does not affect the spectral difference. (Bottom) Change in absorption between elevated temperature absorption and the room temperature absorption. In black is the experimental differences. In the solid lines are the differences due to Debye-Waller factor only.

4.4 Summary

In this chapter, we have demonstrated FEFF10's capability in calculating the finite temperature XAS for different metal systems up to warm dense regime. We achieve good agreement with experimental results and other DFT codes. AIMD can be combined with FEFF10 to simulate the response to x-ray for non-periodic systems up to warm dense regime. In particular, the XANES for Al and Cu for various temperatures at solid density are presented in this

chapter. The simple metals like Al have different temperature response near the absorption edge compared to $3d$ transition metals at elevated temperatures. The pre-edge absorption in L_3-edge of Cu is determined by the localized states below the Fermi level. Moreover, the pre-edge area and edge shift are correlated the electron temperature. These correlations can be used as a quick diagnostic for the electron temperature. Further investigation is required to quantify the quality of estimations at various extreme conditions.

In addition, the analysis of the XANES for Fe/MgO heterostructure results in an understanding of the physical processes that led to the observed spectral changes. The Fe layers in the heterostructure have similar demagnetization response to the Fe film [44, 97]. They do not exhibits the signature of exchange splitting collapsing. Furthermore, the changes in the O K-edge in the MgO layers are dominated by the lattice response up to the picosecond regime.

Chapter 5

FINITE-TEMPERATURE SELF-ENERGY CORRECTION

[Originally published as: Tun S. Tan, J. J. Kas, and J. J. Rehr Phys. Rev. B 98, 115125 (2018)]

In this chapter, we present the finite temperature generalization of the quasiparticle electron self-energy Σ within the COHSEX approximation. This work is tangent to the development of finite temperature XANES since there are considerable interest in properties of matter at finite-temperatures (FT) and extreme conditions.[98, 99, 100] Such properties are often treated using the FT generalization of DFT, with an appropriate FT exchange-correlation functional.[31, 101, 102, 103] However, many properties, such as band-gaps and optical spectra require many-body corrections for an accurate treatment. Consequently a more detailed treatment of exchange and correlation effects beyond DFT are often needed.[104]

Formally, such effects can be described in terms of the one-electron Green's function G, which satisfies a Dyson equation $G = G_0 + G_0 \Sigma G$, which is also applicable at finite T for either the Matsubara or retarded Green's functions. Here G_0 is the one-electron Green's function, and Σ the one-electron self-energy which accounts for many body exchange and correlation effects due to electron-electron interactions v. In principle, Σ can be calculated using many-body perturbation theory with an expansion in powers of v. However, this procedure converges poorly, and a better strategy is to expand in powers of the screened Coulomb interaction $W(q,\omega) = \epsilon^{-1}(q,\omega) v_q$ in momentum- and frequency-space, where $\epsilon(q,\omega)$ is the dielectric function and $v_q = 4\pi/q^2$ the bare Coulomb interaction. While there have been many works focusing on higher order (vertex) corrections to the self-energy,[105, 106] here we keep only the leading term first order in W, i.e., $\Sigma = iGW$, yielding the GW approximation of Hedin.[107, 108]

The GW approximation has been highly successful e.g., for quasiparticle properties such

as corrections to DFT calculations of band-gaps, and has also been extended to finite temperatures.[109, 110] On the other hand, the GW self-energy $\Sigma(k,\omega)$ is state and frequency dependent, and its calculation is computationally demanding. In an attempt to develop a more efficient approximation, the static COHSEX has been introduced, in which the screened Coulomb interaction $W(q,\omega)$ is replaced by its static limit $W(q,0)$, and the self-energy Σ is split into statically screened exchange (SEX) and Coulomb-hole (COH) terms.[108] Although the separation into exchange and correlation parts is arbitrary, depending on the treatment of exchange, the explicit separation of the COH and SEX contributions in the COHSEX approximation is physically motivated,[108, 111] and serves to elucidate the nature of exchange and correlation effects in the theory.

Since its inception, the $T = 0$ COHSEX approximation has been well studied.[108, 112] however, its behavior at finite-temperature has heretofore been unexplored. The main goal of this chapter is therefore to develop the FT generalization of the COHSEX approximation, and to assess it's accuracy. Our approach is based on an extension of the FT GW approximation to the self-energy.[113] We present a systematic analysis similar to that for $T = 0$, comparing the static COH and SEX approximations with the fully dynamic GW quasiparticle self energy. We also present a brief analysis of the physical basis of these results. As in other investigations of the GW approximation,[109, 106, 103] we limit our explicit calculations here to the homogeneous electron gas (HEG). However, the approach can be applied more generally as an approximation to the GW self-energy.

The remainder of the chapter is organized as follows: in the next section we review the $T = 0$ case and present the FT generalizations of the GW and static COHSEX approximations. Subsequent sections discuss the static and fully dynamic results, followed by an analysis and a summary and conclusions. Throughout this chapter we use Hartree atomic units $e = \hbar = m = 1$, with energies in Hartrees and distances in Bohr, unless otherwise noted.

5.1 COHSEX Approximation

5.1.1 Zero-temperature

We begin with a summary of results for the GW self energy and the COHSEX approximation at $T = 0$. All the quantities discussed in this limit are time-ordered, as in standard zero-temperature many-body perturbation theory. Formally, the GW approximation to the quasiparticle self-energy in momentum-k and frequency-ω space at $T = 0$ is the GW self-energy given by[107, 108]

$$\Sigma^T(k,\omega) = \int \frac{d^3q\ d\omega'}{(2\pi)^4}\, G_0^T(\mathbf{k}-\mathbf{q},\omega-\omega')W^T(q,\omega')e^{-i\omega'\delta^+}, \tag{5.1}$$

where G_0^T is the non-interacting, time-ordered one-particle Green's function and W^T the time-ordered, dynamically screened Coulomb interaction. For a given dielectric function $\epsilon(q,\omega)$, the screened interaction W^T can be expressed in terms of its spectral representation

$$W^T(q,\omega) = v_q + W_p^T(q,\omega), \tag{5.2}$$

$$W_p^T(q,\omega) = \int_{-\infty}^{\infty} d\omega' \frac{D(q,\omega')}{\omega-\omega'+i\delta\,\mathrm{sgn}(\omega')}, \tag{5.3}$$

where $D(q,\omega) = (1/\pi)|\mathrm{Im}\, W^T(q,\omega)|\,\mathrm{sgn}(\omega)$ is the anti-symmetric (in frequency) bosonic excitation spectrum and $W_p^T(q,\omega)$ the polarization part of W^T. Thus the poles of $W^T(q,\omega)$ in the ω-plane correspond to the peaks in the loss function $(1/\pi)\,|\mathrm{Im}\,\epsilon^{-1}(q,\omega)|$. Formally the GW self-energy Σ can be partitioned into fully dynamic screened exchange (SEX) and Coulomb-hole (COH) terms, which are defined from the poles of G_0^T and those of W^T respectively.[107] At zero temperature this yields the exact separation $\Sigma^T(k,\omega) = \Sigma^{SEX,T}(k,\omega)+\Sigma^{COH,T}(k,\omega)$ where

$$\Sigma^{SEX,T}(k,\omega) = -\int \frac{d^3q}{(2\pi)^3} f(\varepsilon_{\mathbf{k}-\mathbf{q}})W^T(q,\omega-\varepsilon_{\mathbf{k}-\mathbf{q}}), \tag{5.4}$$

$$\Sigma^{COH,T}(k,\omega) = \int \frac{d^3q}{(2\pi)^3}\int_0^{\infty} d\omega' \frac{D(q,\omega')}{\omega-\varepsilon_{\mathbf{k}-\mathbf{q}}-\omega'+i\delta}. \tag{5.5}$$

The COHSEX approximation to the quasiparticle self-energy, is then defined as the statically screened approximation to the on-shell GW self-energy $\Sigma(k,E_k)$, where the quasiparticle energy satisfies $E_k = \varepsilon_k + \Sigma(k,E_k)$. The bosonic spectral function $D(q,\omega)$ becomes

small at large q; if this decay is sufficiently rapid, then since $E_k \approx k^2/2$ one can to a good approximation replace $\omega - \varepsilon_{\mathbf{k}-\mathbf{q}} \approx 0$ in W in Eq. (5.4) and (5.5).[108] Then, using the spectral representation of W, the static COH and SEX approximations, which are independent of frequency ω, can be denoted with a subscript k and given by

$$\Sigma_k^{SEX} = -\int \frac{d^3q}{(2\pi)^3} f(\varepsilon_{\mathbf{k}-\mathbf{q}}) W^T(q,0), \tag{5.6}$$

$$\Sigma_k^{COH} = \frac{1}{2}\int \frac{d^3q}{(2\pi)^3} W_p^T(q,0), \tag{5.7}$$

where $f(\varepsilon) = \theta(\mu - \varepsilon)$ is the zero-temperature Fermi factor. The factor 1/2 is due to the anti-symmetry of $D(\omega)$ about $\omega = 0$, and has been attributed to the adiabatic turn on of the screened interaction.[108] Their sum is referred to as the static COHSEX self-energy

$$\Sigma_k^{COHSEX,T} \equiv \Sigma_k^{COH,T} + \Sigma_k^{SEX,T}. \tag{5.8}$$

This approximation is often used as an efficient method for obtaining quasiparticle corrections $\Delta_k = E_k - \varepsilon_k$ to DFT single-particle energies ε_k, since it obviates the necessity of calculating dynamic screening. Indeed, the calculation of the dynamically screened Coulomb interaction W is by far the most computationally demanding part of GW calculations, where typically of $O(10^2)$ frequency points are required for converged results for the fully dynamic quasiparticle self energy with $\omega = E_k$ from Eq. (5.4) and (5.5).[108] Thus the static approximation can reduce the computational cost immensely. Nevertheless the static COHSEX approximation turns out to be fairly rough, and cannot be relied on, e.g. for accurate calculations of band gaps, as discussed below. Recently, Kang and Hybertsen,[112] have investigated the errors in the static COHSEX approximation at $T = 0$ by comparing each contribution to the corresponding term in the full GW quasiparticle energy. They found that while the static SEX approximation is generally a good approximation to the fully dynamic SEX, the static Coulomb hole approximation yields errors of order 10-20% to the fully dynamic COH terms for the occupied states. In addition, they suggest a method for correcting the static COH term which give significant improvements for both occupied and low lying unoccupied states.

5.1.2 Finite-temperature

We now derive the finite temperature generalization of the static COHSEX approximation to the GW quasiparticle self-energy. Our treatment follows *mutatis, mutandis*, from the zero-temperature theory with FT generalizations of G_0^T, W^T and Σ^T. Additional details are given in the Appendix D. To this end, we replace the time-ordered quantities in Eq. (5.1) with Matsubara quantities,[114]

$$\Sigma^M(k, i\omega) = -k_B T \int \frac{d^3q}{(2\pi)^3} \sum_{n_{even}} G_0^M(k+q, i\omega + i\omega_n) W^M(q, i\omega_n). \tag{5.9}$$

Then taking the analytic continuation to the real-ω axis, the fully dynamic FT retarded self-energy Σ^R in the GW approximation is given by[115]

$$\begin{aligned} \Sigma^R(k, \omega, T) &= \int_0^\infty d\omega' \int \frac{d^3q}{(2\pi)^3} D(q, \omega') \times \\ &\quad \times \left[\frac{f(\epsilon_{\mathbf{k}-\mathbf{q}}) + N(\omega')}{\omega + \omega' - \epsilon_{\mathbf{k}-\mathbf{q}} + i\delta} + \frac{1 - f(\epsilon_{\mathbf{k}-\mathbf{q}}) + N(\omega')}{\omega - \omega' - \epsilon_{\mathbf{k}-\mathbf{q}} + i\delta} \right], \end{aligned} \tag{5.10}$$

where $f(\varepsilon) = 1/[e^{\beta(\varepsilon-\mu)} + 1]$ is the Fermi factor, $\mu = \mu(T)$ the chemical potential, and $N(\omega) = 1/[e^{\beta\omega} - 1]$ the Bose factor, each with implicit temperature and electron density dependence, $\beta = 1/k_B T$ and $n = N/V = 3/4\pi r_s^3$ in the thermodynamic limit. The static exchange term is given by $\Sigma^x(k, T) = \int [d^3q/(2\pi)^3] f(\epsilon_{\mathbf{k}-\mathbf{q}}) v_q$. The spectral function D has implicit temperature dependence from that of the RPA dielectric function $\epsilon(q, \omega, T)$,

$$\epsilon(q, \omega, T) = 1 + 2v_q \int \frac{d^3k}{(2\pi)^3} \frac{f(\varepsilon_{k+q}) - f(\varepsilon_k)}{\omega - \varepsilon_{k+q} + \varepsilon_k}, \tag{5.11}$$

The imaginary part of $\epsilon(q, \omega, T)$ is analytic,[116, 117] and the real part is calculated via a Kramers-Kronig transform.

As in the $T = 0$ case, the fully dynamic self-energy at finite temperature and it's COH and SEX parts are obtained by evaluating the poles of G_0 and W respectively. The SEX terms with the Fermi factor arise from G_0, while the COH terms with the Bose factors come from the screened Coulomb interaction W. Separating these contributions in the fully

dynamic FT quasiparticle GW retarded self-energy yields

$$\Sigma^{SEX,R}(k,\omega) = -\int\frac{d^3q}{(2\pi)^3}f(\varepsilon_{\mathbf{k-q}})W^R(q,\omega-\varepsilon_{\mathbf{k-q}}) \tag{5.12}$$

$$\Sigma^{COH,R}(k,\omega) = \int_0^\infty d\omega'\int\frac{d^3q}{(2\pi)^3}D(q,\omega')\times \times\left[\frac{N(\omega')}{\omega+\omega'-\varepsilon_{\mathbf{k-q}}+i\delta}+\frac{1+N(\omega')}{\omega-\omega'-\varepsilon_{\mathbf{k-q}}+i\delta}\right]. \tag{5.13}$$

At finite T, Eq. (5.12) is identical in form to Eq. (5.4), apart from implicit temperature dependence in $f(\varepsilon)$ and $W^M(q,\omega)$. Eq. (5.13) reduces to Eq. (5.5) at $T=0$; however, the Bose factors $N(\omega)$ become increasingly important at finite T. In the limit of static screening, we therefore obtain the FT generalization of the COHSEX approximation. The real parts of the FT COHSEX approximation to Σ_k are similar to those for $T=0$ in Eq. (5.6) and (5.7)

$$\Sigma_k^{SEX}(T) = -\int\frac{d^3q}{(2\pi)^3}f(\varepsilon_{\mathbf{k-q}})W^R(q,0), \tag{5.14}$$

$$\mathrm{Re}\left[\Sigma_k^{COH}(T)\right] = \frac{1}{2}\int\frac{d^3q}{(2\pi)^3}W_p^R(q,0). \tag{5.15}$$

As at $T=0$ the static exchange term is given by $\Sigma^x(k,T)=\int[d^3q/(2\pi)^3]f(\varepsilon_{\mathbf{k-q}})v_q$. However, in contrast to the zero temperature case, the static approximation for the FT COH term is complex valued, with a negative imaginary part given by

$$\mathrm{Im}\left[\Sigma_k^{COH,R}(T)\right] = -\int\frac{d^3q}{(2\pi)^2}\lim_{\omega\to0^+}N(\omega)D(q,\omega). \tag{5.16}$$

Note that at low frequency, $D_q(\omega)\propto\omega$ due to particle-hole continuum excitations and $N(\omega)\to k_BT/\omega$ mirrors the high temperature behavior. Thus, the imaginary part of the static COH contribution to Σ increases with temperature. Explicit calculations, however, show that the imaginary part of the static COH term is quite small at all temperatures compared to the contribution from the dynamic COHSEX term.

5.2 Static vs Dynamic COHSEX

As an illustration of the FT theory, we first compare the static and fully dynamic SEX and COH contribution to the quasiparticle GW self-energy on the energy shell $\Sigma_k=\Sigma(k,E_k)$ for

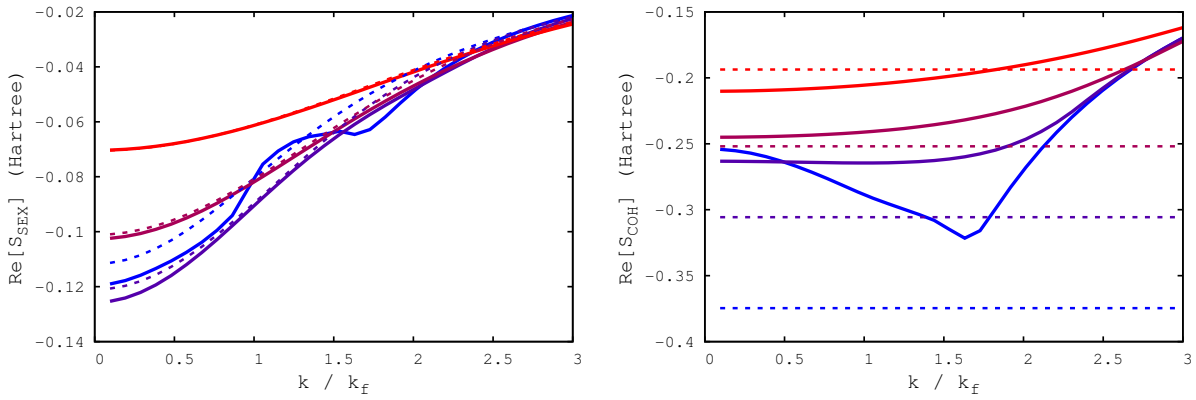

Figure 5.1: (Color online) Results for the SEX (left) and COH (right) contributions to the static (dashed) and full dynamic (solid) quasiparticle self-energy vs k/k_F at various temperatures T/T_F for the homogeneous electron gas for $r_s = 2.0$: (from blue to red) the curves denote T/T_F =0.01, 0.5, 1.0, and 2.0. Note that the COH contribution is always significantly larger in magnitude than the SEX and persists to higher k/k_F, while the SEX becomes for unoccupied states above k_F.

the homogeneous electron gas (Fig. 5.1 left) from Eq. (11-14). For all cases the agreement between static and fully dynamic SEX contribution is quite good, both at low and high k, and become increasingly accurate with increasing temperature. On the other hand the COH terms dominate the GW self-energy Σ_k for all k, but there are substantial errors in making the static approximation at low temperatures, which become smaller with increasing temperature. The dispersion of the fully dynamic COH and SEX contributions largely cancels for $k < k_F$ at low temperature. However, this cancelation does not persist at higher temperatures ($T/T_F > 0.5$), where the dispersion of both contributions is positive. It is important to note that the static COH contribution Σ_k^{COH} is actually constant, independent of k, and hence entirely local. In contrast the dynamic COH terms become strongly momentum dependent beyond a cross-over point $k_p = [2(\omega_p + \varepsilon_F)]^{1/2}$, corresponding to the onset of plasmon-excitations, with the real part approaching zero asymptotically at high momenta and the imaginary part becoming large. Thus for unoccupied states at high $k > k_p$ dynamic

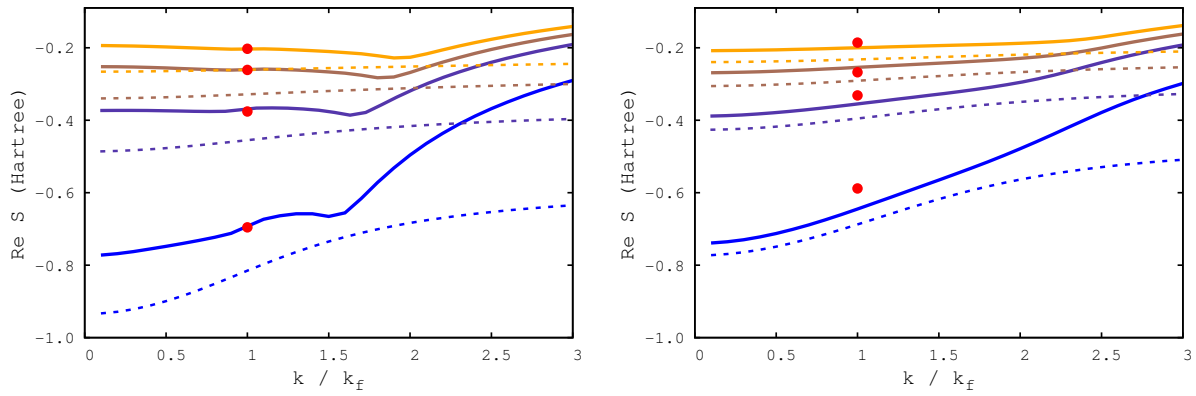

Figure 5.2: (Color online) The real part of static COHSEX approximation (dashed) vs fully dynamic self-energy (solid) for various densities: (from blue to orange) r_s =1.0, 2.0, 3.0, 4.0 at $T/T_F = 0.01$ (left) and 1.0 (right). Note that the high temperature behavior is considerably smoother than near $T = 0$ and the change in behavior beyond about $k = k_p$ reflecting the onset of plasmon excitations. For reference the LDA-$v_{xc}(T)$[113, 101] for each r_s are added as circles at k_F.

corrections to the COHSEX approximation are essential, and necessary to account for the substantial broadening of the high energy unoccupied states.

This behavior is illustrated in Fig. 5.2 with a comparison between the static total static COHSEX and and fully dynamic self-energy for various densities $r_s = 1, 2, 3$ and 4, and $T/T_F = 0.01$ and 1. Note also that the static approximation exhibits considerably less variation with respect to r_s, k, and T than the fully dynamic results. At high T, the dispersion in the quasiparticle self-energy Σ_k is also fairly well represented by the total static COHSEX for $k < k_p$, and has a much smoother variation with temperature than the low T behavior. For comparison we also show the FT-DFT exchange-correlation potential v_{xc} for $r_s = 1, 2, 3$ and 4. As expected, the value of v_{xc} is nearly identical to the quasiparticle energy correction at the $k = k_F$. However, at high T, the Fermi surface broadens and ceases to be a precisely defined concept, and the chemical potential can even lie below the bottom of the band. Thus at high T, $v_{xc}(T)$ is no longer equivalent to the quasiparticle correction at the

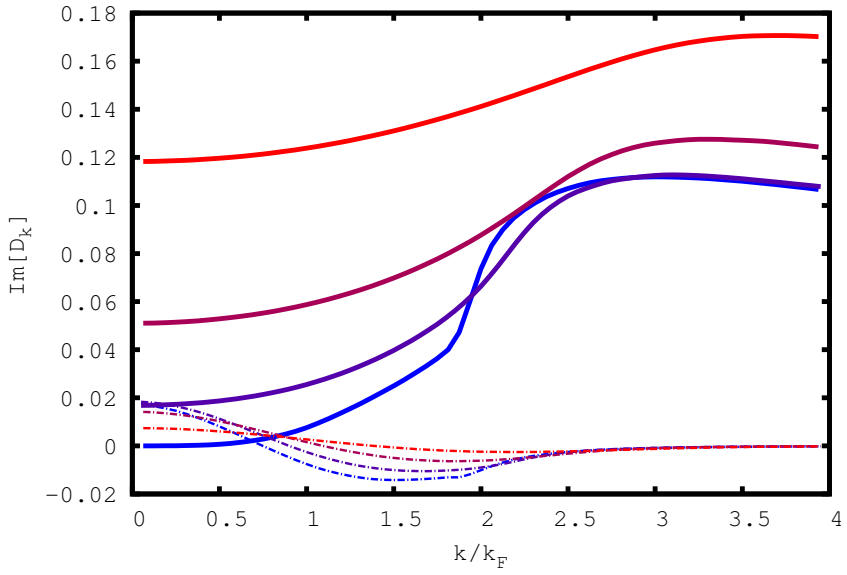

Figure 5.3: (Color online) Fully dynamic COH (solid) and SEX (dashed) contributions to the imaginary part of the quasiparticle correction to the DFT energy ε_k vs k/k_F for $r_s = 4.0$, for various temperatures: (from blue to red) T/T_F =0.01, 0.5, 1.0, and 2.0. Note that the dominant contribution comes from the COH terms, while the dynamic contributions to the SEX from particle-hole excitations are significant only near k_F.

Fermi level. Although the static COHSEX approximation captures much of the quasiparticle correction to the DFT, significant errors remain, especially for excited states at high $k > k_p$. We show in Fig. 5.3 the imaginary part of the quasiparticle self-energy $|\mathrm{Im}\,\Delta_k = \mathrm{Im}\,\Sigma_k|$ vs temperature from the COH (solid) and SEX (dashed) contributions at various temperatures. Unlike the fully dynamic results, the static COHSEX has zero imaginary part at $T = 0$, while at finite T, the COH term alone contributes, resulting in a value of $\approx -0.02i$ H at $T/T_F = 4$, i.e., about 10% of the GW self-energy.

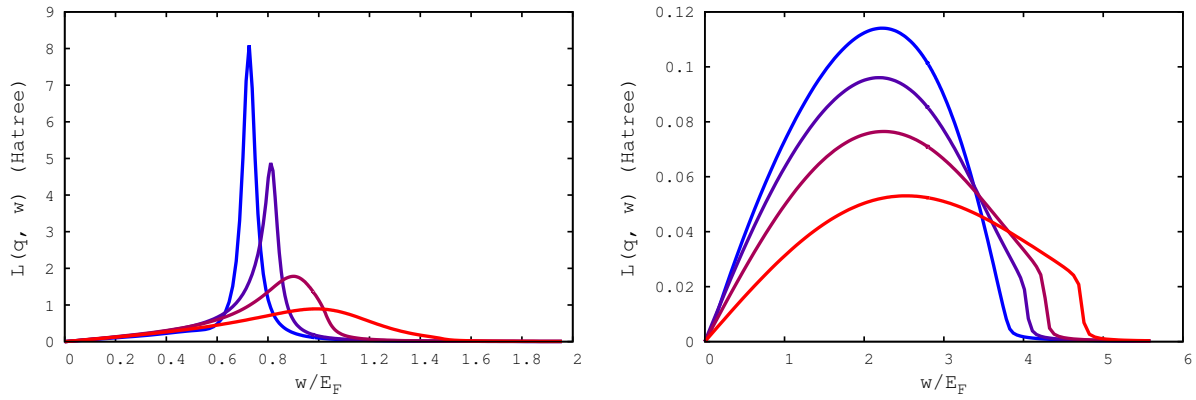

Figure 5.4: (Color online) The electron energy-loss function $L(q,\omega) = |\mathrm{Im}\ \epsilon^{-1}(q,\omega)|$ for $r_s = 2.0$ at various temperatures: (from blue to red) T/T_F =0.01, 0.5, 1.0, and 2.0 for momentum $q/k_F = 0.5$ (left) and 2.0 (right).

5.3 Analysis

In an effort to better understand the static COHSEX approximation and dynamic corrections to the GW self energy, we now present a brief analysis. Physically the GW approximation describes the quasiparticle self-energy due to a dynamically screened exchange-correlation hole. The separation into COH and SEX terms arises naturally in the GW approximation from the poles of W and those of G_0 respectively. The static approximations then amount to replacing the frequency argument of $W(q, E_k - \varepsilon_{\mathbf{k-q}})$ with zero. Thus the static FT screened Coulomb interaction $W(q,0) = 4\pi/[q^2 + \kappa(T)^2]$ has a temperature dependent screening constant $\kappa(T)$ that varies from the Thomas-Fermi value at $T = 0$ to the Debye-Hückel limit at high T.[100, 113] The FT behavior of the loss function $L(q,\omega) = |\mathrm{Im}\,\epsilon^{-1}(q,\omega)|$ is illustrated in Fig. 5.4. At high temperature, higher energy plasmons contribute less to the full COH due to the broadening. By examining Eq. (5.15), the full COH gets closer to the static COH as the blue-shifted plasmons contributes less to adiabatic accumulation of the Coulomb hole from W_p.

Why is the static approximation so good for the SEX term, while at best only fair for

the COH term and only for the occupied levels? In an attempt to answer this question, we examine Eq. (5.12) and (5.13) in the limit of zero momentum and low temperature, as investigated in detail e.g., by Lundqvist.[118] for the $T = 0$ case. For the SEX term, the Fermi function and the screened Coulomb potential have the same argument $q^2/2$, up to a sign. As a result, the frequency argument in $W(q, \omega)$ is limited to $\omega < \epsilon_F$, and hence the substantial variation of W near the plasmon excitation energy ω_p - which is usually larger than the Fermi energy ϵ_F for low to normal ($r_s \approx 2 - 6$) densities - is never accessed. At high momenta $k/k_F \gg 1$, the Fermi function acts to ensure that q/k_F must also be large for any significant contribution. Consequently the frequency argument of W is large only when the momentum is also large. This suppresses the matrix element in the total since $W(q, \omega) \propto 1/q^2$ for large q. Consequently dynamic corrections are small for the SEX term. In contrast, the static COH term in Eq. (5.13) has no limitations on the arguments of $W(q, \omega)$. Physically, the dynamic contributions to the SEX arise only from low energy excitations, e.g., the particle-hole continuum. In contrast the dynamic COH term includes excitations at all energies and its dynamic contributions are dominated by plasmon-excitations and to a much lesser extent particle-hole excitations. These effects are evident in the imaginary part of the self-energy in Fig. 5.3, where $\mathrm{Im}\,\Sigma^{SEX}(k, E_k)$ is limited to momenta near or below k_F, while that for $\Sigma^{COH}(k, E_k)$ is appreciable even beyond the onset of plasmon excitations k_p. Another consequence of the static approximation is that the COH contribution is completely local, i.e., k-independent. This is a drastic approximation, and fails to account for the substantial variation of the self-energy for $k > k_p$ due to plasmon excitations.

Although the COHSEX approximation is perhaps most useful for estimates of the quasiparticle self energy, it is interesting to consider other corrections to the quasiparticle approximation at finite T. These are reflected for example, in the the renormalization factor $Z_k = [1 - \partial\Sigma(k, \omega)/\partial\omega]^{-1}_{\omega=\varepsilon_k}$. Since deviations of Z_k from unity correspond to the fraction of satellites in the spectral function, Z_k provides a diagnostic of the validity of the quasiparticle approximation. For a more detailed analysis and illustrations of the behavior of the finite-T spectral function, we refer the reader to Ref[113, 119]. Fig. 5.5 shows the renormalization

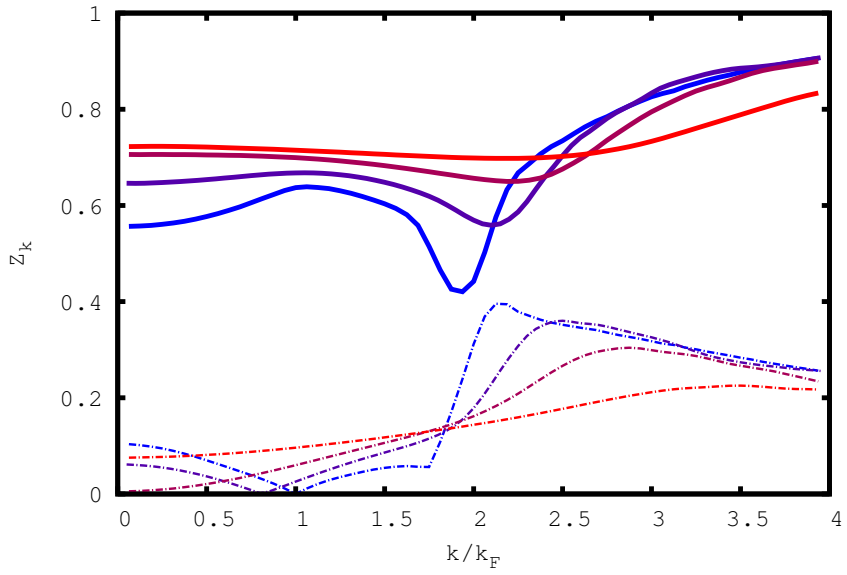

Figure 5.5: Real (solid) and imaginary (dashed) parts of the renormalization constant Z_k vs k/k_F for r_s=4.0 at (blue to red) T/T_F =0.01, 0.5, 1.0, and 2.0.

factor as a function of k for $r_s = 4.0$ and T/T_F =0.01, 0.5, 1.0, and 2.0. Clearly the quasiparticle approximation becomes increasingly valid for very high energy states well above the plasmon frequency $\varepsilon_k \gg \omega_p$. However, this is the range for which the static COH has the largest errors. Since deviations of Z_k from unity correspond to the fraction of satellites in the spectral function, Z_k provides a diagnostic of the validity of the quasiparticle approximation. For a more detailed analysis and illustrations of the behavior of the finite-T spectral function, we refer the reader to Refs. [113, 119]. Note in addition that the renormalization constant is $Z_k \approx 0.75$ for $r_s = 4$, even at high T/T_F, indicating that the quasiparticle energy correction is reduced in magnitude compared to that calculated at the bare energy. This suggests that errors in the static COHSEX approximation of order 20% may well be a best case scenario. Thus while the renormalization constant shows the importance of satellites in the single particle spectrum, it is not a good diagnostic for the quality of the static approximation to the quasiparticle energies.

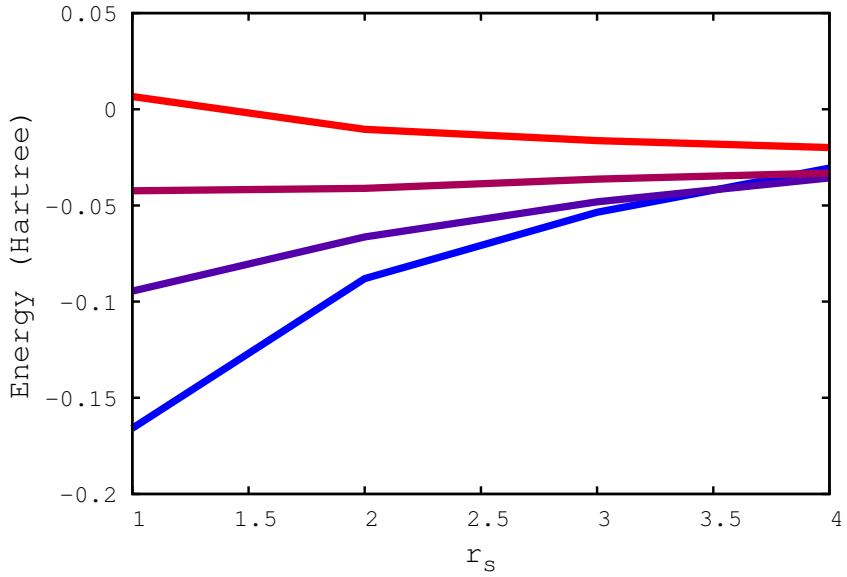

Figure 5.6: (Color online) Dynamic correction to COHSEX self-energy $\Sigma(k, E_k) - \Sigma_k^{COHSEX}$ at the Fermi level k_F as a function of r_s: from blue to red, the curves denote T/T_F =0.01, 0.5, 1.0, and 2.0.

Finally, Fig. 5.6 shows the magnitude of the dynamic corrections to the static COHSEX self-energy at the Fermi momentum as a function of r_s. These results show that for all temperatures, the dynamic correction is smoothly decreasing (increasing) with increasing r_s for $T > (<) T_F$. This behavior suggests that a simple additive correction to the DFT exchange correlation potential may be a reasonable approximation to correct the static COHSEX approximation for states $0 < k < k_p$.

5.4 Summary

We have generalized the COHSEX approximation to the *GW* self-energy to finite temperatures, with an explicit treatment of both the COH and SEX contributions. We find that the FT COHSEX approximation is similar in many-respects to that for $T = 0$. Formally the separation of the fully dynamic *GW* self-energy into COH and SEX terms and their definitions

are similar to their counterparts at $T = 0$, apart from explicit temperature dependence in their ingredients. The static SEX approximation continues to be a very good approximation to the fully dynamic SEX over a broad range of densities, temperatures, and momenta, but is only substantial for occupied levels below about k_F. The COH term is generally much larger than the SEX and persists to higher energies, with a cross-over at the onset of plasmon excitations at $k = k_p$. While the static COH approximation is only fair for mostly occupied and low-lying unoccupied states $k < k_p$ at low temperture, it completely fails to describe dynamic effects in the $\Sigma^{COH}(k, E_k)$ at high $k > k_p$. This behavior is similar to that in the analysis by Kang and Hybertsen for the $T = 0$ case.[112] However, a key difference for finite-T is that the static COHSEX approximation becomes complex valued, even at the Fermi level, with an imaginary part that grows with temperature. While these deficiencies can be remedied for the nominally occupied states, e.g., by generalizing the extended COHSEX approximation[112] to finite temperature, the static COH approximation still retains it's unphysical spatial locality, independent of k. This limitation has the consequence that at high T, equilibrium properties will be increasingly error-prone since they depend on the high momentum behavior of the electrons. Nevertheless, the static COHSEX approximation does provide a fair approximation of corrections to DFT for quasiparticle energies with typical errors of about 10-20%. While this degree of accuracy provides rough estimates of quasiparticle corrections to DFT, dynamic corrections are always important. Eventually, the FT COHSEX approximation could replace the T=0 Hedin-Lundqvist self-energy approximation in FEFF.

Chapter 6

SUMMARY AND CONCLUSIONS

In this thesis, we presented several contributions to the theory of finite-temperature and non-equilibrium x-ray absorption. This work opened up new possibilities for efficient simulation of finite-temperature XAS including dynamics and non-equilibrium behavior in generic systems up to the WDM regime. We extended the current theory for calculating XANES based on the multiple-scattering framework by including the temperature correction to the exchange-correlation. The x-ray absorption depends on electron temperature through the Fermi-Dirac distribution and self-consistent electronic density. Lattice dynamics are included by averaging the x-ray absorption over a set of configurations generated by the dynamical matrix and the molecular dynamics. Next, we developed the FEFF10 code which implements the finite-temperature theory for the calculation of x-ray absorption. The finite temperature theory can be combined with ab initio molecular dynamic simulation or Monte Carlo sampling to model non-equilibrium systems. The electron temperature can be estimated from XAS measurement by combining the theory with the energy transport equation in the form of a two-temperature model. In addition, we demonstrated the FEFF10 code on three examples: warm dense Al, warm dense Cu, and $[Fe/MgO]_8$ heterostructure. We showcased the effects of the finite temperature exchange-correlation effects to the XAS of Al. We showed an example of paramagnetic system, Cu and an example of ferromagnetic system, $[Fe/MgO]_8$. We analyzed the XANES of $[Fe/MgO]_8$ right after the laser heating and inferred the relaxation dynamics of the electrons and lattice. Lastly, we developed a finite temperature generalization of the quasiparticle self-energy within the COHSEX approximation. Our analysis highlighted the importance of dynamical response of the coulomb-hole correlation even at finite temperature. In this chapter, we review these contributions and

propose directions for future work.

6.1 Theory of Finite-Temperature XAS

In chapter 2, we showed the generalization of the quasiparticle XAS. We formulated the x-ray absorption cross section using the one electron Green's function. Finite temperature corrections to the ground states and excited states were introduced in the form of exchange-correlation potentials and quasiparticle self-energy. The theory can be combined with ab initio molecular dynamics or Monte Carlo sampling for non-equilibrium systems as described in chapter 3. This development resulted in the finite-temperature XANES workflow shown in Fig 6.1. We illustrated this theory on warm dense Al, warm dense Cu and $[Fe/MgO]_8$ heterostructure in chapter 4. In particular, our calculations showed the difference in absorption edge temperature response in simple metal like Al and in $3d$ transition metal like Cu. In addition, ferromagnetic system exhibits magnetic response that is measurable in XANES. We analyzed the changes in the Fe L3-edge and O K-edge of $[Fe/MgO]_8$ in response to a demagnetizing laser excitation. We compared the role of exchange splitting and the Fermi-Dirac broadening on Fe L3-edge response. The O K-edge in the $[Fe/MgO]_8$ exhibits Debye-Waller-like attenuation and is not sensitive to the changes in the electron temperature. With the new code, we provided an alternative to compute XANES at finite temperature without the need of a constructing a temperature dependent pseudopotential.

6.2 Finite-Temperature COHSEX Self-Energy

In chapter 5, we derived the finite-temperature generalization of the quasiparticle self-energy within the COHSEX approximation from the Matsubara formalism. Our explicit comparisons of the static and dynamic screened exchange and Coulomb-hole contributions for the homogeneous electron gas showed that the static SEX approximation agrees well with the fully dynamic SEX at all temperatures and densities. In contrast, dynamic corrections to the COH approximation are always significant, especially for high energy unoccupied states. We also showed that the COHSEX quasiparticle self-energy is complex valued at finite tem-

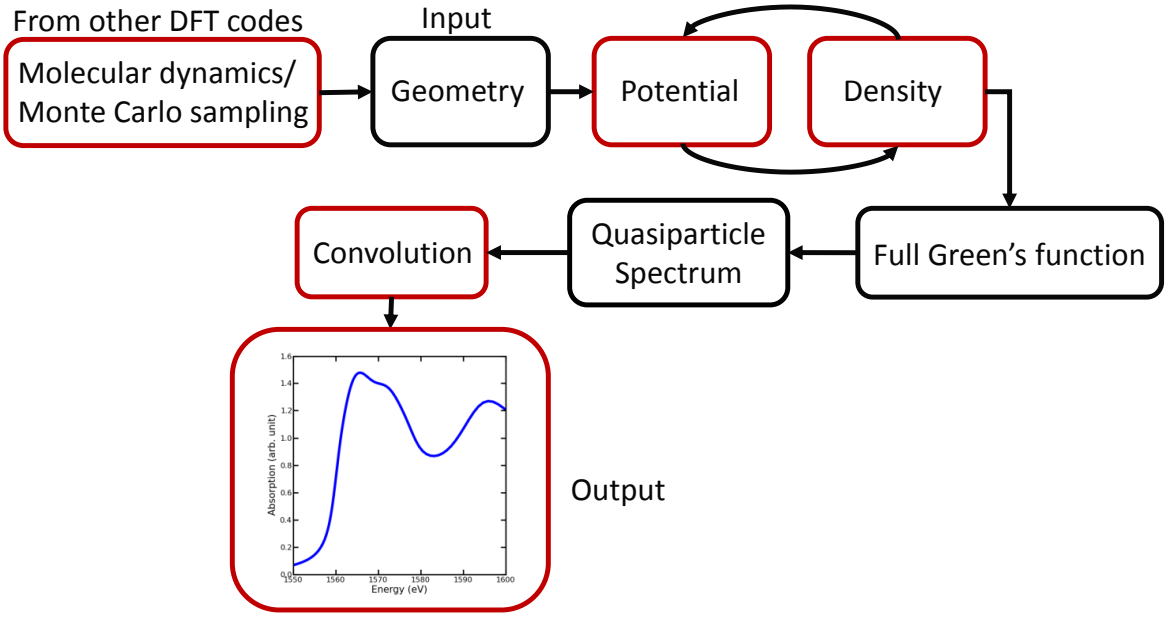

Figure 6.1: Finite-temperature XANES workflow in FEFF10. The red boxes highlight the temperature dependent steps in the workflow.

perature even at the Fermi level.

6.3 Future Work

The theory and code developed in this work make possible general calculations of XAS at finite temperature in systems throughout the periodic table for both equilibrium and non-equilibrium systems. However, there are many possible ways to extend the theory. A few examples are listed below:

- Finite-temperature Many-body Effects

  The finite-temperature quasiparticle theory presented in this work ignores many-body effects such as shake-up, shake-off, and exciton excitations which has been shown to be important for correlated systems. Moreover, our theory treats the amplitude reduction factor S_0^2, the many-body response of a system to the creation of the core hole,

as a constant. As a further matter, the quasiparticle GW self-energy predicts plasmon satellites far away from the quasiparticle energy. Further, only the quasiparticle excitation is included in the quasiparticle theory of XAS and the satellite contribution is neglected. A recent development in the finite-temperature retarded cumulant formalism by Kas et al. [120] improves the treatment of quasiparticle GW self-energy by introducing implicit vertex correction at finite temperature. The cumulant formalism is no more complex than the GW self-energy calculation and requires minimum modification to the existing theory and code. This method has been shown to yield good agreement in exchange-correlation energies and potentials with state of the art quantum Monte-Carlo simulations [32, 102]. While the cumulant formalism provides a better model for the plasmon satellites, neutral excitations like the electron-hole pair can be treated in the Bethe-Salpeter framework.[121] Further investigation into finite-temperature excitons up to the warm dense regime is required.[29, 122, 123]

- Efficient Parameterization of Finite-temperature Self-Energy

  Computation of GW self-energy is computationally expensive but is necessary for x-ray response. In a XANES calculation which typically takes a few CPU hours to compute on modern PCs and laptops, a full calculation of GW self-energy can quickly become a bottleneck. Efficient approximations and algorithms such as the plasmon-pole model and SternheimerGW [124] have been introduced for zero temperature GW self-energy. In our current code, we approximate the self-energy with the Hedin-Lundqvist plasmon-pole model [58]. This approximation is sufficiently accurate for XANES. To the best of our knowledge, there is currently no similar parameterization for the finite-temperature self-energy. To address the shortage of efficient approximation, our work on the finite temperature generalization of COHSEX can be adapted to an efficient parameterization of the quasiparticle self-energy at finite temperatures. In addition, generalization of Kang et al.'s [68] enhanced static approximation to the dynamical Coulomb-hole correction can potentially alleviate the need of a full finite-temperature

GW self-energy calculation.

- Self-consistent Spin-polarized Density

  The spin-polarized density of state is currently determined by the self-consistent spin-unpolarized density of state. In addition, we consider only the spin polarization of the d and f-electrons spin polarization and neglect the spin contributions from the s and p-electrons. A more accurate treatment of the magnetic systems requires the self-consistent spin-polarized density of state for all the shells.

6.4 Concluding Remarks

We have extended the theory of XAS to finite temperatures and non-equilibrium behavior. The theory has been implemented in an efficient general purpose code FEFF10, which is applicable to systems throughout the periodic table. The theory and code have been tested against modern experiment and are in very good quantitative agreement. These developments have considerable promise for the interpretation of experiments in many fields, in particular for studies of warm-dense-matter and non-equilibrium behavior.

Appendix A

NUMERICAL SOLUTION OF CONVOLUTION INTEGRAL

Direct integration of Eq. (2.16) along the real axis contains poles from the Green's function G. We can extend it to the complex plane where G is smooth as discussed in section 2.3.1. However, the Lorentzian also contributes two additional poles to the contour integral. It can be numerically unstable when $n\pi kT = \Gamma$ for some odd integer n. One of the poles from the Lorentzian ($E = \omega + i\Gamma$) will lie on the complex contour. The typical approach to numerical integration involving a simple pole is to isolate the problematic term from the integrand. Thus, the effective quasiparticle cross section (σ_{eff}) becomes

$$\begin{aligned}\sigma_{eff}(\omega) &= -4\pi\frac{\omega}{c}S_0^2\mathrm{Im}\sum_{ill'} f_T(\epsilon_i)\int d\omega'\Big[g(\omega') - g(\omega+i\Gamma)\Big]\frac{\pi/\Gamma}{(\omega-\omega')^2+\Gamma^2}\Big[1-f_T(\omega'+\epsilon_i)\Big] \\ &\quad + g(\omega+i\Gamma)\int d\omega'\frac{\pi/\Gamma}{(\omega-\omega')^2+\Gamma^2}\Big[1-f_T(\omega'+\epsilon_i)\Big] \qquad \text{(A.1)}\end{aligned}$$

where $g(\omega)$ is the matrix dipole element $\langle i|\hat{d}\ G_{l0,l'0}(\omega+\epsilon_i)\ \hat{d}^\dagger|i\rangle$. The first term can be extended to the complex plane as discussed in Section 2.3.1 and the second term can be integrated on the real axis since it does not contain any poles along the real axis.

Appendix B

HARMONIC APPROXIMATION OF X-RAY ABSORPTION

B.1 Derivation of Dynamical Matrix

In this section, we derive the expectation of value of an observable $A(\mathbf{R})$ within the harmonic approximation to the nuclear potential V. Starting from the Hamiltonian for the nuclei in Eq. (3.9) and Bloch's theorem $u_{n\alpha i} = \frac{1}{\sqrt{M_\alpha}}\varepsilon_{\alpha i}\exp[i\mathbf{q}\cdot\mathbf{R}_n - i\omega t]$, we can obtain the dynamical matrix equation by extremize the Euler-Lagrange equation:[125]

$$\omega^2(\mathbf{q})\varepsilon_{\alpha i} = \sum_{\alpha'}\frac{\Phi_{\alpha i,\alpha' i'}(n')}{\sqrt{M_\alpha}\sqrt{M_{\alpha'}}}\varepsilon_{\alpha'}e^{i\mathbf{q}\cdot\mathbf{R}_{n'}} \tag{B.1}$$

where $\Phi_{\alpha,\beta}(n)$ is the second derivative of V in the n-th unit cell and $\mathbf{R}_n$ is the Bravais lattice. If we can define a new quantity called the dynamical matrix $\mathbf{D}(\mathbf{q})$:

$$D_{\alpha i,\alpha' i'}(\mathbf{q}) = \sum_n \frac{\Phi_{\alpha i,\alpha' i'}(n)}{\sqrt{M_\alpha M_{\alpha'}}}e^{i\mathbf{q}\cdot\mathbf{R}_n} \tag{B.2}$$

$$D_{\alpha i,\alpha' i'}(\mathbf{R}_n) = \sum_{\mathbf{q}} D_{\alpha i,\alpha' i'}(\mathbf{q})e^{-i\mathbf{q}_n\cdot\mathbf{R}_n} \tag{B.3}$$

then we can rewrite Eq. (B.1) into Eq. (3.11).

$$\sum_{\alpha' i'}\Big(D_{\alpha i,\alpha' i'}(\mathbf{q}) - \delta_{\alpha i,\alpha' i'}\omega_\mu^2(\mathbf{q})\Big)\varepsilon^{(\mu)}_{\alpha' i'}(\mathbf{q}) = 0 \tag{B.4}$$

Once the eigvectors $\varepsilon^{(\mu)}$ are identified, any displacement $\vec{u}_{n\alpha}$ can be expressed as a linear combination of the eigenvectors:

$$\vec{u}_{n\alpha}(t) = \frac{1}{\sqrt{N}}\sum_{\mathbf{q},\mu} Q^{(\mu)}(\mathbf{q},t)\frac{1}{\sqrt{M_\alpha}}\bar{\varepsilon}^{(\mu)}(\mathbf{q})e^{i\mathbf{q}\cdot\mathbf{r}_{n\alpha}} \tag{B.5}$$

where $Q^{(\mu)}$ is called the normal coordinate and $r_{n\alpha}$ is the position of atom α with respect to the reference origin $\mathcal{O}$. The harmonic time dependence is absorbed into the definition of $Q^{(\mu)}$

and the representation for $Q^{(\mu)}$ is not unique. Since $\hat{S}_{n\alpha}(t)$ is real, $Q^{(\mu)*}(\mathbf{q}) = Q^{(\mu)}(-\mathbf{q})$. By substituting Eq. (B.5) back into the Hamiltonian in Eq. (3.9), we can rewrite the equation as[126]

$$H = \frac{1}{2}\sum_{\mathbf{q},\mu}\left(\left|\dot{Q}^{(\mu)}(\mathbf{q})\right|^2 + \omega_\mu^2(\mathbf{q})\left|Q^{(\mu)}(\mathbf{q})\right|^2\right) + V^{BO} \tag{B.6}$$

It is straightforward to show that the conjugate momenta is given by $P(\mathbf{q}) = \dot{Q}(\mathbf{q})$ and that they satisfy the canonical commutation relation $\left[Q^{(\mu)*}(\mathbf{k}), P^{(\nu)}(\mathbf{q})\right] = i\hbar\delta_{\mu,\nu}\delta_{\mathbf{k},\mathbf{q}}$. Therefore, we can transform the canonical variables into the creation-annihilation operators $\hat{a}^\dagger(\hat{a})$ with the standard transformation:

$$Q^{(\mu)}(\mathbf{q}) = \sqrt{\frac{\hbar}{2\omega_\mu(\mathbf{q})}}\left(\hat{a}_\mu(\mathbf{q}) + \hat{a}_\mu^\dagger(-\mathbf{q})\right) \tag{B.7}$$

$$P^{(\mu)}(\mathbf{q}) = -i\sqrt{\frac{\hbar\omega_\mu(\mathbf{q})}{2}}\left(\hat{a}_\mu(\mathbf{q}) - \hat{a}_\mu^\dagger(-\mathbf{q})\right) \tag{B.8}$$

Therefore, the Eq. (B.6) can be expressed as

$$H = \sum_{\mathbf{q},\mu}\hbar\omega_\mu(\mathbf{q})\left(\hat{a}_\mu^\dagger(\mathbf{q})\hat{a}_\mu(\mathbf{q}) + \frac{1}{2}\right) + V^{BO} \tag{B.9}$$

which is a collection of independent harmonic oscillators. In the normal coordinates, the n-th excited nuclear wavefunction χ_n is expressed as a product of 1-dimensional quantum harmonic wavefunctions ϕ.

$$\chi_n = \Pi_{\mathbf{q},\mu}\phi_{n_{\mathbf{q},\mu}}(Q^{(\mu)}(\mathbf{q})) \tag{B.10}$$

$$n = \sum_{\mathbf{q},\mu} n_{\mathbf{q},\mu} \tag{B.11}$$

$$\phi_{n_{\mathbf{q},\mu}}(Q^{(\mu)}(\mathbf{q})) = \frac{(2\pi a_{\mathbf{q},\mu}^2)^{-1/4}}{\sqrt{2^{n_{\mathbf{q},\mu}} n_{\mathbf{q},\mu}!}} H_{n_{\mathbf{q},\mu}}\left(\frac{Q^{(\mu)}(\mathbf{q})}{\sqrt{2}a_{\mathbf{q},\mu}}\right)\exp\left[-\frac{Q^{(\mu)}(\mathbf{q})^2}{4a_{\mathbf{q},\mu}^2}\right] \tag{B.12}$$

where H_n is the Hermite polynomial, $a_{\mathbf{q},\mu} = 1/\sqrt{(2M_p\omega_\mu(\mathbf{q}))}$ is the normal length and M_p is some reference mass.

Within the harmonic potential approximation, the thermal expectation value of an observable $A(\mathbf{R})$ can be expressed as [127]:

$$\begin{aligned}
\langle A\rangle_T &= \frac{1}{Z}\sum_{n=0}^{\infty} e^{-\beta E_n}\langle\chi_n|A(\mathbf{R})|\chi_n\rangle \\
&= \frac{1}{Z}\sum_{n=0}^{\infty} e^{-\sum_{n_\nu}\beta E_{n_\nu}}\prod_{\nu=1}^{3N}\langle\phi_{n_\nu}|A(\mathbf{R})|\phi_{n_\nu}\rangle \\
&= \int\prod_{\nu=1}^{3N} dx_\nu\ A(\mathbf{R})\sum_{n_\nu=0}^{\infty}\|\phi_{n_\nu}(x_\nu)\|^2\frac{\exp[-\beta E_{n_\nu}]}{Z_\nu} \\
&= \int\prod_{\nu=1}^{3N} dx_\nu\ A(\mathbf{R})\left(\frac{1}{\sqrt{2\pi\langle x_\nu^2\rangle_T}}\exp\left[-\frac{x_\nu^2}{2\langle x_\nu^2\rangle_T}\right]\right)
\end{aligned} \tag{B.13}$$

where $\langle x_\nu^2\rangle_T = a_\nu^2(2n_B(\Omega_\nu,T)+1)$ and $n_B(\omega,T) = 1/(\exp(\omega/kT)-1)$. The integral can be easily approximated by importance sampling. The set of independent random configurations $\mathbf{R}$ are generated from a standard normal z vector:

$$\mathbf{R}_i = \mathbf{R}_i^0 + \sqrt{\frac{M_p}{m_i}}\sum_\nu e_i^\nu\ z_\nu\sqrt{\langle x_\nu^2\rangle_T} \tag{B.14}$$

where $\mathbf{R}_i^0$ is the equilibrium position of the i-th atom.

B.2 Debye-Waller Factor

The Debye-Waller factor $2k^2\sigma^2(T)$ quantifies the thermal disorder in x-ray absorption where σ^2 is the mean-square relative displacement and k is the photo-electron wave number. σ^2 is dependent on the path chosen between two atoms. For a given path R, σ^2 is expressed as[128]

$$\sigma^2(T) = \frac{1}{2\mu}\int_0^\infty\frac{d\omega}{\omega}\coth\left(\frac{\beta\omega}{2}\right)\rho(\omega) \tag{B.15}$$

where μ is the reduced mass for the atoms along the path R, ρ is the projected vibrational density of state (VDOS) along path R and $\beta = 1/k_BT$. The vibrational density of state ρ can be approximated with the correlated Debye model which yield good results for isotropic systems.[129] Within the correlated Debye model, the projected VDOS is given by[128]

$$\rho(\omega) = \frac{3\omega^2}{\omega_D^3}\left(1-\frac{\omega R/v}{\omega R/v}\right) \tag{B.16}$$

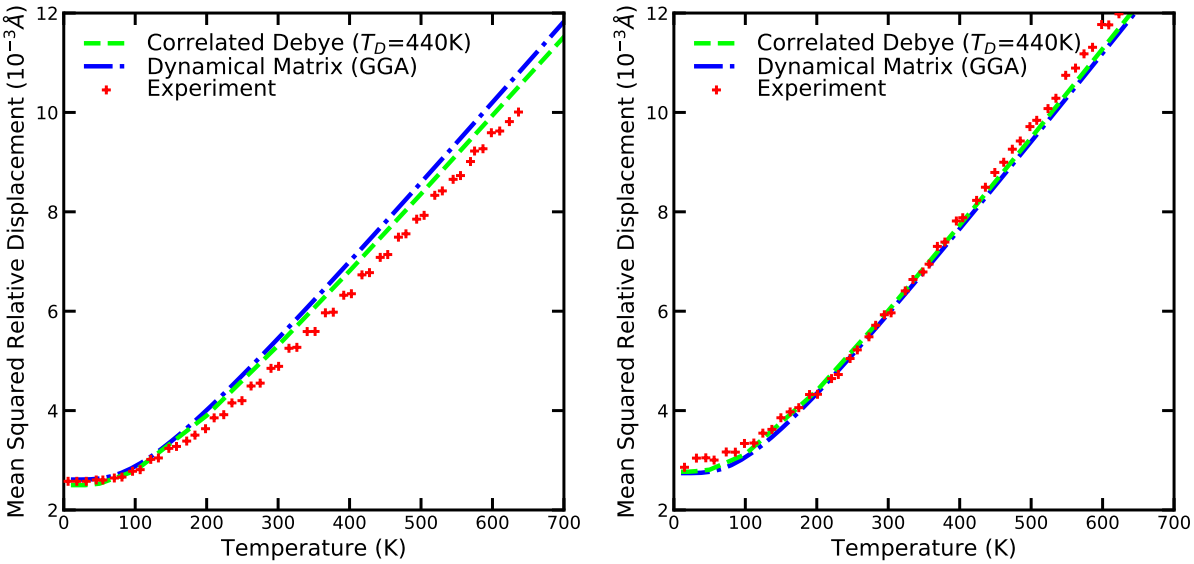

Figure B.1: Temperature dependence of $\sigma^2(T)$ for the nearest neighbor (left) and next nearest neighbor (right) single scattering path in iron. The $\sigma^2(T)$ computed using the dynamical matrix with GGA functional (blue) is compared to the correlated Debye model (green) and experiment measurements [131] (red).

where $\omega_D = k_B T_D$, $v = \omega_D / k_D$, T_D is the Debye temperature, $k_D = (6\pi^2 a)^{1/3}$ and a is the atomic density number. The first principle based approach to VDOS involves the use of Lanczos algorithm to compute the phonon Green's function matrix element[130]

$$\rho(\omega) = \mathrm{Im}\langle 0 | \frac{1}{\omega + D + i\delta} | 0 \rangle \tag{B.17}$$

where $|0\rangle$ is a random initial state for the Lanczos procedure, D is the dynamical matrix introduced in the previous section. In Fig B.1, we compare $\sigma^2(T)$ for the correlated Debye model and the dynamical matrix approach using the GGA functional with the experiment for the nearest neighbor and next nearest neighbor single scattering path in iron. The GGA functional is known to produce a stiff bond which results in an overestimation of $\sigma^2(T)$.[129]

Appendix C

FEFF10 FINITE-TEMPERATURE CODES

C.1 Finite-temperature Related Cards

FEFF10 introduces two new control cards related to the finite-temperature calculation of XANES: `TEMP` and `SCFTH`. The `TEMP` card is required setting the electron temperature. The `SCFTH` card is an optional card that sets the parameters for the finite-temperature SCF. In this section, we provide the description and arguments for the cards. A complete documentation of FEFF10 can be found at feffproject.org.

TEMP `etemp iscfxc`

```
Description: Sets electronic temperature and exchange-correlation potential
             etemp:  in unit of eV [default: 0]
             iscfxc: 11 - von-Barth Hedin 1971 [default]
                     12 - Perdew-Zunger
                     21 - Perrot Dharma-Wardana 1984
                     22 - KSDT
```

SCFTH `iscfth emaxscf negrid nmu xntol`

```
Description: Sets the parameters for thermal SCF calculation.
             iscfth: 2 - Use exact integral [default]
             emaxscf: Set upper bound of energy grid
                      if 15kT is smaller than emaxscf [default: 68.0275eV]
             negrid: Number of energy points [default: 320]
             nmu: Number of iterations for chemical potential [default: 100]
             xntol: Tolerance for electron counts [default: 1e-4]
```

C.2 Description of Subroutines

In this section, we briefly describe the main subroutines for finite-temperature calculation in alphabetical order. The source codes for each subroutines are available at `https://github.com/times-software/feff10`.

1. `FF2X/m_thermal_xscorr.f90`

   Compute the x-ray absorption from the convolution of quasiparticle cross section with the lifetime of the core hole and experimental broadening.

2. `POT/m_thermal_scf.f90`

   Compute the density of states, total number of electrons and chemical potential.

3. `XSPH/phmesh2T.f90`

   Generate the energy grid for computing the Green's function.

C.3 Example Calculations

In this section, we provide the L_3-edge XANES calculation for early transition metals (titanium and vanadium) where the d-bands are partially filled and for late transition metals (silver and gold) where the d-bands are full. Fig C.1 and C.2 show the temperature dependence of titanium (Ti) and vanadium (V) respectively. The XANES of Ti and V are blue-shifted with increasing temperature because the chemical potential are located in the middle of the d-bands and the density of states above the chemical potential are higher. At the same time, the broadening of the Fermi-Dirac distribution includes a wider energy range of d-states in the transition which resulted in the onset of the pre-edge. In contrast, the XANES of silver (Ag) and gold (Au) are red-shifted as shown in Fig C.3 and C.4 respectively. The opposing behavior is due to the higher density of states below the chemical potential. The onset of the pre-edge structures are due to the broadening of the Fermi-Dirac

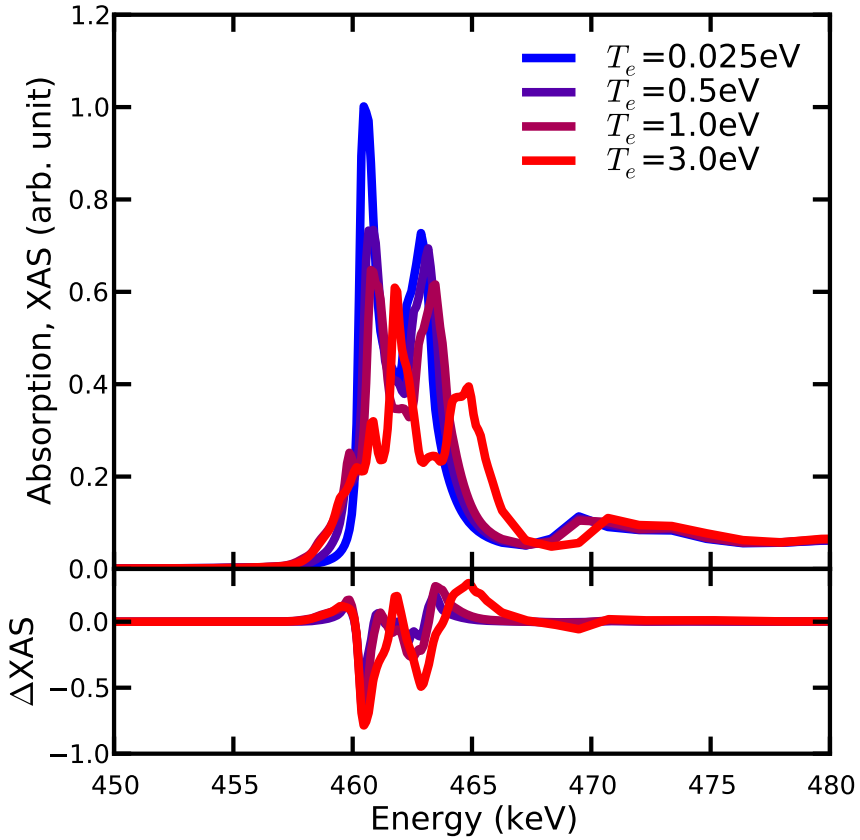

Figure C.1: (Top) Electron temperature dependence of L_3-edge in titanium for T_e= 0.025, 0.5, 1.0 and 3.0 eV. (Bottom) The difference in absorption with respect to the T_e= 0.025 eV absorption spectrum.

distribution. In summary, the changes in XANES is sensitive to the details of the density of states near the chemical potential.

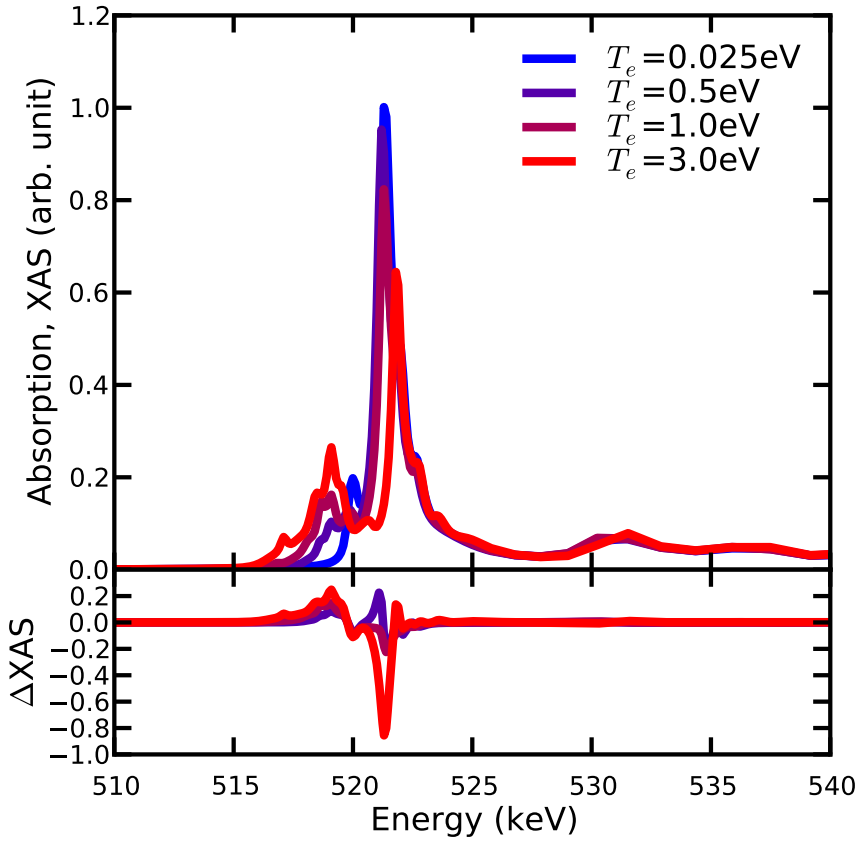

Figure C.2: (Top) Electron temperature dependence of L_3-edge in vanadium for T_e= 0.025, 0.5, 1.0 and 3.0 eV. (Bottom) The difference in absorption with respect to the T_e= 0.025 eV absorption spectrum.

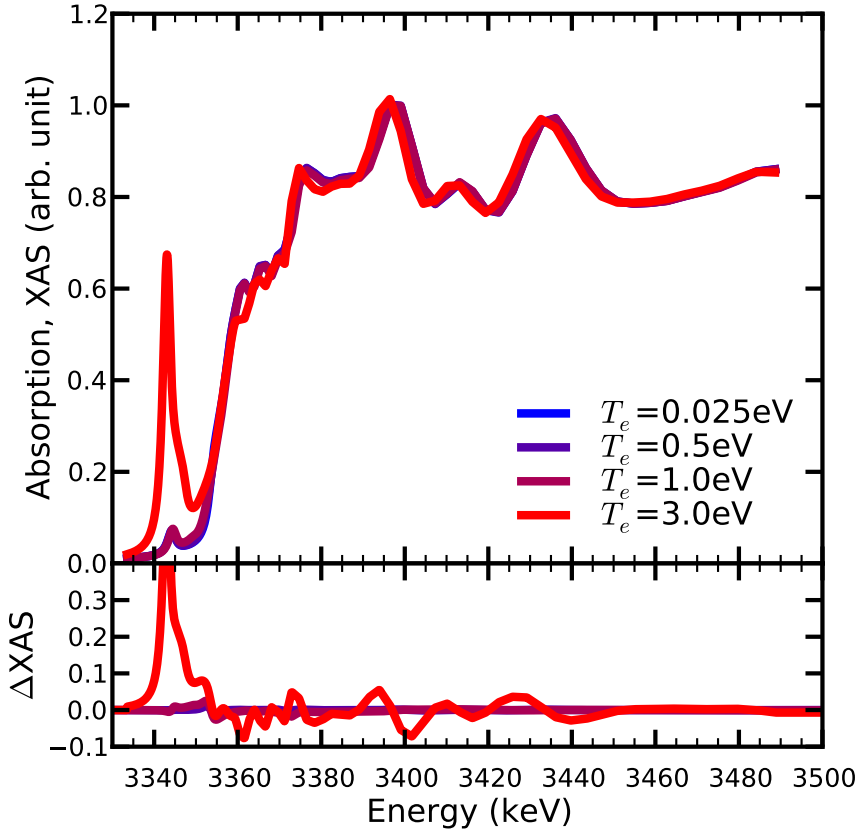

Figure C.3: (Top) Electron temperature dependence of L_3-edge in silver for T_e= 0.025, 0.5, 1.0 and 3.0 eV. (Bottom) The difference in absorption with respect to the T_e= 0.025 eV absorption spectrum.

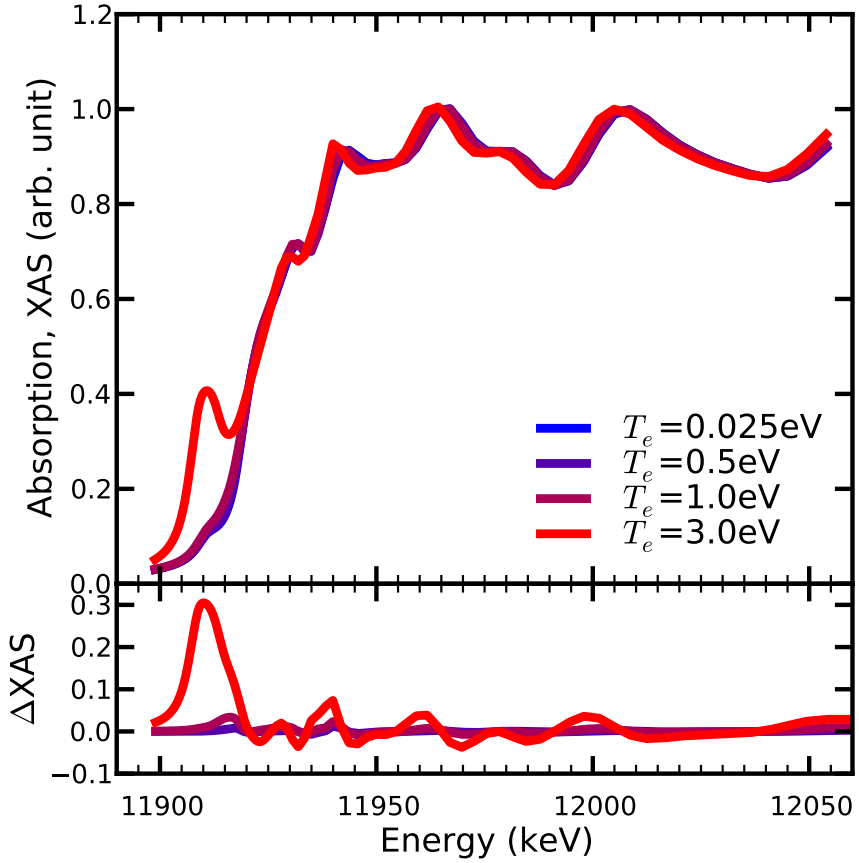

Figure C.4: (Top) Electron temperature dependence of L_3-edge in gold for T_e= 0.025, 0.5, 1.0 and 3.0 eV. (Bottom) The difference in absorption with respect to the T_e= 0.025 eV absorption spectrum.

Appendix D

DERIVATION OF STATIC COHSEX APPROXIMATION

In this section, we present some additional details of the derivation of the static FT COHSEX approximation from the fully dynamic FT quasiparticle COHSEX self-energy. Starting from Eq. (5.12) and (5.13) and using the Sokhotski-Plemelj formula, we can separate the COH term into real and imaginary parts as

$$\mathrm{Re}[\Sigma^{COH}(k,\omega)] = \mathcal{P}\int_0^\infty d\omega' \int \frac{d^3q}{(2\pi)^3} D(q,\omega')\left[\frac{N(\omega')}{\omega+\omega'-\varepsilon_{\mathbf{k}-\mathbf{q}}} + \frac{1+N(\omega')}{\omega-\omega'-\varepsilon_{\mathbf{k}-\mathbf{q}}}\right] \tag{D.1}$$

$$\begin{aligned}\mathrm{Im}[\Sigma^{COH}(k,\omega)] = -\pi\int_0^\infty d\omega' \int \frac{d^3q}{(2\pi)^3} D(q,\omega')\Big[&N(\omega')\delta(\omega+\omega'-\varepsilon_{\mathbf{k}-\mathbf{q}})+\\ &+[1+N(\omega')]\,\delta(\omega-\omega'-\varepsilon_{\mathbf{k}-\mathbf{q}})\Big],\end{aligned} \tag{D.2}$$

where $\mathcal{P}$ denotes the principal value. To further simplify Eq. (D.2), we use the antisymmetric property of $D(q,\omega)$ and $N(-\omega) = -1 - N(\omega)$, so that

$$\begin{aligned}\mathrm{Im}[\Sigma^{COH}(k,\omega)] &= -\pi\int \frac{d^3q}{(2\pi)^3}\Big[D(q,\varepsilon_{\mathbf{k}-\mathbf{q}}-\omega)N(\varepsilon_{\mathbf{k}-\mathbf{q}}-\omega)\theta(\varepsilon_{\mathbf{k}-\mathbf{q}}-\omega)\\ &\quad + D(q,\omega-\varepsilon_{\mathbf{k}-\mathbf{q}})\Big[1+N(\omega-\varepsilon_{\mathbf{k}-\mathbf{q}})\Big]\theta(\omega-\varepsilon_{\mathbf{k}-\mathbf{q}})\Big]\\ &= -\pi\int \frac{d^3q}{(2\pi)^3}\Big[D(q,\varepsilon_{\mathbf{k}-\mathbf{q}}-\omega)N(\varepsilon_{\mathbf{k}-\mathbf{q}}-\omega)\Big].\end{aligned} \tag{D.3}$$

In the limit of static screening ($\omega - \varepsilon \to 0^+$), the imaginary part is found by evaluating $D(q,\omega)$ and $N(\omega)$ at low frequency: $D(q,\omega) \propto \omega$ due to particle-hole continuum excitations, and $N(\omega) \to k_BT/\omega$ because k_BT is large compared to $\omega \to 0^+$ for $T > 0$. On the other hand, the Bose factors in the real part cancel identically for all ω' after taking the static limit, so we end up with the same form as in the zero temperature limit, up to the temperature

dependence of the screened coulomb interaction. Therefore, the FT static COHSEX becomes

$$\mathrm{Re}[\Sigma^{SEX}(k)] = -\int \frac{d^3q}{(2\pi)^3} f(\varepsilon_{\mathbf{k}-\mathbf{q}}) \mathrm{Re}[W_M(q,0)], \tag{D.4}$$

$$\begin{aligned}\mathrm{Re}[\Sigma^{COH}(k)] &= \mathcal{P}\int_0^\infty d\omega' \int \frac{d^3q}{(2\pi)^3} D(q,\omega') \left[\frac{N(\omega')}{\omega'} + \frac{1+N(\omega')}{-\omega'}\right] \\ &= \mathcal{P}\int_0^\infty d\omega' \int \frac{d^3q}{(2\pi)^3} \frac{D(q,\omega')}{-\omega'} \\ &= \frac{1}{2}\int \frac{d^3q}{(2\pi)^3} W_p(q,0).\end{aligned} \tag{D.5}$$

$$\mathrm{Im}[\Sigma^{SEX}(k)] = -\int \frac{d^3q}{(2\pi)^3} f(\varepsilon_{\mathbf{k}-\mathbf{q}}) \mathrm{Im}[W(q,0)] = 0, \tag{D.6}$$

$$\begin{aligned}\mathrm{Im}[\Sigma^{COH}(k)] &= -\pi \int \frac{d^3q}{(2\pi)^3} \lim_{\omega'\to 0^+} D(q,\omega') N(\omega') \\ &= -\pi k_B T \int \frac{d^3q}{(2\pi)^3} \alpha(\mathbf{q}),\end{aligned} \tag{D.7}$$

where $\alpha(q) = dD(q,\omega)/d\omega|_{\omega=0}$ is the proportionality constant. While the imaginary part of the static COH is linear in temperature, it is relatively small compared to the fully dynamic FT quasiparticle self-energy. To complete the derivation, we then use the following relations to convert the retarded static COHSEX results into time-ordered quantities

$$\mathrm{Re}[G_R(k,\omega)] = \mathrm{Re}[G_T(k,\omega)], \tag{D.8}$$

$$\mathrm{Im}[G_R(k,\omega)] = \coth(\omega/2T)\ \mathrm{Im}[G_T(k,\omega)]. \tag{D.9}$$

Appendix E

FE/MGO HETEROSTRUCTURE

E.1 Normalization of O K-edge

In this section, we describe the method used to handle the pre-edge background in the O K-edge measurements. The left plot in Fig. E.1 shows the raw experiment measurements for O K-edge at time-delay $t = 870$ fs and 90 ps. The measurements of O K-edge at 870 fs time-delay have significant background obscuring the pre-edge. Due to the setup of the experiment, the background is same in both the signal before and after pumping. Thus, the background does not affect the spectral differences but it is hard to estimate the relative amplitude of the peaks in the 870 fs measurement. To overcome this, we perform background subtraction on both measurements using Larch [132] and offset the 870 fs measurements to match the 90 ps measurements. The resulting absorption amplitude after the background subtraction process is shown in right plot of Fig E.1. This process allows us to get an estimate for the fine structure amplitude above the edge.

E.2 Density of State Calculation

In this section, we present the full layer resolved density of states (DOS) for Fe/MgO heterostructure. We perform the local spin density approximation electronic structure calculation using a $5 \times 5 \times 5$ supercell with a full multiple scattering radius $r_{fms} = 6.0$ Å. In our calculation, there are 8 unique layers in the heterostructure namely, the center layer (L1) of Fe, adjacent layer (L2) of Fe, next adjacent layer (L3) of Fe, interface layer (L4) of Fe, L1 of MgO, L2 of MgO, L3 of MgO and L4 of MgO. The DOS are shown in Fig E.2. The FEFF DOS for MgO are shifted by -2.6eV and Fe are shifted by 0.2eV to match the Fermi level of the DFT. Our calculated Fe DOS in the bulk (L1,L2,L3) are similar to the DFT

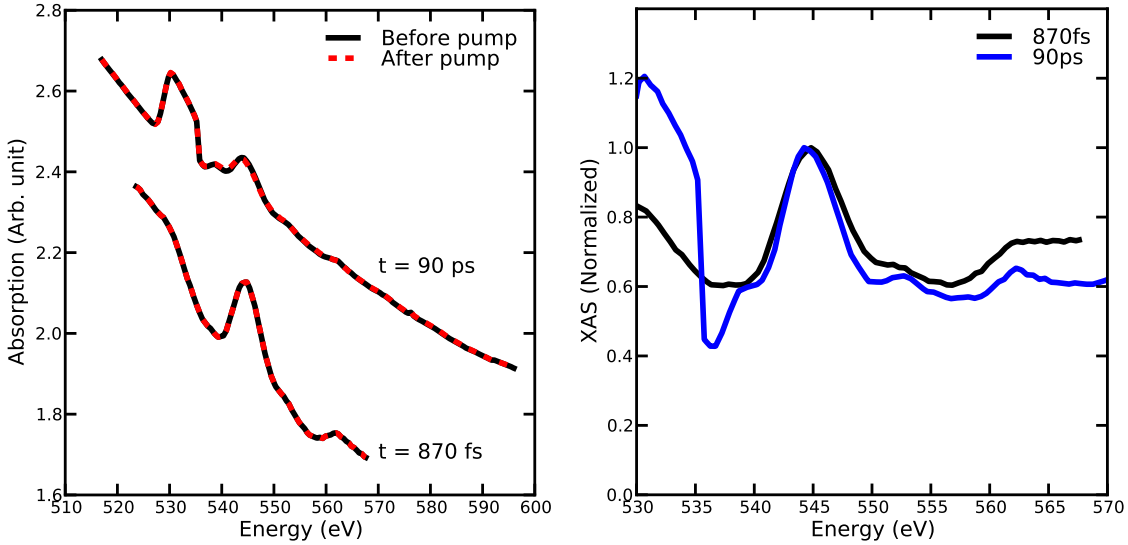

Figure E.1: (Left) Oxygen K-edge X-ray absorption before background subtraction at time-delay t = 870 fs and 90 ps. In black are the measurements before pumping and in red are the measurements after pumping. The differences in the signals are very small to observed. (Right) Background subtracted absorption measurement before pumping at time-delay t = 870 fs (black) and 90 ps (blue).

calculation by Rothenbach et al. [8]. At the edge, there is a highly localized state above the Fermi level due to the hybridization with oxygen at the interface. For the MgO layers, our oxygen calculation agrees well with the DFT in the bulk (L1,L2,L3). But at the interface, the localized state due to the hybridization is at the wrong energy due to the error in the Fermi level placement (prior to the -2.6 eV shift. Refer to Fig 4.10). This results in large states near -2eV in spin down DOS at the MgO interface layer. In addition, the MgO DOS are also different from the DFT results. FEFF is known to not yield accurate result for light oxide elements like MgO.[133]

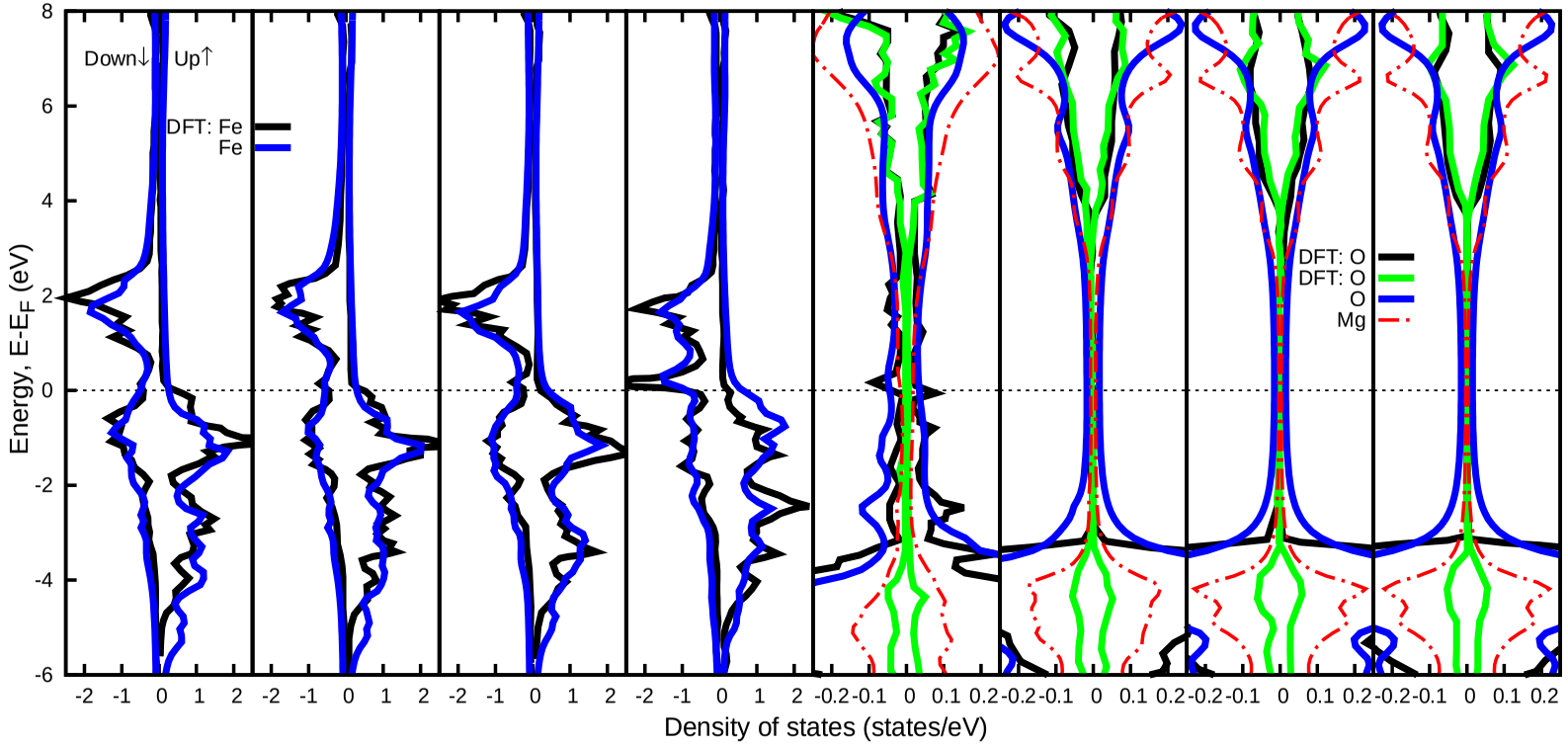

Figure E.2: Layer resolved density of states (DOS) for Fe/MgO at T_e=0K. From the left, the first four figures are the iron total DOS of layers from L1 to L4 and the last four figures are the DOS for oxygen and magnesium of layers from L4 to L1. The FEFF DOS for MgO are shifted by -2.6eV and Fe are shifted by 0.2eV to match the Fermi level of the DFT. The reference density of states are the DFT calculation by Rothenbach et al. [8].

BIBLIOGRAPHY

[1] A. Savin Shelley L.P.and Berko, A. N. Blacklocks, W. Edwards, and A. V. Chadwick, "The applications of x-ray absorption spectroscopy in the study of nanocrystalline materials and electrochemical systems," Comptes Rendus Chimie **11**, 948–963 (2008).

[2] G. J. Sherborne and B. N. Nguyen, "Recent xas studies into homogeneous metal catalyst in fine chemical and pharmaceutical syntheses," Chemistry Central Journal **9**, 37 (2015).

[3] F. Lin et al., "Synchrotron x-ray analytical techniques for studying materials electrochemistry in rechargeable batteries," Chemical Reviews **117**, 13123–13186 (2017).

[4] R. Bolis et al., "X-ray absorption near edge spectroscopy study of warm dense mgo," Physics of Plasmas **26**, 112703 (2019).

[5] B. I. Cho et al., "Electronic structure of warm dense copper studied by ultrafast x-ray absorption spectroscopy," Phys. Rev. Lett. **106**, 167601 (2011).

[6] C. Stamm, N. Pontius, T. Kachel, M. Wietstruk, and H. A. Dürr, "Femtosecond x-ray absorption spectroscopy of spin and orbital angular momentum in photoexcited Ni films during ultrafast demagnetization," Phys. Rev. B **81**, 104425 (2010).

[7] E. Beaurepaire, J.-C. Merle, A. Daunois, and J.-Y. Bigot, "Ultrafast spin dynamics in ferromagnetic nickel," Phys. Rev. Lett. **76**, 4250–4253 (1996).

[8] N. Rothenbach et al., "Microscopic nonequilibrium energy transfer dynamics in a photoexcited metal/insulator heterostructure," Phys. Rev. B **100**, 174301 (2019).

[9] J. J. Rehr, J. A. Soininen, and E. L. Shirley, "Final-state rule vs the bethe-salpeter equation for deep-core x-ray absorption spectra," Physica Scripta, 207 (2005).

[10] W. Kohn and L. J. Sham, "Self-consistent equations including exchange and correlation effects," Phys. Rev. **140**, A1133–A1138 (1965).

[11] P. Hohenberg and W. Kohn, "Inhomogeneous electron gas," Phys. Rev. **136**, B864–B871 (1964).

[12] C. R. Natoli, M. Benfatto, and S. Doniach, "Use of general potentials in multiple-scattering theory," Phys. Rev. A **34**, 4682–4694 (1986).

[13] J. J. Rehr and R. C. Albers, "Scattering-matrix formulation of curved-wave multiple-scattering theory: application to x-ray-absorption fine structure," Phys. Rev. B **41**, 8139–8149 (1990).

[14] A. L. Ankudinov, Y. Takimoto, and J. J. Rehr, "Combined Bethe-Saltpeter equations and time-dependent density-functional theory approach for x-ray absorption calculations," Phys. Rev. B **71**, 165110 (2005).

[15] L. Campbell, L. Hedin, J. J. Rehr, and W. Bardyszewski, "Interference between extrinsic and intrinsic losses in x-ray absorption fine structure," Phys. Rev. B **65**, 064107 (2002).

[16] A. Zangwill and P. Soven, "Density-functional approach to local-field effects in finite systems: photoabsorption in the rare gases," Phys. Rev. A **21**, 1561–1572 (1980).

[17] A. L. Ankudinov, A. I. Nesvizhskii, and J. J. Rehr, "Dynamic screening effects in x-ray absorption spectra," Phys. Rev. B **67**, 115120 (2003).

[18] J. J. Kas, T. D. Blanton, and J. J. Rehr, "Exchange-correlation contributions to thermodynamic properties of the homogeneous electron gas from a cumulant Green's function approach," Phys. Rev. B **100**, 195144 (2019).

[19] International X-ray Absorption Society, *X-ray absorption data library*, (2020).

[20] W. B. Hubbard, T. Guillot, J. I. Lunine, A. Burrows, D. Saumon, M. S. Marley, and R. S. Freedman, "Liquid metallic hydrogen and the structure of brown dwarfs and giant planets," Physics of Plasmas **4**, 2011–2015 (1997).

[21] G. Chabrier, P. Brassard, G. Fontaine, and D. Saumon, "Cooling sequences and color-magnitude diagrams for cool white dwarfs with hydrogen atmospheres," The Astrophysical Journal **543**, 216–226 (2000).

[22] N. Nettelmann, R. Püstow, and R. Redmer, "Saturn layered structure and homogeneous evolution models with different eoss," Icarus **225**, 548–557 (2013).

[23] H. F. Wilson and B. Militzer, "Sequestration of noble gases in giant planet interiors," Phys. Rev. Lett. **104**, 121101 (2010).

[24] J. Daligault and S. Gupta, "Electron–ion Scattering In Dense Multi-component Plasmas: Application To The Outer Crust Of An Accreting Neutron Star," The Astrophysical Journal **703**, 994–1011 (2009).

[25] A. Mančić et al., "Picosecond short-range disordering in isochorically heated aluminum at solid density," Phys. Rev. Lett. **104**, 035002 (2010).

[26] B. Mahieu, N. Jourdain, K. Ta Phuoc, F. Dorchies, J.-P. Goddet, A. Lifschitz, P. Renaudin, and L. Lecherbourg, "Probing warm dense matter using femtosecond x-ray absorption spectroscopy with a laser-produced betatron source," Nature Communications **9**, 3276 (2018).

[27] B. I. Cho et al., "Measurement of electron-ion relaxation in warm dense copper," Scientific Reports **6**, 18843 (2016).

[28] P. Ludwig, M. Bonitz, H. Kählert, and J. W. Dufty, "Dynamics of strongly correlated ions in a partially ionized quantum plasma," Journal of Physics: Conference Series **220**, 012003 (2010).

[29] M. Bonitz, T. Dornheim, Z. A. Moldabekov, S. Zhang, P. Hamann, H. Kählert, A. Filinov, K. Ramakrishna, and J. Vorberger, "Ab initio simulation of warm dense matter," Physics of Plasmas **27**, 042710 (2020).

[30] T. Dornheim, S. Groth, and M. Bonitz, "The uniform electron gas at warm dense matter conditions," Physics Reports **744**, 1–86 (2018).

[31] N. D. Mermin, "Thermal properties of the inhomogeneous electron gas," Phys. Rev. **137**, A1441–A1443 (1965).

[32] V. V. Karasiev, T. Sjostrom, J. Dufty, and S. B. Trickey, "Accurate homogeneous electron gas exchange-correlation free energy for local spin-density calculations," Phys. Rev. Lett. **112**, 076403 (2014).

[33] M. W. C. Dharma-wardana and F. Perrot, "Simple classical mapping of the spin-polarized quantum electron gas: distribution functions and local-field corrections," Phys. Rev. Lett. **84**, 959–962 (2000).

[34] C. E. Starrett and D. Saumon, "Equation of state of dense plasmas with pseudoatom molecular dynamics," Phys. Rev. E **93**, 063206 (2016).

[35] N. Gill and C. Starrett, "Tartarus: a relativistic green's function quantum average atom code," High Energy Density Physics **24**, 33–38 (2017).

[36] N. Jourdain, L. Lecherbourg, V. Recoules, P. Renaudin, and F. Dorchies, "Electron-ion thermal equilibration dynamics in femtosecond heated warm dense copper," Phys. Rev. B **97**, 075148 (2018).

[37] E. C. Stoner, "Collective electron ferromagnetism," Proceedings of the Royal Society of London. Series A, Mathematical and Physical Sciences **165**, 372–414 (1938).

[38] M. Shimizu, "Itinerant electron magnetism," Reports on Progress in Physics **44**, 329–409 (1981).

[39] K. Zakeri, "Elementary spin excitations in ultrathin itinerant magnets," Physics Reports **545**, Elementary spin excitations in ultrathin itinerant magnets, 47–93 (2014).

[40] H.-S. Rhie, H. A. Dürr, and W. Eberhardt, "Femtosecond electron and spin dynamics in Ni/W(110) films," Phys. Rev. Lett. **90**, 247201 (2003).

[41] K. Carva, D. Legut, and P. M. Oppeneer, "Influence of laser-excited electron distributions on the x-ray magnetic circular dichroism spectra: implications for femtosecond demagnetization in ni," EPL (Europhysics Letters) **86**, 57002 (2009).

[42] R. Carley, K. Döbrich, B. Frietsch, C. Gahl, M. Teichmann, O. Schwarzkopf, P. Wernet, and M. Weinelt, "Femtosecond laser excitation drives ferromagnetic gadolinium out of magnetic equilibrium," Phys. Rev. Lett. **109**, 057401 (2012).

[43] M. Pickel, A. B. Schmidt, M. Weinelt, and M. Donath, "Magnetic exchange splitting in fe above the curie temperature," Phys. Rev. Lett. **104**, 237204 (2010).

[44] E. Carpene, H. Hedayat, F. Boschini, and C. Dallera, "Ultrafast demagnetization of metals: Collapsed exchange versus collective excitations," Phys. Rev. B **91**, Publisher: American Physical Society, 174414 (2015).

[45] S. Eich et al., "Band structure evolution during the ultrafast ferromagnetic-paramagnetic phase transition in cobalt," Science Advances **3**, e1602094 (2017).

[46] D. E. Eastman, F. J. Himpsel, and J. A. Knapp, "Experimental band structure and temperature-dependent magnetic exchange splitting of nickel using angle-resolved photoemission," Phys. Rev. Lett. **40**, 1514–1517 (1978).

[47] S. I. Anisimov, B. L. Kapeliovich, and T. L. Perelman, "Electron emission from metal surfaces exposed to ultrashort laser pulses," Zhurnal Eksperimentalnoi i Teoreticheskoi Fiziki **66**, 776–781 (1974).

[48] C. E. Starrett, "High-temperature electronic structure with the Korringa-Kohn-Rostoker Green's function method," Phys. Rev. E **97**, 053205 (2018).

[49] T. S. Tan, J. J. Kas, and J. J. Rehr, "Coulomb-hole and screened exchange in the electron self-energy at finite temperature," Physical Review B **98**, 115125 (2018).

[50] K. Hatada, K. Hayakawa, M. Benfatto, and C. R. Natoli, "Full-potential multiple scattering for x-ray spectroscopies," Phys. Rev. B **76**, 060102 (2007).

[51] H. Ebert, D. Ködderitzsch, and J. Minár, "Calculating condensed matter properties using the KKR-Green's function method—recent developments and applications," Reports on Progress in Physics **74**, 096501, 096501 (2011).

[52] J. J. Rehr, J. J. Kas, F. D. Vila, M. P. Prange, and K. Jorissen, "Parameter-free calculations of x-ray spectra with FEFF9," Phys. Chem. Chem. Phys. **12**, 5503–5513 (2010).

[53] A. L. Ankudinov, B. Ravel, J. J. Rehr, and S. D. Conradson, "Real-space multiple-scattering calculation and interpretation of x-ray-absorption near-edge structure," Phys. Rev. B **58**, 7565–7576 (1998).

[54] M. P. Prange, J. J. Rehr, G. Rivas, J. J. Kas, and J. W. Lawson, "Real space calculation of optical constants from optical to x-ray frequencies," Phys. Rev. B **80**, 155110 (2009).

[55] U. v. Barth and L. Hedin, "A local exchange-correlation potential for the spin polarized case. i," Journal of Physics C: Solid State Physics **5**, 1629–1642 (1972).

[56] B. Mattern, "Compton scattering and warm dense matter thermometry," PhD dissertation (University of Washington).

[57] K. Wildberger, P. Lang, R. Zeller, and P. H. Dederichs, "Fermi-Dirac distribution in ab initio Green's-function calculations," Phys. Rev. B **52**, 11502–11508 (1995).

[58] L. Hedin and S. Lundqvist, in *Solid state physics*, Vol. 23 (Academic Press), pp. 1–181.

[59] F. Giustino, "Electron-phonon interactions from first principles," Rev. Mod. Phys. **89**, 015003 (2017).

[60] P. B. Allen, "Theory of thermal relaxation of electrons in metals," Phys. Rev. Lett. **59**, 1460–1463 (1987).

[61] T. Q. Qiu and C. L. Tien, "Short-pulse laser heating on metals," International Journal of Heat and Mass Transfer **35**, 719–726 (1992).

[62] T. Q. Qiu and C. L. Tien, "Heat Transfer Mechanisms During Short-Pulse Laser Heating of Metals," Journal of Heat Transfer **115**, 835–841 (1993).

[63] T. Q. Qiu and C. L. Tien, "Femtosecond laser heating of multi-layer metals—I. analysis," International Journal of Heat and Mass Transfer **37**, 2789–2797 (1994).

[64] O. M. Roscioni, P. D'Angelo, G. Chillemi, S. Della Longa, and M. Benfatto, "Quantitative analysis of XANES spectra of dis-ordered systems based on molecular dynamics," Journal of Synchrotron Radiation **12**, 75–79 (2005).

[65] S. Boccato et al., "Melting properties by x-ray absorption spectroscopy: common signatures in binary Fe-C, Fe-O, Fe-S and Fe-Si systems," Scientific Reports **10**, 11663 (2020).

[66] V. Recoules and S. Mazevet, "Temperature and density dependence of xanes spectra in warm dense aluminum plasmas," Phys. Rev. B **80**, 064110 (2009).

[67] O. Peyrusse, "Real-space finite-difference calculations of XANES spectra along the aluminum Hugoniot from molecular dynamics simulations," High Energy Density Physics **6**, 357–364 (2010).

[68] D. Kang, J. Dai, H. Sun, Y. Hou, and J. Yuan, "Quantum simulation of thermally-driven phase transition and oxygen K-edge x-ray absorption of high-pressure ice," Scientific Reports **3**, 3272 (2013).

[69] T. Fujikawa, "Theory of atomic displacement effects induced by core-hole production on EXAFS," Journal of the Physical Society of Japan **65**, 87–94 (1996).

[70] T. Fujikawa, "XAFS theory at zero and finite temperature," Journal of the Physical Society of Japan **68**, 2444–2456 (1999).

[71] R. Nemausat, D. Cabaret, C. Gervais, C. Brouder, N. Trcera, A. Bordage, I. Errea, and F. Mauri, "Phonon effects on x-ray absorption and nuclear magnetic resonance spectroscopies," Phys. Rev. B **92**, 144310 (2015).

[72] R. Nemausat et al., "Temperature dependence of x-ray absorption and nuclear magnetic resonance spectra: probing quantum vibrations of light elements in oxides," Phys. Chem. Chem. Phys. **19**, 6246–6256 (2017).

[73] D. Marx and J. Hutter, *Ab initio molecular dynamics: basic theory and advanced methods* (Cambridge University Press).

[74] L. Woodcock, "Isothermal molecular dynamics calculations for liquid salts," Chemical Physics Letters **10**, 257–261 (1971).

[75] H. C. Andersen, "Molecular dynamics simulations at constant pressure and/or temperature," The Journal of Chemical Physics **72**, 2384–2393 (1980).

[76] T. Schneider and E. Stoll, "Molecular-dynamics study of a three-dimensional one-component model for distortive phase transitions," Phys. Rev. B **17**, 1302–1322 (1978).

[77] H. J. C. Berendsen, J. P. M. Postma, W. F. van Gunsteren, A. DiNola, and J. R. Haak, "Molecular dynamics with coupling to an external bath," The Journal of Chemical Physics **81**, 3684–3690 (1984).

[78] W. G. Hoover, "Canonical dynamics: equilibrium phase-space distributions," Phys. Rev. A **31**, 1695–1697 (1985).

[79] S. Nosé, "A unified formulation of the constant temperature molecular dynamics methods," The Journal of Chemical Physics **81**, 511–519 (1984).

[80] W. Cochran, "The relation between phonon frequencies and interatomic force constants," Acta Crystallographica Section A **27**, 556–559 (1971).

[81] X. Gonze, "Adiabatic density-functional perturbation theory," Phys. Rev. A **52**, 1096–1114 (1995).

[82] S. Baroni, P. Giannozzi, and A. Testa, "Green's-function approach to linear response in solids," Phys. Rev. Lett. **58**, 1861–1864 (1987).

[83] P.-W. Ma, S. L. Dudarev, and C. H. Woo, "Spin-lattice-electron dynamics simulations of magnetic materials," Phys. Rev. B **85**, 184301 (2012).

[84] B. Koopmans, J. J. M. Ruigrok, F. D. Longa, and W. J. M. de Jonge, "Unifying ultrafast magnetization dynamics," Phys. Rev. Lett. **95**, 267207 (2005).

[85] S. Ono, "Thermalization in simple metals: role of electron-phonon and phonon-phonon scattering," Phys. Rev. B **97**, 054310 (2018).

[86] P. Maldonado, K. Carva, M. Flammer, and P. M. Oppeneer, "Theory of out-of-equilibrium ultrafast relaxation dynamics in metals," Phys. Rev. B **96**, 174439 (2017).

[87] Z. Lin, L. V. Zhigilei, and V. Celli, "Electron-phonon coupling and electron heat capacity of metals under conditions of strong electron-phonon nonequilibrium," Phys. Rev. B **77**, 075133 (2008).

[88] R. Chimata, A. Bergman, L. Bergqvist, B. Sanyal, and O. Eriksson, "Microscopic model for ultrafast remagnetization dynamics," Phys. Rev. Lett. **109**, 157201 (2012).

[89] R. F. L. Evans, W. J. Fan, P. Chureemart, T. A. Ostler, M. O. A. Ellis, and R. W. Chantrell, "Atomistic spin model simulations of magnetic nanomaterials," Journal of Physics: Condensed Matter **26**, 103202 (2014).

[90] O. Peyrusse, "Theoretical calculations of K-edge absorption spectra in warm dense Al," Journal of Physics: Condensed Matter **20**, 195211 (2008).

[91] N. Jourdain, V. Recoules, L. Lecherbourg, P. Renaudin, and F. Dorchies, "Understanding XANES spectra of two-temperature warm dense copper using ab initio simulations," Phys. Rev. B **101**, 125127 (2020).

[92] G. Kresse and J. Furthmüller, "Efficient iterative schemes for ab initio total-energy calculations using a plane-wave basis set," Phys. Rev. B **54**, 11169–11186 (1996).

[93] G. Kresse and D. Joubert, "From ultrasoft pseudopotentials to the projector augmented-wave method," Phys. Rev. B **59**, 1758–1775 (1999).

[94] J. P. Perdew, K. Burke, and M. Ernzerhof, "Generalized gradient approximation made simple," Phys. Rev. Lett. **77**, 3865–3868 (1996).

[95] Unpublished cif file for FeMgO heterostructure by Markus Gruner and Rossitza Pentcheva., (2020).

[96] N. Rothenbach et al., "Modeling the spectroscopic fine structures of pump-induced changes in time-resolved soft x-ray absorption spectroscopy of an Fe/MgO multilayer," arXiv e-prints, arXiv:1911.06201 (2019).

[97] I. Razdolski, A. Alekhin, U. Martens, D. Bürstel, D. Diesing, M. Münzenberg, U. Bovensiepen, and A. Melnikov, "Analysis of the time-resolved magneto-optical Kerr effect for ultrafast magnetization dynamics in ferromagnetic thin films," Journal of Physics: Condensed Matter **29**, 174002 (2017).

[98] T. Sjostrom and J. Dufty, "Uniform electron gas at finite temperatures," Phys. Rev. B **88**, 115123 (2013).

[99] S. Glenzer et al., "Dense plasma x-ray scattering: methods and applications," High Energy Density Physics **6**, 1–8 (2010).

[100] M. W. C. Dharma-wardana and R. Taylor, "Exchange and correlation potentials for finite temperature quantum calculations at intermediate degeneracies," Journal of Physics C: Solid State Physics **14**, 629–646 (1981).

[101] V. V. Karasiev, L. Calderın, and S. B. Trickey, "Importance of finite-temperature exchange correlation for warm dense matter calculations," Phys. Rev. E **93**, 063207 (2016).

[102] E. W. Brown, B. K. Clark, J. L. DuBois, and D. M. Ceperley, "Path-integral monte carlo simulation of the warm dense homogeneous electron gas," Phys. Rev. Lett. **110**, 146405 (2013).

[103] S. Groth, T. Dornheim, T. Sjostrom, F. D. Malone, W. M. C. Foulkes, and M. Bonitz, "Ab initio exchange-correlation free energy of the uniform electron gas at warm dense matter conditions," Phys. Rev. Lett. **119**, 135001 (2017).

[104] R. Martin, L. Reining, and D. Ceperley, "Interacting electrons: theory and computational approaches," in ().

[105] H. Maebashi and Y. Takada, "Analysis of exact vertex function for improving on the GWΓ scheme for first-principles calculation of electron self-energy," Phys. Rev. B **84**, 245134 (2011).

[106] Y. Pavlyukh, A.-M. Uimonen, G. Stefanucci, and R. van Leeuwen, "Vertex corrections for positive-definite spectral functions of simple metals," Phys. Rev. Lett. **117**, 206402 (2016).

[107] L. Hedin, "New method for calculating the one-particle green's function with application to the electron-gas problem," Phys. Rev. **139**, A796–A823 (1965).

[108] L. Hedin, "On correlation effects in electron spectroscopies and the GW approximation," Journal of Physics: Condensed Matter **11**, R489–R528 (1999).

[109] L. X. Benedict, C. D. Spataru, and S. G. Louie, "Quasiparticle properties of a simple metal at high electron temperatures," Phys. Rev. B **66**, 085116 (2002).

[110] S. V. Faleev, M. van Schilfgaarde, T. Kotani, F. ç. Léonard, and M. P. Desjarlais, "Finite-temperature quasiparticle self-consistent GW approximation," Phys. Rev. B **74**, 033101 (2006).

[111] M. E. Casida and D. P. Chong, "Physical interpretation and assessment of the coulomb-hole and screened-exchange approximation for molecules," Phys. Rev. A **40**, 4837–4848 (1989).

[112] W. Kang and M. S. Hybertsen, "Enhanced static approximation to the electron self-energy operator for efficient calculation of quasiparticle energies," Phys. Rev. B **82**, 195108 (2010).

[113] J. J. Kas and J. J. Rehr, "Finite temperature green's function approach for excited state and thermodynamic properties of cool to warm dense matter," Phys. Rev. Lett. **119**, 176403 (2017).

[114] G. D. Mahan, *Many-particle physics* (Springer US).

[115] P. B. Allen and B. Mitrović, "Theory of superconducting Tc," in , Vol. 37, edited by H. Ehrenreich, F. Seitz, and D. Turnbull, Solid State Physics (Academic Press), pp. 1–92.

[116] F. C. Khanna and H. R. Glyde, "Dynamic susceptibility of Fermi liquids at finite temperature," Canadian Journal of Physics **54**, 648–654 (1976).

[117] N. R. Arista and W. Brandt, "Dielectric response of quantum plasmas in thermal equilibrium," Phys. Rev. A **29**, 1471–1480 (1984).

[118] B. Lundqvist, Phys. kondens. Materie **6**, 206 (1967).

[119] J. J. Kas, J. J. Rehr, and L. Reining, "Cumulant expansion of the retarded one-electron green function," Phys. Rev. B **90**, 085112 (2014).

[120] J. J. Kas and J. J. Rehr, "Finite temperature Green's function approach for excited state and thermodynamic properties of cool to warm dense matter," Phys. Rev. Lett. **119**, 176403 (2017).

[121] J. Vinson, J. J. Rehr, J. J. Kas, and E. L. Shirley, "Bethe-Salpeter equation calculations of core excitation spectra," Phys. Rev. B **83**, 115106 (2011).

[122] A. Marini, "Ab initio finite-temperature excitons," Phys. Rev. Lett. **101**, 106405 (2008).

[123] Y. Takada, "Emergence of an excitonic collective mode in the dilute electron gas," Phys. Rev. B **94**, 245106 (2016).

[124] F. Giustino, M. L. Cohen, and S. G. Louie, "Gw method with the self-consistent sternheimer equation," Phys. Rev. B **81**, 115105 (2010).

[125] P. Pushchnig, *Equation of motion and dynamical matrix*, (2012).

[126] M. Jarrell, *Chapter 4: crystal lattice dynamics*, (2017).

[127] C. E. Patrick and F. Giustino, "Unified theory of electron–phonon renormalization and phonon-assisted optical absorption," Journal of Physics: Condensed Matter **26**, 365503 (2014).

[128] A. V. Poiarkova and J. J. Rehr, "Multiple-scattering x-ray-absorption fine-structure debye-waller factor calculations," Phys. Rev. B **59**, 948–957 (1999).

[129] F. D. Vila, J. J. Rehr, H. H. Rossner, and H. J. Krappe, "Theoretical x-ray absorption Debye-Waller factors," Phys. Rev. B **76**, 014301 (2007).

[130] A. V. Poiarkova and J. J. Rehr, "Recursion method for multiple-scattering XAFS Debye–Waller factors," Journal of Synchrotron Radiation **6**, 313–314 (1999).

[131] S. Boccato, A. Sanson, I. Kantor, O. Mathon, V. Dyadkin, D. Chernyshov, A. Carnera, and S. Pascarelli, "Thermal and magnetic anomalies of α-iron: an exploration by extended x-ray absorption fine structure spectroscopy and synchrotron x-ray diffraction," Journal of Physics: Condensed Matter **28**, 355401 (2016).

[132] M. Newville, "Larch: an analysis package for XAFS and related spectroscopies," Journal of Physics: Conference Series **430**, 012007 (2013).

[133] K. Nakanishi and T. Ohta, "Verification of the FEFF simulations to K-edge XANES spectra of the third row elements," Journal of Physics: Condensed Matter **21**, 104214 (2009).

[134] A. Rohatgi, *Webplotdigitizer: version 4.4*, (2020).